PATIENT-SPECIFIC ENDOVASCULAR AORTIC REPAIR (EVAR)

Andrew Lin (LNXAND004)

In fulfilment of the requirements for the degree: MSc in Biomedical Engineering

University of Cape Town

May 2019

Department of Human Biology: Division of Biomedical Engineering

in association with

Biomaterials Group: Cardiovascular Research Unit

Thesis

Supervisor: Assoc. Prof Deon Bezuidenhout

Co-supervisors: Dr Nikolaus Thierfelder

DECLARATION

I, Andrew Lin , hereby declare that the work on which this dissertation/thesis is based is my original work (except where acknowledgements indicate otherwise) and that neither the whole work nor any part of it has been, is being, or is to be submitted for another degree in this or any other university.

I empower the university to reproduce for the purpose of research either the whole or any portion of the contents in any manner whatsoever.

Signature: Signed by candidate

Date: 24/05/2019

ACKNOWLEDGEMENTS

Firstly, I would like to thank my supervisor, Assoc. Prof Deon Bezuidenhout, for his excellent mentorship on this project, and patience towards teaching me. I am truly grateful for his contribution to this project and my personally development.

I would like to thank Dr Nikolaus Thierfelder for his contribution of ideas and clinical insight, and André Hemmler for his contribution of the FEA simulation data and provision of the commercial stent-grafts for radial force testing.

A great deal of gratitude towards the following people for their assistance with lab work, equipment development, and training on equipment operation: Jandré de Villiers (DSC training), Wesley Elson (fluidised bath training), Jeran Cloete (3D printing consultations), Anel Oosthuysen (lab work consultations), Peter September (Impressive Designs – humidity control Perspex box manufacturing), Sibusisiwe Maseko (lab work consultations), Rosslee Guess (Electrospinning rig development), Vincent Hülk (electrospinning rig and humidity control system development, lunch partner, biltong supplier)

I deeply appreciate the University of Cape Town (UCT) for giving me the opportunity to study here and complete this research, and the National Research Foundation (NRF) for their financial support.

I am very grateful towards my family and friends, especially to my mother (Judy) and father (Mike), for their mental and financial support, and their encouragement throughout my life. To my sister Erin, thank you for being there through my tough times, and always being there to listen. To my beloved Chiayu, thank you for your love and support, you've motivated me in more ways than you can imagine.

I would not have been able to complete the project without the support from all of the above people, for that I am deeply grateful.

ABSTRACT

Endovascular aortic repair (EVAR) is a minimally invasive procedure to treat aortic aneurysms. Current off-the-shelf devices may not fit the patient perfectly, potentially increasing the chance of post-operative complications.

This project aims to provide proof of concept for rapidly creating inexpensive patient-specific EVAR stent-grafts, conforming to the unique anatomy of the patient.

After investigating the range of electrospinning shape capabilities on idealised stent-graft geometries (straight, tapered, elliptical, and curved), CT scans was used to create blood and aortic models of an abdominal aortic aneurysm. The former was used to design a patient-specific stent-graft geometry, 3D print a conductive electrospinning mandrel, and electrospin (290 mm, +18 kV, -3 kV, 5 ml/hr, 5 mm/s, 750 rpm) a luminal layer of Polyurethane (PU). Shape-memory Nitinol wire (Af: body temperature, 380 µm Ø) was heat-set (500°C, 5min) in individual sinusoidal ring-segments (8 wave, 10 mm stent-height, 25 mm Ø), placed over the first layer, and incorporated into the graft by overspinning a second PU layer.

Various geometries were successfully spun. Electrospun PU scaffolds had a mean ultimate tensile strength of 7.3 MPa, mean Young's Modulus of 1.9 MPa, and a mean maximum strain of 571%. Fibre morphology analysis showed a mean orientation index of 0.25 (750 rpm) and 0.35 (1000 rpm), mean fibre diameter of 2.3 µm, and a mean pore size of 7.5 µm; pore size indicates possibility of endothelialisation. Nitinol reinforced patient-specific graft was successfully made and stent-grafts of various stent patterns had radial forces between 1.3 to 5.8 N (comparable to 2.8 N from a commercial example).

FEA simulation highlighted various advantages of customised stent-grafts that conform to the anatomy over standard cylindrical devices such as better seal and contact traction. Simulation results (25 mm Ø, cylindrical, electrospun stent-graft) showed close approximations to experimental results; its use for future stent-graft design optimisations is promising.

Mock insertion of an electrospun patient-specific stent-graft was performed in a 3D-printed transparent-PLA hollow aortic model with good conformity, albeit subpar visibility without a backlight and inflexibility.

Although further improvements can be made to the individual steps, proof of principle was achieved. This process is very promising for the manufacturing of patient-specific devices that could offer better long-term outcomes.

TABLE OF CONTENTS

LIST OF FIGURES

LIST OF TABLES

LIST OF SYMBOL

AAA	*Abdominal Aortic Aneurysm*	Ms	*Martensite start temperature*
A	*Area*	MFM	*Multi-layer Flow Modulator*
Af	*Austenite finish temperature*	*OI*	*Orientation index*
Ap	*Austenite peak temperature*	OS	*Oversize*
As	*Austenite start temperature*	PET	*Polyethylene Terephthalate*
CVD	*Cardiovascular Diseases*	PTFE	*Polytetrafluoroethylene*
CT	*Computed Tomography*	PD	*Pre-deformation*
CAD	*Computer-Aided Design*	r, R	*Radius*
d, D, Ø	*Diameter*	SEM	*Scanning Electron Microscope*
DSC	*Differential Scanning Calorimeter*	P	*Statistical P value*
EVAR	*Endovascular Aortic Repair*	ε	*Strain*
ePTFE	*Expanded Polytetrafluoroethylene*	*t*	*Thickness*
FEA	*Finite Element Analysis*	TAA	*Thoracic Aortic Aneurysm*
FDM	*Fused Deposition Modelling*	TEVAR	*Thoracic Endovascular Aortic Repair*
L	*Length*	TEVG	*Tissue Engineered Vascular-Graft*
l	*Length of ellipse – major axis*	UTS	*Ultimate Tensile Strength*
MRI	*Magnetic Resonance Imaging*	ρ_v	*Volumetric resistivity*
Mf	*Martensite finish temperature*	*w*	*Width of ellipse – minor axis*
Mp	*Martensite peak temperature*	*E*	*Young's Modulus*

1. Introduction

This section provides background information on the need for investigation on aortic aneurysm treatment, as well as the need to improve current EVAR stent-graft designs used to treat it. The literature review covers topics related to stent-graft designs, as well as materials and methods used. The research proposal is then described using a problem statement and project objectives.

1.1. Literature Review

Cardiovascular diseases (CVD) are the world's leading causes of death. These include strokes, myocardial infarction, aortic aneurysm, aortic dissection and other aorta related problems. Many aortic diseases, such as those on the ascending aorta, require open surgery, but advancements in medical technology have allowed the use of minimally invasive techniques to treat certain aortic problems, mostly those relating to the descending aorta such as abdominal aortic aneurysm (AAA) and thoracic aortic aneurysm (TAA). The minimally invasive treatment for AAA's and TAA's are similar, which uses the endovascular aortic repair (EVAR) and thoracic endovascular aortic repair (TEVAR) procedures, respectively.

1.1.1. Pathology & Incidence

Approximately 422.7 million people had some type of CVD in 2015, of which 17.92 million people died from it, which represents 31% of worldwide deaths (Roth et al., 2017). It was estimated that around 92.1 million American adults have at least one type of CVD (Benjamin et al., 2017). Amongst the various CVD's, high blood pressure was the most prevalent, followed by coronary heart diseases such as myocardial infarction, angina pectoris, heart failure, and stroke (Mozaffarian et al., 2015). Although high blood pressure was the most prevalent, ischemic heart disease and stroke were actually the top two killers when it comes to CVD's (Roth et al., 2017), as shown in Figure 1-1.

Aortic aneurysms are enlargements in the diameter of the aorta when compared to its normal diameter. Although not as prevalent, they are still a worldwide issue, with an estimated global annual mortality rate of 168,200 in 2015 (Roth et al., 2017), and 30,000 to 60,000 in the US (Elefteriades & Farkas, 2010); with the highest dead occurrences in the Australasia region (see Figure 1-2). Data from the National Centre for Injury Prevention And Control (NCIPC,2007) showed that aortic-aneurysm-related deaths ranked 15th in 1999 and dropped to 18th in 2007 for the leading causes of death in the US, with an overall decreasing trend for aortic-aneurysm-related deaths from 1999 to 2007, as shown in Figure 1-3. This may be the result of improved healthcare system and technology in the US, as well as healthier lifestyles. However, its global

mortality rate show a continual increase (15% increase from 1990 to 2013) (Mozaffarian et al., 2015), which emphasises the need for investigation and improved treatments.

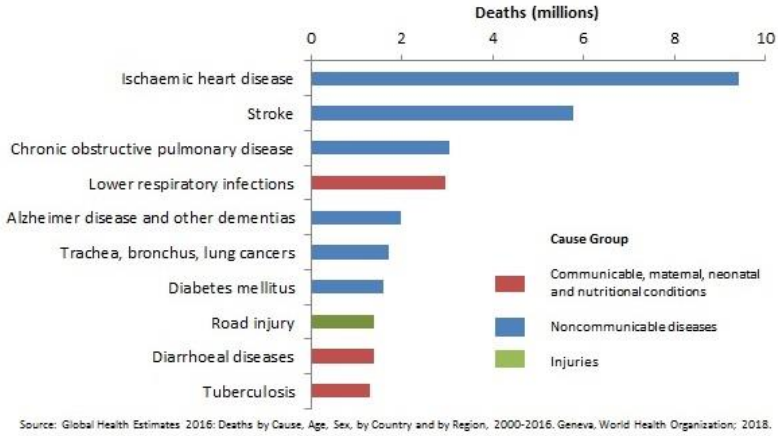

Figure 1-1 Top 10 global causes of deaths, 2016 (WHO,2018)

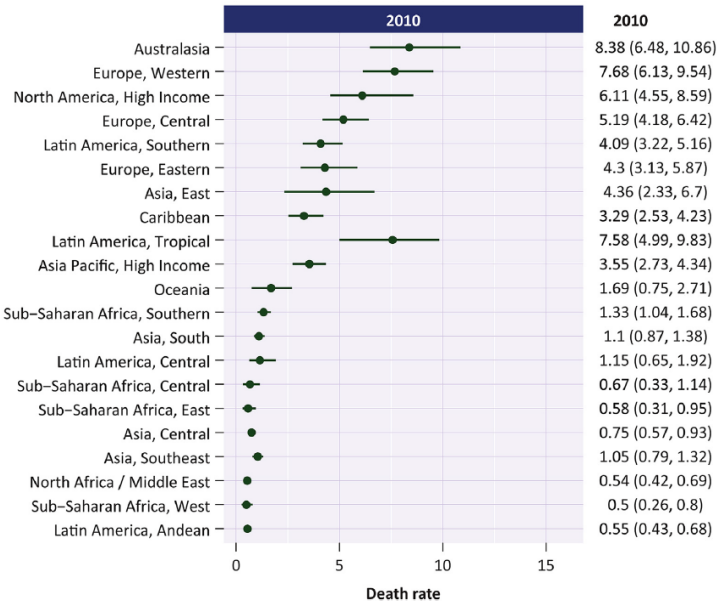

Figure 1-2 Mortality rates per 100,000 people due to aortic aneurysms, with bars showing 95% uncertainty (Sampson et al., 2014)

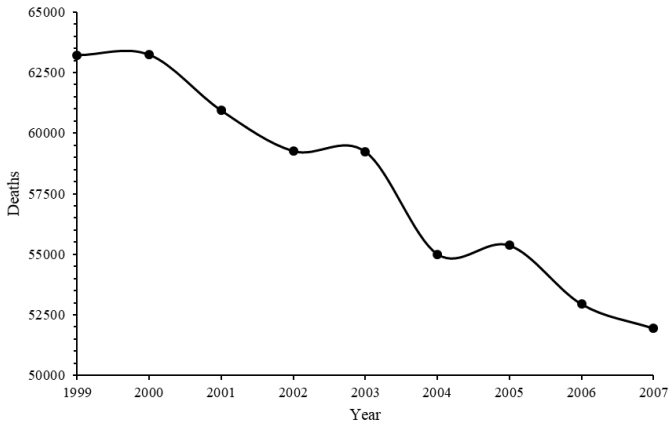

Figure 1-3 Annual aortic-aneurysm-related deaths in the US from 1999 to 2007 (NCIPC,2007)

Aortic aneurysms can occur anywhere on the aorta, but are most commonly seen in the abdominal region, which are called abdominal aortic aneurysms (AAA); occurrences in the thoracic region are called thoracic aortic aneurysms (TAA). An aortic aneurysm is considered problematic when it becomes more than 1.5 times the normal diameter of the aorta (Aggarwal, Qamar, Sharma, & Sharma, 2011). Normal aortic diameters can range between 14.6 to 26.2 mm for the proximal descending aorta, and 17.6 to 35 mm for the ascending aorta (Davis et al., 2013); which decreases as one moves distally from the heart. Factors that affect the normal diameters of the aorta include gender (larger in males) and obesity (larger for people that are obese), as shown in Table 1-1.

Table 1-1 Effects of gender and obesity on normal aortic diameters (Davis et al., 2013)

Male				
Aortic Diameter (mm)	**Normal Weight**	**Overweight**	**Obese**	**ANOVA p**
Aortic Valve Annulus	24.0 (18.8-29.2)	24.7 (19.5-29.9)	25.7 (20.7-30.7)	<0.05
Sinus of Valsalva	32.2 (24.6-39.8)	32.9 (25.3-40.5)	33.3 (25.3-31.3)	<0.05
Sino-tubular Junction	24.9 (18.1-31.7)	25.8 (17.0-34.6)	25.9 (19.1-32.7)	<0.05
Ascending Aorta	26.6 (18.2-35.0)	27.8 (18.8-36.8)	28.6 (23.2-34.0)	<0.01
Proximal Descending Aorta	20.4 (14.6-26.2)	21.2 (15.6-26.8)	22.1 (16.5-27.7)	<0.01
Distal Descending Aorta	17.4 (12.0-22.8)	18.3 (12.7-23.9)	19.0 (14.8-23.2)	<0.01
BMI (kg/m2)	22 (+/- 1.7)	27 (+/- 1.6)	34 (+/- 4.8)	<0.01
BSA (m2)	1.9 (+/- 0.1)	2.0 (+/- 0.1)	2.3 (+/- 0.2)	<0.01
Female				
Aortic Diameter (mm)	**Normal Weight**	**Overweight**	**Obese**	**ANOVA p**
Aortic Valve Annulus	20.2 (17.0-23.4)	21.7 (18.5-23.9)	21.6 (17.6-25.6)	<0.01
Sinus of Valsalva	27.6 (22.0-33.2)	28.6 (21.6-35.6)	27.8 (22.2-33.4)	<0.05
Sino-tubular Junction	21.7 (16.7-26.7)	22.5 (16.5-28.5)	22.3 (16.5-28.1)	<0.05
Ascending Aorta	24.8 (17.6-32.0)	26.7 (19.3-34.1)	26.9 (19.3-34.5)	<0.01
Proximal Descending Aorta	18.6 (14.6-22.6)	19.5 (14.9-24.1)	20.1 (15.5-24.7)	<0.01
Distal Descending Aorta	16.1 (14.1-18.1)	16.9 (14.7-19.1)	17.6 (15.7-19.5)	<0.01
BMI (kg/m2)	22.0 (+/- 1.6)	27.0 (+/- 1.5)	37.0 (+/- 4.8)	<0.01
BSA (m2)	1.7 (+/- 0.1)	1.8 (+/- 0.1)	2.0 (+/- 0.2)	<0.01

Aortic aneurysm is a silent disease, which means it can be dormant and undetected, and the individual can live normally without feeling any pain; usually only 5% of aneurysm patients in the US showed symptoms such as pain, the other 95% of patients usually experience death before any symptoms showing (Elefteriades & Farkas, 2010). However, if it continues to enlarge, it could lead to other complications; if it ruptures, it could cause severe internal bleeding and rapid death, with a mortality rate of more than 75% (Steuer, Lachat, Veith, & Wanhainen, 2016). The most severe case of complications caused by aortic aneurysms is an aortic dissection, which is a tear in the inner wall of the aorta, splitting the layers, causing blood to leak between them (Erbel & Eggebrecht, 2006). They are classified into two types; type A for conditions on the ascending aorta and type B for conditions downwards from the descending aorta (M.-H. Zhang et al., 2017). The risk of getting an aneurysm is affected by age (especially after the age of 60), gender, ethnicity, smoking habits, high blood pressure, bad diets and other environmental factors (Aggarwal et al., 2011).

A study by Elefteriades and Farkas (2010) showed that the growth rate of an aortic aneurysm is usually very slow (1 and 3 mm per year for the ascending and descending aorta, respectively). They recommended treating the diseased aorta before reaching 6 cm in diameter (critical dimension) in order to prevent aneurysm related death. They developed an Aortic Size Index Nomogram to estimate when the aortic diameter is large enough for intervention, taking into account the size of the aneurysm and the body surface area (BSA) of the patient (Elefteriades & Farkas, 2010), as shown in Table 1-2.

Table 1-2 Aortic Size Index Nomogram (Elefteriades & Farkas, 2010)

	Aortic size (cm)									
BSA	**3,5**	**4,0**	**4,5**	**5,0**	**5,5**	**6,0**	**6,5**	**7,0**	**7,5**	**8,0**
1,30	2,69	3,08	3,46	3,85	4,23	4,62	5,00	5,38	5,77	6,15
1,40	2,50	2,86	3,21	3,57	3,93	4,29	4,64	5,00	5,36	5,71
1,50	2,33	2,67	3,00	3,33	3,67	4,00	4,33	4,67	5,00	5,33
1,60	2,19	2,50	2,81	3,13	3,44	3,75	4,06	4,38	4,69	5,00
1,70	2,06	2,35	2,65	2,94	3,24	3,53	3,82	4,12	4,41	4,71
1,80	1,94	2,22	2,50	2,78	3,06	3,33	3,61	3,89	4,17	4,44
1,90	1,84	2,11	2,37	2,63	2,89	3,16	3,42	3,68	3,95	4,21
2,00	1,75	2,00	2,25	2,50	2,75	3,00	3,25	3,50	3,75	4,00
2,10	1,67	1,90	2,14	2,38	2,62	2,86	3,10	3,33	3,57	3,81
2,20	1,59	1,82	2,05	2,27	2,50	2,73	2,95	3,18	3,41	3,64
2,30	1,52	1,74	1,96	2,17	2,39	2,61	2,83	3,04	3,26	3,48
2,40	1,46	1,67	1,88	2,08	2,29	2,50	2,71	2,92	3,13	3,33
2,50	1,40	1,60	1,80	2,00	2,20	2,40	2,60	2,80	3,00	3,20

=low risk (≈4% per yr)
=moderate risk (≈8% per yr)
=severe risk (≈20% per yr)

Initially, many aorta related diseases such as aneurysms were treated with open-surgery, but with a low success rate (surgical mortality exceeding 30%), and a high chance of post-surgery complications (M.-H. Zhang et al., 2017). Throughout the years, as more experience is gained and the advantages became clearer, the preferred treatment option has been shifted towards the minimally invasive EVAR procedure (Arslan, Turba, Sabri, Angle, & Matsumoto, 2009); in most countries, more than 50% of AAA repairs are commonly done using the EVAR procedure (Steuer et al., 2016).

1.1.2. TEVAR/EVAR Procedure

The minimally invasive EVAR procedure aims to regain healthy blood flow through the diseased aorta using a stent-graft, (which is a tubular fabric/scaffold (graft) reinforced with a metal supporting structure (stent)), whilst having lower risk of surgical and post-surgery

complications when compared to open-surgeries. This isolates the aneurysm from the blood flow and prevents it from further expansion.

Medical imaging scans of the blood vessels are usually taken first, which helps determine the optimal arterial access location, suitability of the patient's anatomy for treatment with the EVAR procedure, and stent-graft modification requirements. The stent-graft is crimped to fit inside a catheter usually between 20 to 25F (Findeiss & Cody, 2011). It is usually deployed through the femoral artery; the location of arterial access depend on the size of the catheter required, and valves are used at the arterial opening to provide haemostasis. A guide wire is inserted and navigated to the target location, which is used to guide the stent-graft in the catheter to the target location. Once in the correct position and orientation, verified by fluoroscopy, it is released from the catheter into the aorta; radiopaque markers attached to the stent-graft are clearly visible under fluoroscopy. Depending on the material of the stent and the procedure, the stent-graft could be self-expanding, or a balloon catheter could be used to aid the expansion of the stent-graft (M.-H. Zhang et al., 2017). Once the stent-graft is deployed correctly, the catheter delivery system is removed under fluoroscopy. The EVAR procedure for the treatment of an AAA is depicted in Figure 1-4.

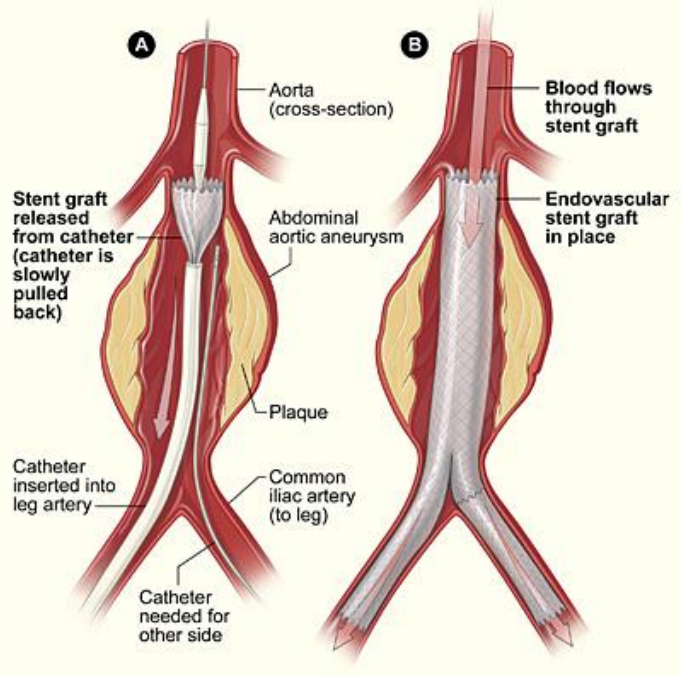

Figure 1-4 EVAR procedure for the treatment of AAA's (NHLBI,2019)

Over the years, the EVAR procedure became the most commonly used method for treating AAA's (England & Mc Williams, 2013). Although EVAR was more commonly used to treat

AAA's, treatment for TAA's on the descending aorta using the TEVAR procedure has also become a common practice.

Morbidity and mortality rates of AAA treatment using the EVAR procedure were shown to be lower compared to the results of open-surgeries in many cases. A randomized trial by Prinssen et al. (2004) showed the combined mortality rate during AAA operations and severe complications was 9.8 percent for the open-surgery group (17 out of 174 patients), and 4.7 percent in the EVAR group (8 out of 171 patients). For an elective EVAR procedure, the 30-day postoperative mortality rate is less than 4%, and if successful, the 5-year survival rate can be as high as 95% (Steuer et al., 2016). Although the perioperative mortality rate of EVAR is significantly lower than that of open-surgery, postoperative complications are still a significant cause of aneurysm-related deaths (Chang et al., 2013); these include endoleaks, stent-graft migration, aortic neck dilation due to stent-graft induced stress, and stent-graft fracture (Hemmler, Lutz, Reeps, Kalender, & Gee, 2018a).

Endoleaks occur when blood flows outside the stent-graft and within the aneurysm. There are 5 types of endoleaks, with type 1 and 3 being the most severe as they can cause the aneurysm to enlarge and potentially rupture; type 1 endoleaks occur at graft attachment sites and type 3 endoleaks occur due to a defected graft or a disconnection between multiple grafts (England & Mc Williams, 2013). The different types of endoleaks are shown in Figure 1-5.

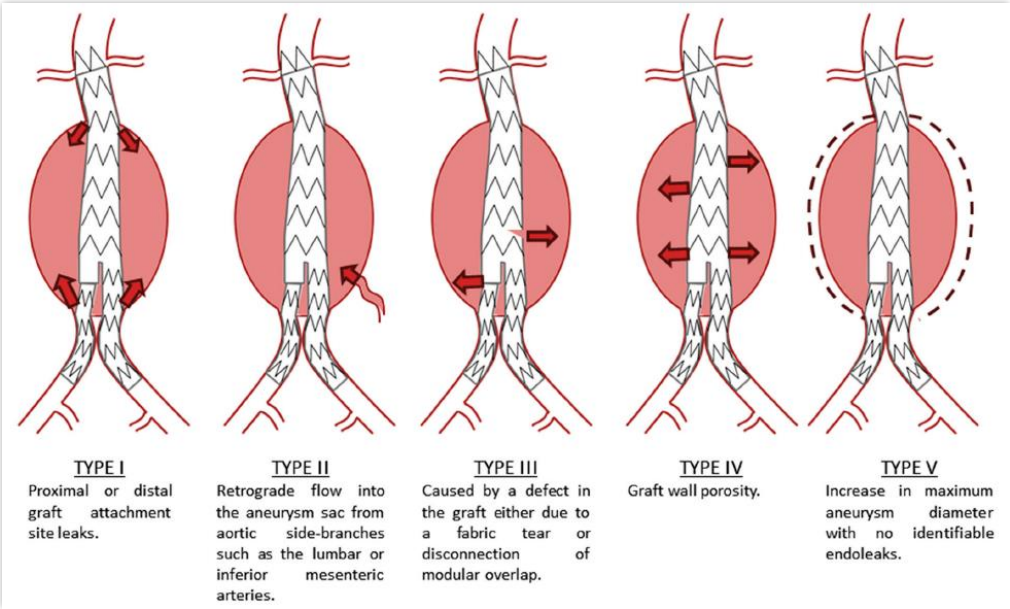

Figure 1-5 Stent-graft endoleak classifications (England & Mc Williams, 2013)

After Parodi, Palmaz, and Barone (1991) introduced the first EVAR procedure, there has been significant technological advancements in stent-graft technology as well as in catheter delivery

systems (Arslan et al., 2009). Dake MD, Miller DC, and Semba CP (1994) introduced the first TEVAR procedure using woven Dacron™ grafts attached to Z-shaped stainless steel stents using various interrupted 5-0 polypropylene sutures. Their endovascular stent-grafts were implanted into 13 patients and the results are shown in Table 1-3. They have used the femoral artery and aorta for access, delivering stent-grafts with diameters between 30 mm and 45 mm in various lengths. 12 out of 13 cases showed complete thrombosis of the aneurysm, although around half of the patients experienced post-surgery complications. After many years of testing, the first US Food and Drug Administration (FDA) approved commercial device for the TEVAR procedure was in 2005 (Desai et al., 2015).

EVAR procedures can also be used to treat aneurysmal complications such as aortic dissections before they cause the aorta to rupture. Due to the curvature of the aortic arch, type A aortic dissections require open-surgery, whilst type B aortic dissections, such as those caused by AAA's and TAA's, can be treated with EVAR procedures. A successful case of the TEVAR procedure on an acute case of type B aortic dissection is shown in the 3D reconstructed CT scan images in Figure 1-6.

Table 1-3 Results of 13 patients with TAA's treated using the TEVAR procedure (Dake MD et al., 1994)

Patient No.	**Characteristics of Stent-Grafts**				**Extent of Aneurysm Thrombosis**	**Complications**	**Length of Follow-up (months)**
	Access Artery	**No. of Devices**	**Diameter (cm)**	**Length (cm)**			
1	Femoral	1	3.2	10.0	Complete	Transient chest pain	24
2	Femoral	1	3.2	10.0	Complete	None	15
3	Femoral	2	3.2, 3.8	8.0, 8.0	Complete	Transient chest pain	13
4	Femoral	1	3.0	16.0	Complete	Transient chest pain	13
5	Aorta	1	3.4	12.5	Complete	None	11
6	Aorta	2	4.5, 4.5	7.5, 7.5	Complete	2nd procedure needed	10
7	Femoral	2	3.0, 3.8	5.0, 10.0	Complete	2nd procedure needed	10
8	Femoral	1	3.8	15.0	Partial	None	9
9	Femoral	1	3.4	15.0	Complete	None	9
10	Femoral	1	3.6	9.0	Complete	None	8
11	Femoral	1	4.0	12.5	Complete	Pleural effusion	8
12	Aorta	1	3.2	9.0	Complete	None	6
13	Aorta	2	3.2, 3.4	9.0	Complete	None	6

Figure 1-6 3D reconstructed CT scan images of A) an acute case of type B aortic dissection, and B) results after stent-graft implantation using the TEVAR procedure after 1 year (M.-H. Zhang et al., 2017)

1.1.3. Current technology

As of 2009, there were five EVAR devices (Medtronic AneuRx, W.L. Gore Excluder, Cook Zenith, Endologix Powerlink, and Medtronic Talent), and three TEVAR devices (W.L. Gore TAG, Cook TX2, and Medtronic Talent) approved by the US Food and Drug Administration (FDA) (Arslan et al., 2009). The top 3 key vendors for EVAR/TEVAR devices are Cook Medical, Gore Medical and Medtronic; other prominent vendors include Bolton Medical, Gamida Cell, JOTEC, Maquet and MicroPort (Technavio, 2016).

A study by Morris, Stefanov, Hynes, Diethrich, and Sultan (2016) tested four bifurcated stent-grafts (Medtronic Endurant II, Gore Excluder, Cook Zenith, and Cordis Fortron) and a multi-layer flow modulator (MFM) device used to treat AAA's, as shown in Figure 1-7. The stent-graft characteristics are shown in Table 1-4.

From the table, the most commonly used graft material is woven polyester except in the Excluder, where expanded polytetrafluoroethylene (ePTFE) is used. The stent materials used were cobalt alloy, stainless steel and Nitinol, and they were all self-expanding type stents; where the transformation temperature for the Nitinol used was above 30℃, and cobalt alloy and stainless steel stents were pre-deformed to create the self-expanding effect. The wall thickness of the stent-graft varies between 0.4 mm to 0.7 mm.

Table 1-4 Characteristics of 5 endovascular stent-graft and MFM devices for the treatment of AAA's (Morris et al., 2016)

Device features	MFM	Endurant II	Excluder	Zenith	Fortron
IFU aortic vessel diameter (mm)	24-28	23-25	24-26	23-24	23-27
Maximum proximal diameter (mm)	30.0	28.0	28.5	28.0	30.0
Maximum distal diameter (mm)	16.0	16.0	14.5	14.0	16.0
Device length (mm)	150	170	160	184	200
% Degree of oversizing (IFU)	25.0	17.0	18.8	17.0	25.0
Uncovered fixation length (mm)	-	15	0	30	30
Fixation type	Radial force	Radial force, barbs	Radial force, barbs	Radial force, barbs	Radial force, barbs
Proximal fixation location	Suprarenal	Renal	Infrarenal	Suprarenal	Suprarenal
Stent material	Cobalt alloy	Nitinol	Nitinol	Stainless steel	Nitinol
Fabric material	-	Woven polyester	ePTFE	Woven Polyester	Woven Polyester
Measured wall thickness (mm)	0.7	0.5	0.4	0.4	0.5
Activation type	Self-expanding	Self-expanding	Self-expanding	Self-expanding	Self-expanding
Activation temperature (℃)	-	>30	>30	-	>30

Note: IFU = instructions for use; ePTFE = expanded polytetrafluoroethylene

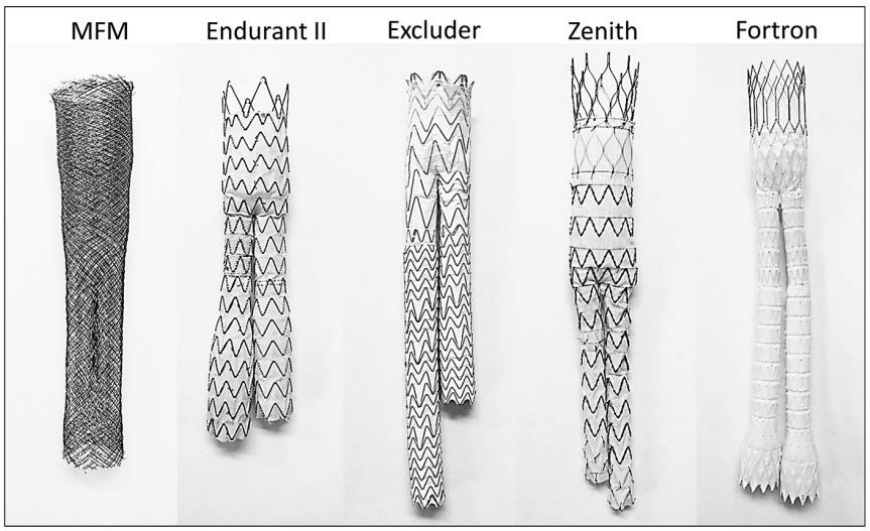

Figure 1-7 Endovascular stent-graft and MFM devices for the treatment of AAA's (Morris et al., 2016)

In order for the stent-graft to effectively seal against the wall of the aorta and reduce the risk of type I endoleaks, manufacturers recommend oversizing the diameters of the stent-graft. From Table 1-4, the percentage of oversizing is between 17 to 25 %. However, too much oversizing is also detrimental, as this could cause the graft to kink and do not seal properly, and under-sizing causes large gaps between the graft and the aorta, also causing insufficient seal, as shown in Figure 1-8.

a) 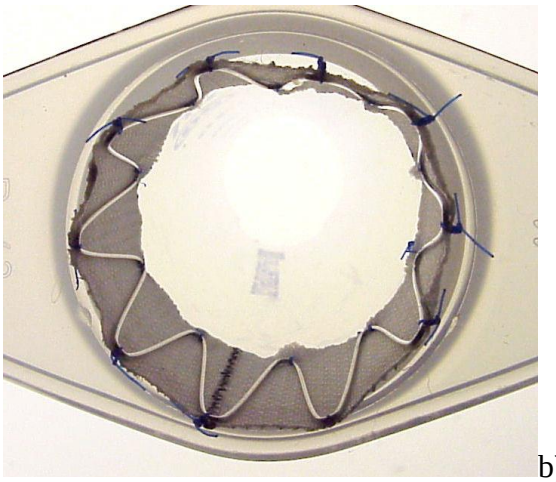 b) 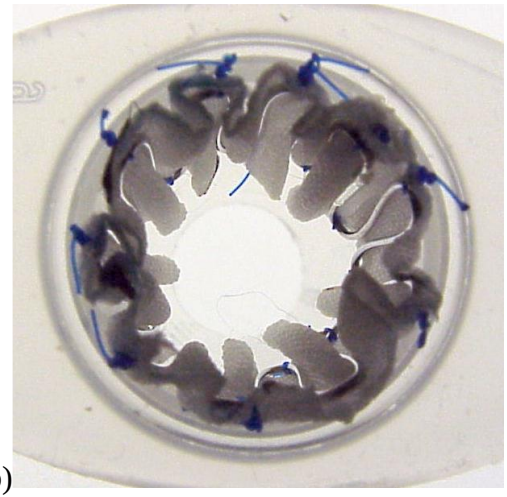

Figure 1-8 a) diameter undersizing, b) excessive oversizing (CookMedical, 2011)

A few examples of current standard EVAR and TEVAR devices are shown in Table 1-5 and Table 1-6 respectively.

Table 1-5 Examples of current EVAR stent-grafts and specifications (Rabih A Chaer, 2018)

Endograft	Materials graft/support	Suprarenal fixation	Active proximal fixation	Native aortic neck diameter (range in mm)	Native iliac diameter (range in mm)	Max introducer diameter (French, OD)	Potential advantages
Endurant (Medtronic)	Dacron/electropolished nitinol	Yes	Yes	19 to 32	8 to 25	20	Indications include short (10 mm) aortic neck, angulated neck
AFX2 (Endologix)	PTFE/cobalt chromium alloy	Yes	No	18 to 32	10 to 23	17	Anatomic fixation at bifurcation, low profile
Ovation (Endologix)	PTFE/nitinol	Yes	Yes	16 to 30	8 to 20	15	Low profile, proximal sealing ring
Excluder (Gore)	PTFE/nitinol	No	Yes	19 to 29	10 to 18.5	20	C3 delivery system, ability to recapture and reposition body, delivery sheath with hemostatic seal
Zenith (Cook Medical)	Dacron/stainless steel	Yes	Yes	18 to 32	8 to 20	26	Spiral Z flexible limbs
Zenith fenestrated (Cook Medical)	Dacron/stainless steel	Yes	Yes	19 to 31	9 to 21	20	Juxtarenal aneurysm
Aorfix (Lombard)	PTFE/nitinol	No	Yes	19 to 29	8 to 19	22	Flexibility, angulated neck
Incraft (Cordis; investigational device in the United States)	Dacron/nitinol	Yes	No	27 to 31	10 to 24	16	Ultra low profile

Table 1-6 Examples of current TEVAR stent-grafts and specifications (Ronald M Fairman, 2018)

Endograft	Materials graft/support	Proximal fixation	Distal fixation	Diameters (range in mm)	Lengths (range in mm)	Introducer diameters (French, OD)	Potential advantages
TAG (Gore)	ePTFE/nitinol+FEP	Yes	Yes	26 to 45	100 to 200	20 to 24	ePTFE+FEP reinforcing sleeve reduces risk of type IV endoleak
CTAG (Gore)	ePTFE/nitinol+FEP	Yes	Yes	21 to 45	100 to 200	20 to 24	better conformability
Zenith TX2 (Cook) 2 piece system (proximal/distal)	Dacron/stainless steel Z stent	Yes	Yes	28 to 42	120 to 216	20 or 22	Staight + tapered components available
Zenith Alpha (Cook) 2 piece system (proximal/distal)	Dacron/stainless steel Z stent	Yes	Yes	18 to 46	105 to 160	16 to 20	low profile, better conformability
Valiant (Medtronic)	Dacron/nitinol	Yes	Yes	22 to 46	105 to 212	22 to 25	Improved flexibility and conformability,
Relay (Bolton)	Dacron/nitinol	Yes	No	22 to 46	100 to 250	20 to 26	Improved longitudinal stength

FEP: fluorinated ethylene propylene

ePTFE: expanded polytetrafluoroethylene

The majority of the available stent-grafts are standard or off-the-shelf devices. However, due to variations in human anatomy and the varying locations for arterial branches, these devices may not always provide the perfect fit. Therefore, to a certain extent, when these devices are used in TEVAR/EVAR procedures, they are customized/modified in some way. The degree of customisation could vary from only changing the diameters of the device, to adding fenestrations, branches, and combining different stent-grafts to achieve the desired effect. (Timothy, 2016)

Efforts have been made by companies to customize standard devices to make them compatible with each patient's anatomy. A few examples are shown in Figure 1-9 to Figure 1-12. The Cook Medical Zenith and Vascutek Anaconda stent-grafts were modified with custom fenestrations, the Jotec stent-graft was customised with branches, and the Bolton Medical (now Terumo) aortic arch stent-graft was modified with branches to accommodate the carotid arteries (Timothy, 2016).

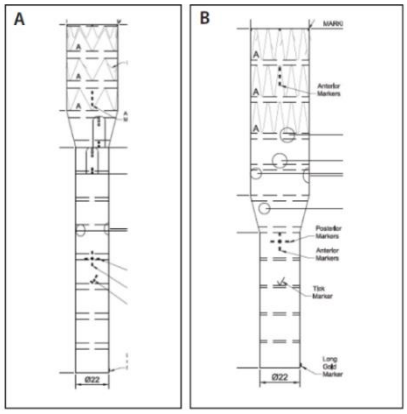

Figure 1-9 Cook Medical Zenith low-profile stent-grafts with custom fenestrations (Timothy, 2016)

Figure 1-10 Jotec custom stent-graft with branches (Timothy, 2016)

Figure 1-11 Vascutek Anaconda stent-graft with custom fenestrations (Timothy, 2016)

Figure 1-12 Bolton Medical aortic arch stent-graft with two branches (Timothy, 2016)

Some efforts have also been made by physicians to modify standard stent-grafts; using manual measurements from CT images, modifications for side branches were made. However, manual measurements possesses a large degree of human error. A more sophisticated method for creating a custom physician-modified stent-graft using a 3D printed template sleeve with fenestration holes was developed, and is shown in Figure 1-13. The CT image of the patient's aorta was used to create a 3D model (A) of a sleeve with accurately placed holes for fenestrations. This sleeve was then 3D printed (B), placed over a standard AAA bifurcated stent-graft (C), the holes were marked, and the fenestrations were cut-out after removing the template. (Leotta DF, 2015)

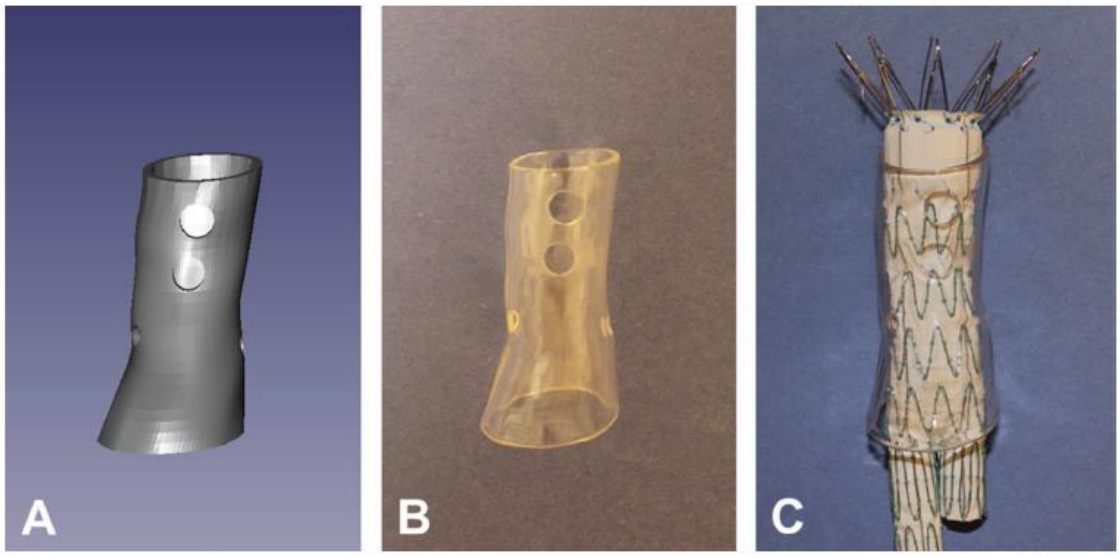

Figure 1-13 Physician modified stent using custom 3D printed fenestration template. A) 3D model, B) 3D printed template, C) 3D printed template placed on standard AAA bifurcated stent-graft (Leotta DF, 2015)

However, these physician-modified devices may still contain some degree of human error, and due to these standardized sizes and geometries, they still may not conform to the patient's anatomy. Thus, the idea of creating patient-specific devices was proposed to create stent-grafts tailored to each individual patient's anatomy.

The method of electrospinning patient-specific devices have been applied in the patent WO 2017/035500 A1 (Krieger et al., 2017) to tissue engineered vascular-grafts (TEVG), but no reference on the application to EVAR/TEVAR stent-grafts have been found.

1.1.4. Endovascular Stent Reinforcements

According to Moravej and Mantovani (2011), the metal stents for EVAR devices are most commonly made of corrosion-resistant materials such as SS316L, Nitinol (Nickel-Titanium) and cobalt-chromium alloy. These materials provide a permanent fixture that provide structural

rigidity for the graft, preventing it from collapsing after it is deployed. Stainless steel and cobalt chromium stents can be self-expanding (to an extent) when designed with a degree of pre-deformation, and a pattern that produces spring like effects (sinusoidal pattern), or they can be expanded with a balloon catheter. The Z-shaped stainless steel stent by Dake MD et al. (1994) mentioned previously is shown in Figure 1-14. Stent-grafts using the abovementioned metals were shown in Figure 1-7 and Table 1-4.

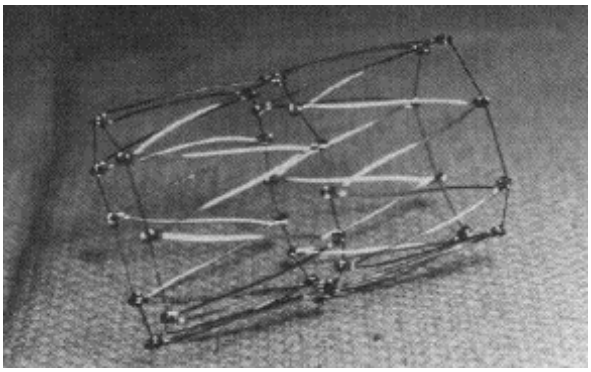

Figure 1-14 Z-shaped stainless steel stent, reproduced with permission from (Dake MD et al., 1994), Copyright Massachusetts Medical Society

Nitinol is an alloy with close to equiatomic composition of Nickel and Titanium (50:50 at% Ni & Ti). It is a particularly interesting metal, as it possesses both shape-memory and super-elastic properties due to its two phase, temperature dependent crystal lattice. The former is caused by a Martensitic B'19 monoclinic crystal structure, and the latter by an Austenitic B2 ordered crystal structure (Figure 1-15). Nitinol also has different phase transition temperatures (typically 20-30℃) between austenitic and martensitic phases (thermal hysteresis, see Figure 1-16). In some cases there is an intermediate phase (R phase) between the austenitic and martensitic phases that is martensitic in nature, which causes a two-stage transformation. (Memry, 2017)

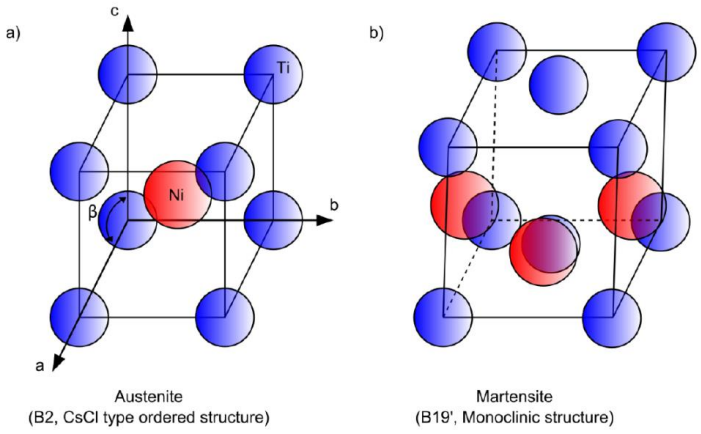

Figure 1-15 Crystal structure of Nitinol, a) austenitic phase, b) martensitic phase (Memry, 2017), Copyright Memry

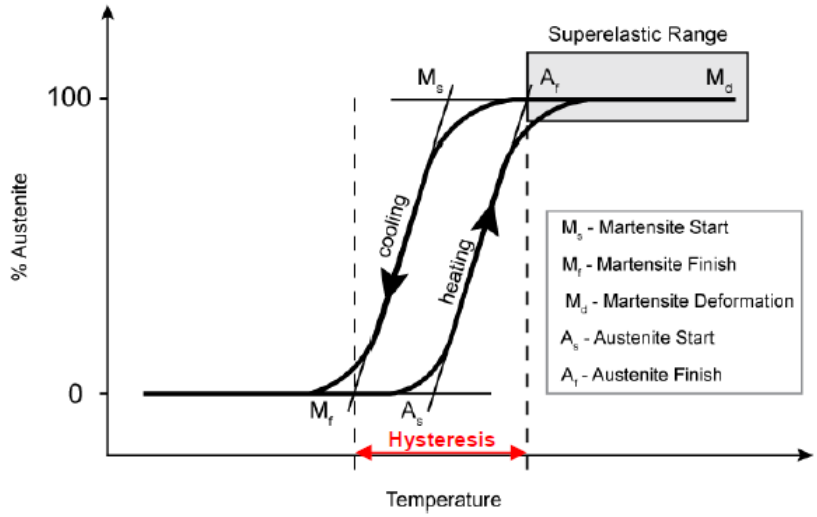

Figure 1-16 Typical Nitinol stress-strain curve (Memry, 2017), Copyright Memry

In the martensitic phase, Nitinol is malleable and retains the deformed shape. When heated above the austenite final (Af) temperature into the austenitic phase, stresses applied (up to 8% strain, above which plastic deformation occurs) will be converted to a stress induced martensite (SIM) which causes superelastic behaviour (spring-like property); the crystal structure reorganises into the ordered B2 structure, transforming the deformed Nitinol back to its original heat-set shape (shape-memory effect). When cooled below the martensite final (Mf) temperature, it returns to the malleable martensitic phase (Memry, 2017). The transformation temperatures can be varied with different percentages of Ni:Ti composition (FWMetals, 2017).

The shape setting temperatures can range between 400-500°C, with a heat-set time ranging from a minute to above 20 minutes (JohnsonMedicalComponents, 2018b) (Gilbert & Webster, 2016). However, manufacturers recommend heat setting at approximately 500°C for at least 5 minutes (JohnsonMedicalComponents, 2018b). The Nitinol is quickly quenched after heat setting, which allows it to retain the heat-set shape. The heat treatment temperature, duration as well as the methods used will also produce varying results of transformation temperature, peak force and plateau stress (JohnsonMedicalComponents, 2018b).

These properties of Nitinol make it particularly useful as a stent material because it can be crimped down to fit inside a smaller gauge catheter, and automatically return to the heat-set shape once delivered to the target location. This is either due to the body temperature raising the temperature of the stent above the Af temperature (martensite to austenite), or the stent used is already in its superelastic (austenite) state at room temperature, allowing it to automatically expand to its heat-set shape when the catheter is removed.

Nitinol is also highly biocompatible; the Nickel and Titanium bond is very strong so the Nickel has a very low reaction with the human body, making it suitable for biomedical applications. (JohnsonMedicalComponents, 2018a)

A newer shape-memory alloy of Nickel-Titanium-Cobalt (NiTiCo) compositions produces a higher modulus of elasticity, but contains 1.2-1.5 wt% Co (Memry, 2017), which exceeds the limit of the ASTM F2063 standards for medical devices and surgical implants (maximum allowable trace 0.05 wt% Co).

1.1.5. Endovascular Graft Scaffolds

Currently, for larger arteries (more than 8 mm in diameter), Dacron™ and ePTFE are the most common materials used for vascular grafts as seen in Table 1-7. Both materials have the properties of being hydrophobic with high crystallinity (Chlupac, Filova, & Bacakova, 2009).

Table 1-7 Recommended vascular graft materials depending on body region (Chlupac et al., 2009)

	Vascular regions				
Vascular substitute choice	**Large-calibre arteries (≥ 8 mm)**	**Medium-calibre arteries (6-8 mm)**	**Small-calibre arteries (≤ 6 mm)**	**Venous reconstructions**	**Haemodialysis arteriovenous access**
	Aorta, arch vessels, iliac and common femoral arteries	Carotid, subclavian, common femoral, visceral and above-the-knee arteries	Coronary, below-the-knee, tibial and peroneal arteries	Superior and inferior vena cava, ilico-femoral veins, portal veins, visceral veins	Upper > lower extremity
1st choice	Prosthesis (Dacron, ePTFE)	Prosthesis or autograft (equal)	Arterial or venous autograft	Saphenous spiral vein graft, deep venous autograft	Native material
2nd choice	Allograft, deep venous autograft	Prosthesis or autograft	Composite graft, vein interposition, prosthesis (ePTFE, Dacron), allograft, biosynthetic	Allografts, ePTFE, Dacron, biografts	ePTFE, PU, xenografts, biografts, TEBV (clinical trial)

ePTFE (expanded polytetrafluoroethylene), PU (polyurethane), TEBV (totally-engineered blood vessels)

DuPont patented polyethylene terephthalate (PET) under the name Dacron™ in 1950. It is a thermoplastic polymer under the polyester family. It is used to create synthetic fibres that can be woven or knitted. Woven Dacron™ has a lower porosity compared to knitted Dacron™. The porosity allows for cell ingrowth and eventually endothelial and smooth muscle layers can form. (Chlupac et al., 2009)

DuPont also patented PTFE as Teflon in 1937 and Gore patented ePTFE as Gore-Tex in 1969. ePTFE is very stable in biological environments and are less susceptible to deterioration in these environments compared to Dacron™ (Guidoin et al., 1993). A graft made with ePTFE will react less with blood components due to the graft surface being electronegative. It usually has an internodal distance (IND) between 30 to 90 µm, which is used to describe its average porosity. (Chlupac et al., 2009)

Dacron™ and ePTFE was found to perform equally well as vascular grafts (Roll et al., 2008).

Electrospinning is another way of creating fibrous and porous scaffolds for vascular grafts; allowing mimicry of native tissue mechanical properties, and cell ingrowth (Hasan et al., 2014). In this process, a syringe with a needle is filled with polymer solution, connected to a syringe pump to set the flow rate. The needle and the spinning mandrel/collector are electrically charged with opposite charges, which causes the polymer solution to be attracted to the mandrel. With the correct settings, the polymer solution forms a cone in front of the needle. A fibre forms from the cone as it whips and dries in the air towards the mandrel, which wraps around the mandrel, and over time, this creates many fused fibrous layers, forming a fibrous scaffold. The basic electrospinning setup is shown in Figure 1-17.

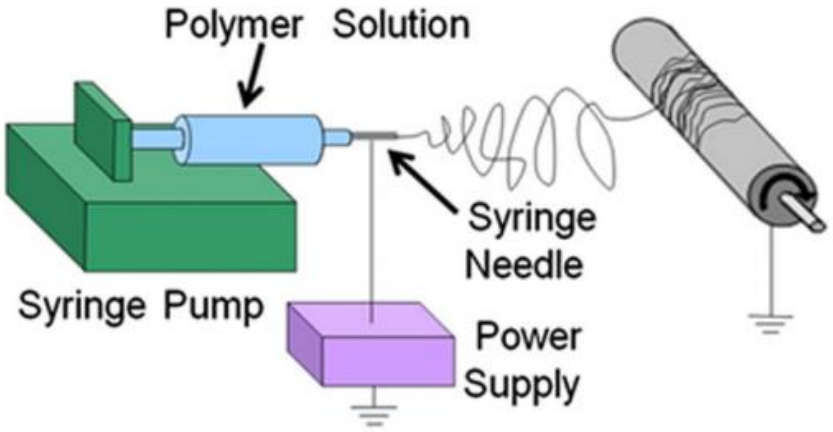

Figure 1-17 Electrospinning setup (Hasan et al., 2014)

Efforts are continuously being made to improve electrospinning techniques to create specific fibre orientation and sizes by varying process conditions such as applied voltage, distance between collector and the needle, and the flow rate; environmental conditions such as humidity and temperature also affects the outcome of electrospinning (Kishan A, 2017).

Although other methods are useful and suitable to produce other scaffold morphologies, 3D printing and dip-coating methods are not suitable to obtain the micrometre sized non-woven and microporous structures obtainable by electrospinning. Since endothelialisation is desirable, porous scaffold structures are crucial for the success of the implanted stent-graft, thus the use of electrospinning is more advantageous over other methods.

1.2. Research Proposal

1.2.1. Problem Statement

The EVAR stent-graft devices should conform to, and seal and fixate securely on the patient-specific anatomy.

However, current EVAR procedures mostly involve standard, off-the-shelf devices, which are cylindrical in nature. Patient-specific anatomies differ from person to person, and standard devices may not provide the perfect fit for every patient. Current custom devices are also time consuming to produce, and still may not be very accurate. The mismatch in conformity results in problems such as endoleaks and stent-graft migration, thus causing possible post-operative device failures, as well as mortality.

Thus, this study proposes to provide proof of concept of rapidly creating a relatively low-cost patient-specific EVAR stent-graft that conforms to each individual patient's anatomy, thereby potentially improving EVAR procedure success rates, and minimising the risk of post-surgery complications.

1.2.2. Objectives

The following objectives were formulated for this project:

- Define patient-specific geometry
    - Obtain computed tomography (CT) scan
    - Digitise and 3D reconstruction
        - Blood model
        - Aortic model
    - Design patient-specific stent-graft geometry from blood model
        - Computer aided design (CAD) software
- Fabricate electrospinning mandrels
    - Additive manufacturing using a fused deposition modelling (FDM) 3D printer
    - Mandrel material determination
    - Idealised graft geometry
    - Patient-specific graft geometry
- Electrospin luminal layer on electrospinning mandrel
    - Manufacture/implement humidity control
    - Electrospinning parameters
    - Pellethane solution

- Determine effect of idealised geometry on scaffold morphology and mechanics
    - Mechanical test
    - Fibre morphology evaluation
        - Coherency
        - Fibre diameter
        - Pore size
- Develop Nitinol stent rings
    - Heat set mandrel design and manufacture
    - Stent pattern design
    - Stent winding
    - Heat-set stents – fluidised bath
    - Nitinol transformation temperature determination
- Determine effect of Nitinol stent pattern on mechanical properties
    - Radial force testing of individual stent rings
- Incorporation of Nitinol into patient-specific stent-graft
    - Attachment by overspinning
    - Radial force testing of stent-grafts
    - Stent-graft delamination resistance determination
- Finite element analysis (FEA) simulation
    - Compare simulation and experimental radial force test results
- Mock insertion of patient-specific stent-graft in hollow aortic model
    - 3D printed transparent aortic model

2. Materials and methods

The following sections will describe the methods used to manufacture patient-specific EVAR stent-grafts, which involved obtaining the patient-specific aorta geometry, converting it to a blood and a hollow aortic model, designing the patient-specific stent-graft geometry, 3D printing into an electrospinning mandrel, electrospinning the luminal layer of the graft scaffold, heat-setting and attaching the Nitinol stent on the luminal layer, and overspinning with the abluminal layer. Various idealised geometries (tapered, curved, elliptical) were used as electrospinning mandrels to simulate features of patient-specific aortic geometry. Hollow aortic model was then used for mock insertion.

2.1. Patient-Specific Models

Dr Nikolaus Thierfelder (Munich University) provided the aortic models used in this study (CT scan data, 3D-reconstructed-CT-scan computer-aided design (CAD) models, and patient-specific stent-graft design stereolithography (STL) files). These scans were from anonymous patients and ethics approval was received from the Human Research Ethics Committee (HREC Ref: 273/2018, valid until May 2019).

2.1.1. Blood Model 3D Reconstruction

The aortic blood volume from each slice of the CT scan data (Siemens SOMATOM definition CT scanner) was determined by its grey values and isolated, the total blood volume was calculated (Figure 2-1), reconstructed into a 3D CAD blood model using automated functions in Materialise Mimics (software package to convert medical image files to 3D models), and the surface quality was improved using the smoothing tool (Figure 2-2).

a) 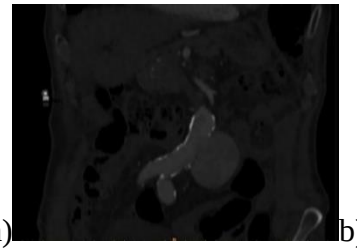 b) 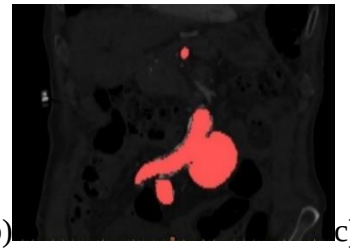 c) 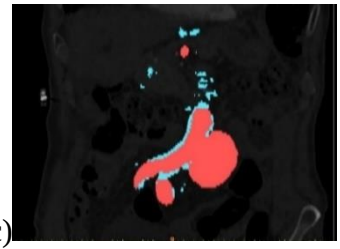

Figure 2-1 a) CT scan image in the abdominal region, frontal plane, b) main aortic blood volume region identified, c) calculated total relevant aortic blood volume

a) 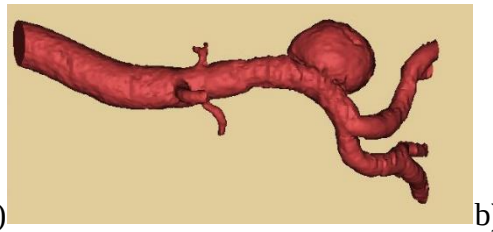 b) 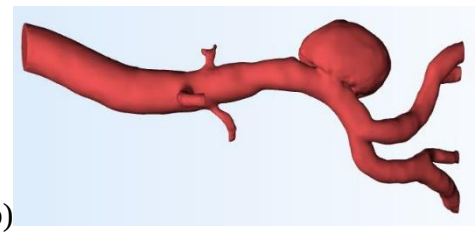

Figure 2-2 a) reconstructed 3D aortic blood model from CT scan images, b) smoothed blood model

2.1.2. Hollow Aortic Model

Hollow aortic models were designed in Mimics, the hollowing tool was used to extend the surface of the blood model outwards, which formed the outer aortic wall, and the original surface was then inverted and used as the inner aortic wall. The ends of the hollow model were trimmed using reference planes and the surface quality was improved using a smoothing tool.

2.1.3. Stent-Graft Geometry Design

An initial attempt was made to create a patient-specific stent-graft geometry from a TAA blood model by importing the STL file into SolidWorks, possible proximal and distal landing zones were identified, reference planes were placed across each end of the landing zones, the spline tool was used to trace and smooth the cross-sectional geometry, and the loft tool was used to join the two cross-sections with the curvature of the aorta as a guide curve. The thoracic aorta blood model is shown in Figure 2-3.

A model from a patient with AAA was also investigated, herein referred to as P16. The patient-specific stent-graft geometry design was created in Mimics; areas above and below the aneurysm with normal cross-sectional diameters (proximal and distal landing zones) were identified, the aneurysm was removed using a brush tool on each layer of the CT scan, and the ends of the landing zones were trimmed using reference planes, which left behind the native blood volume. Rough surfaces were removed using a smoothing tool. The outer surface was extended by 10 and 20% to create oversized stent-graft designs, the outline of the stent-graft geometry was then placed on the CT scan images to ensure the geometry of the aorta was conserved, see Figure 2-3. The patient-specific stent-graft geometries were then exported as STL files in Mimics for 3D printing into electrospinning mandrels.

To simulate features on patient-specific aortic geometries, 15 simplified graft geometries (one straight/cylindrical, five elliptical, four curved and five tapered geometries, see Table 2-1) were also designed in SolidWorks, herein referred to as idealised geometries. The naming convention uses the first letter of the geometry combined with the dimension that was varied, e.g. E10: elliptical, 35x10 mm, T20: tapered, 35 mm $Ø_1$, 20 mm $Ø_2$, C5: curved, 30 mm Ø, 5 mm offset.

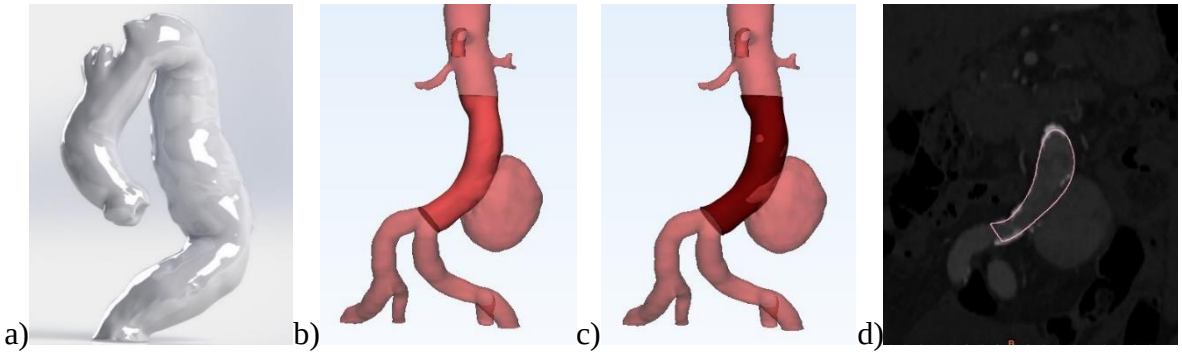

Figure 2-3 a) rendering of a thoracic aortic blood model with an aneurysm, b) P16 native blood volume over aneurysmal region, c) 10% oversized stent-graft design over aneurysmal region, d) outline of designed stent-graft geometry placed on CT scan image for evaluation

Table 2-1 idealised geometry mandrel variations

Letter	Mandrel shapes	Variation	Dimensions
S	Straight	Baseline	25 mm Ø; 100 mm L
E	Elliptical	Width	35 mm *l*; 10, 15, 20, 25, 30 mm *w*; 120 mm L
C	Curved	Offset from centre	30 mm Ø; 5, 10, 15, 20 mm offset; 120 mm L
T	Tapered	Diameter on one end	35 mm $Ø_1$; 10, 15, 20, 25, 30 mm $Ø_2$; 120 mm L

2.2. Electrospinning Mandrel

The patient-specific electrospinning mandrels were made using additive manufacturing (3D printing). Although metal mandrels would provide optimal results, the high cost and lack of facilities to produce these in-house, led to investigations into the use of various alternatives of 3D printed plastic mandrels, which were tested to determine their feasibility for use with electrospinning. The STL files were imported into the slicer software, converted to G-Code files, uploaded onto the 3D printer, and 3D printed.

2.2.1. 3D Printer

The 3D printer used was a DIYElectronics Prusa i3 FDM 3D printer (0.4 mm Ø nozzle, 1.75 mm Ø filaments, 250x270x200 mm build volume, aluminium bed), shown in Figure 2-4.

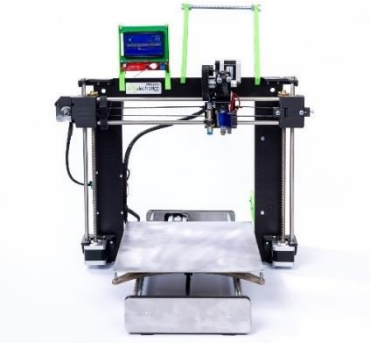

Figure 2-4 DIYElectronics Prusa i3 FDM 3D printer (DIYElectronics, 2019)

During initial print tests, it was discovered that vibrations caused by the movement of the nozzle in the x and y directions caused poor print quality; the effect of vibration increased at higher z values. An aluminium frame was designed, and built around the 3D printer using slotted 30 x 30 mm aluminium extrusions, as shown in Figure 2-5.

The extruder was additionally upgraded with 3D printed fan mounts and an airflow guide in order to help cool the part while printing, as shown in Figure 2-5.

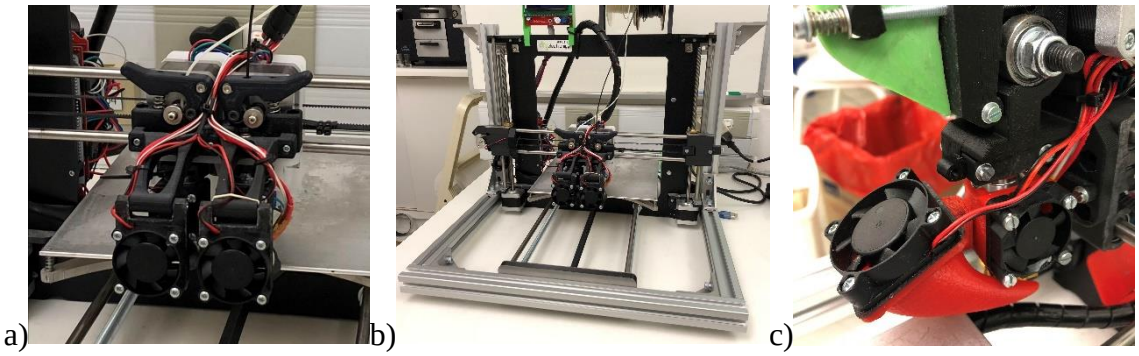

Figure 2-5 a) dual extruder upgrade, b) aluminium frame upgrade, c) print cooling fan mount upgrade

2.2.2. Electrospinning Mandrel Material

Non-conductive and conductive Polylactic Acid (PLA) 3D printing filaments were investigated for the use as electrospinning mandrels. Two tapered mandrels of each material were electrospun on (2 ml/hr, 260 mm needle distance to mandrel, 1000 rpm, 1.5 hours) to compare their resulting scaffolds.

2.2.2.1. Non-conductive PLA

Initial electrospinning mandrel prototypes were 3D printed using non-conductive PLA filaments (volumetric resistivity $\rho_v \approx 10^{15}\,\Omega$m (Zenkiewicz, Richert, Rytlewski, & Richert, 2011)), shown in Figure 2-6. Since the mandrels were non-conductive, perimeter holes (1-2 mm Ø) were then added along the mandrel design in an attempt to improve the electrical field around it by allowing direct access to the metal shaft inside.

Figure 2-6 3D printed non-conductive PLA mandrels

2.2.2.2. Conductive PLA

Proto-Pasta conductive PLA filament (conductive due to the addition of graphite, $\rho_v \approx$ 0.3-1.15 Ωm (ProtoPasta, 2019), compared to aluminium 2.65×10^{-8} Ωm (EngineeringToolBox, 2008)) was later discovered and used to 3D print the electrospinning mandrels. An example of a 3D printed conductive PLA mandrel is shown in Figure 2-7.

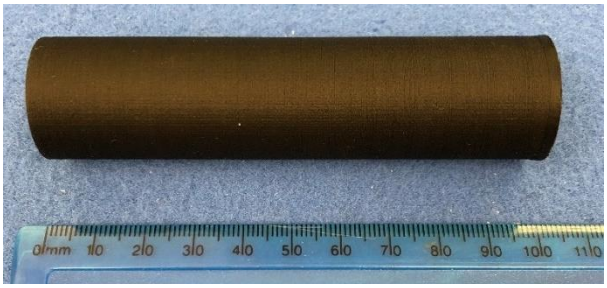

Figure 2-7 3D printed conductive PLA cylindrical mandrel

2.2.3. Surface Smoothing

Surface smoothing of the 3D printed conductive PLA electrospinning mandrels was achieved by removing large surface defects with a scalpel, sanding (100-1200 grit increments), and Tetrahydrofuran (THF) vapour smoothing.

Vapour smoothing was done by boiling THF in a tall beaker (66°C, 100 ml, under a fume extraction hood), which caused vapour to rise and fill the beaker, and the 3D printed mandrel was submerged in the vapour. Vapour condensation on the side of the beaker was used as a vapour level guide, once high enough to cover the length of the mandrel, it was carefully dipped (1-2 seconds) into the vapour (see Figure 2-8), air-cooled (10-20 seconds), recoated 2-3 times, and then air-dried completely (10 minutes). Excessive vapour smoothing was also investigated (10 second continuous in the vapour).

Figure 2-8 Vapour smoothing conductive PLA mandrel

2.2.4. 3D Printing Parameters

The STL files were converted to 3D printable G-Code files (Ultimaker Cura v3.6 slicer). The 3D printing parameters used were established after taking into consideration the printing material, speed of production, print quality, rigidity and cost savings. The details were as follows:

1. The nozzle temperature used was 230℃ for conductive PLA and 210℃ for non-conductive PLA. Due to the addition of graphite in the conductive PLA, a higher temperature was used to allow the molten plastic to flow more easily, which reduced the chance of the nozzle clogging, and created stronger bonds between each layer.
2. The build plate temperature used was 50℃. This improved the adhesion of the printed part to the build plate.
3. A 0.1 mm layer height was used. This was the highest resolution of the printer used; thinner layers created models with less visible layer lines, which improved the surface quality, although the printing time was increased.
4. The manufacturer's recommended print speed of 30 mm/s for conductive PLA was used (15 mm/s for the wall, which improved the surface quality of the printed part). Although higher print speeds (up to 60 mm/s was investigated) was used with the non-conductive PLA to decrease the manufacturing time, the conductive PLA could not be 3D printed at this speed as it clogged up the nozzle frequently.
5. A 0.8 mm wall thickness (2 wall line counts) was used to provide an adequately sturdy shell for the mandrels, whilst minimising the material used.
6. An 8 mm brim was used which further aided the printed part in adhering to the build plate.
7. 1 mm top/bottom thickness and 20% infill were used to provide adequate structural support, whilst minimising the material used.

2.3. Electrospinning

Electrospinning was used to make the fibrous graft scaffold. The patient-specific geometries were electrospun on to form the luminal layer of the stent-graft. The following subsections cover the electrospinning equipment and polymer solution used, the environmental control system, various electrospinning parameters investigated, the basic electrospinning procedure, the investigation of the mandrel shape on the scaffold morphology, and the various mechanical tests performed.

2.3.1. Electrospinning Equipment

The electrospinning rig used consisted of a wooden box (830x735x700 mm) with glass doors enclosing the electrospinning stage (A) and mandrel, the humidifier (B), and the needle holder (C), as shown in Figure 2-9.

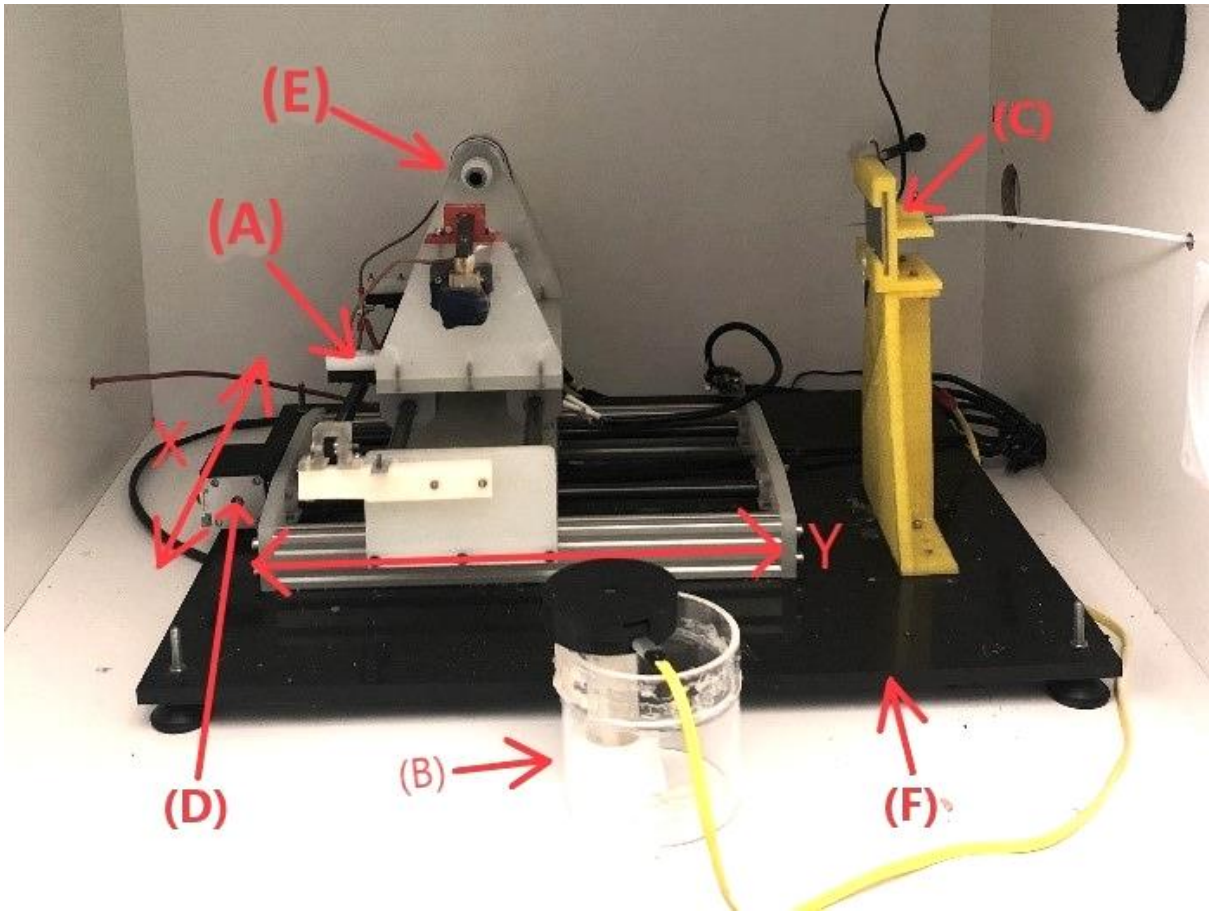

Figure 2-9 Electrospinning rig interior

The stage (A) moved in the x and y directions (actuated by two NEMA 17 (1.7 A, 4 kg.cm torque) stepper motors (D) connected to GT2 timing belts), which allowed the adjustment of mandrel to needle distance, and sideways translation of the mandrel. A rotating chuck (E) (attaching up to 8 mm Ø metal rods, actuated by an EMAX Grand Turbo GT2826/06 brushless motor connected to a GT2 belt and pulley system) mounted on the stage allowed the electrospinning mandrel to be attached and rotated. An Arduino Mega 2560 board, with a RAMPS 1.4 shield, mounted on the outside of the box controlled these electronics, supplied with a 12 V DC, 30 A power supply. (Refer to Figure 2-9 with corresponding labels)

The needle holder (C) (3D printed with non-conductive PLA, with a 60x60x3 mm metal plate with a 1 mm needle hole attached) screwed onto a large Perspex base (F) with multiple holes for position adjustment (Figure 2-9). Two GAMMA High Voltage Research power supplies

provided the electrical charge to the mandrel and needle. The positive high voltage power supply (Model: ES60P-20W/CIC2) was attached to the metal plate to evenly distribute the electrical charge to the needle. The negative high voltage power supply (Model: ES30N-20W) was attached to spring-loaded carbon brushes on each end of the mandrel. These opposing charges attracted the polymer solution through the needle to the mandrel.

Access holes around the electrospinning enclosure allowed the wires of the various electronics and the needle to pass through. All access holes were only large enough for the intended wires and the needle, which reduced leakage between the internal and external environment.

A Chemyx Fusion 100 syringe pump supplied the electrospinning polymer solution through a 20 ml BD syringe, connected to a blunted 18G needle via a length of Teflon tube (20-30 cm long, 1.75 mm ID). Teflon was used as it has high chemical corrosive-resistance and could handle the pressure applied by the syringe pump without bulging.

2.3.2. Environmental Control System

In order to improve the reproducibility and consistency of the electrospun graft scaffolds, an enclosure for the relative humidity (RH) regulating environmental control system was designed in SolidWorks, and manufactured (by Impressive Designs) into a transparent Perspex box, with various compartments to separate the different airflow pathways. The airflow pathway began at the inlet under the environmental control enclosure, through the carbon filter (Futurama Carbon Filter – 150x300 mm, 50 mm Carbon Bed) for solvent filtration, then flows either through the humidification and general air circulation pathway, or through the desiccant pathway for dehumidification, and finally through the outlet back into the electrospinning enclosure. The environmental control system is shown in Figure 2-10 on top of the electrospinning rig.

Two 120 mm, 12 V DC fans (Orion Fans, OD1238-12HBXC) were used to circulate the airflow; Fan 1 was used for humidification and general air circulation, and fan 2 purely for dehumidification. Two buck-modules (Texas Instruments, LM2596S) were used to regulate the fan speeds.

The fans and humidifier (humidifier shown in Figure 2-9(B)) were controlled using a temperature and humidity regulator (Comet Africa, H3021-4). Both fans were connected to relay 1; fan 1 on normally closed, fan 2 on normally open. The humidifier was connected to relay 2 on normally open. When relay 1 was triggered (RH>set-point 1, dehumidification process, 1% hysteresis, 1 second delay), fan 1 stopped, fan 2 started, and the humidifier

stopped. When relay 2 was triggered (RH<set-point 2, humidification processs, 1% hysteresis, 1 second delay), fan 1 started, fan 2 stopped, and the humidifier started. When the RH was between the set-points, only fan 1 was on for general air circulation.

A round hinged door was mounted after each fan, which opened outwards towards the outlet; since only one fan was in operation at a time, the backpressure closed the hinged door on the other fan; the main purpose was to prevent humidified air from flowing backwards through the desiccant chamber.

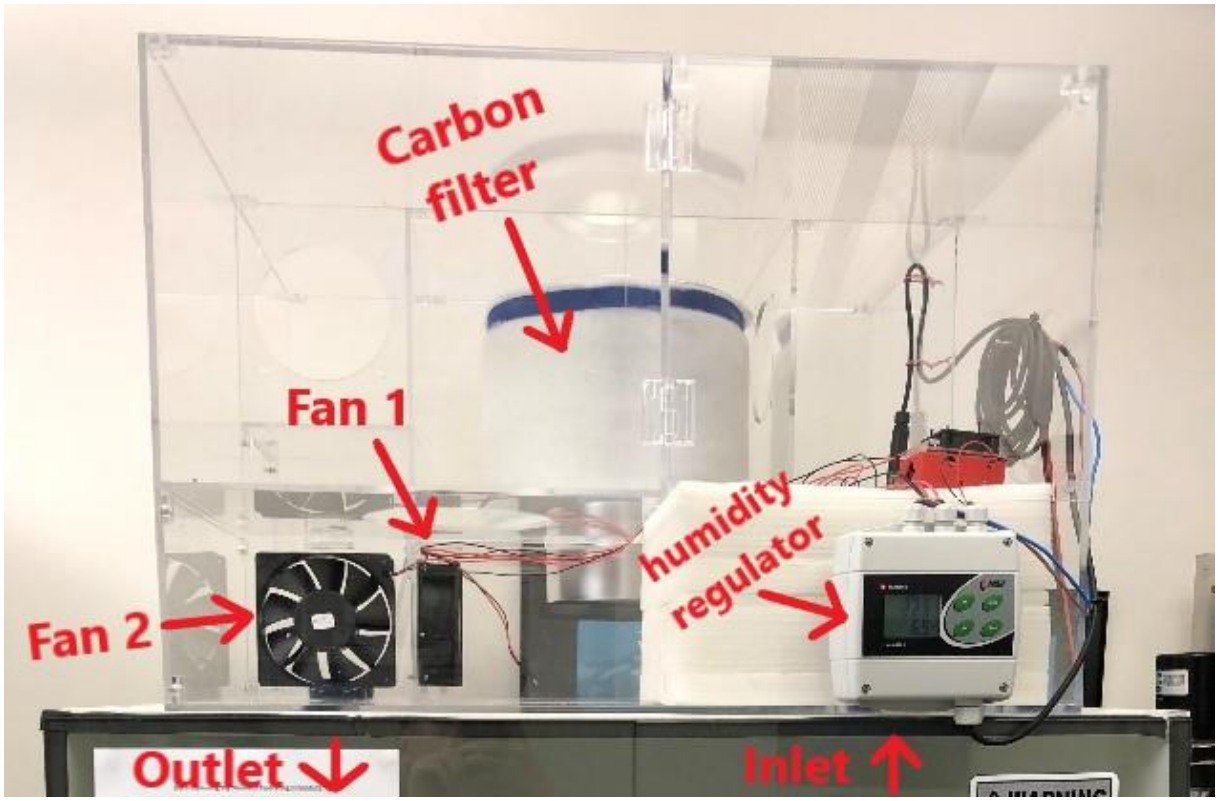

Figure 2-10 environmental control box on top of electrospinning rig

The efficiency of the environmental control system was investigated by varying the set point (40 to 70% RH) in 10-minute intervals (ambient: 54.8% RH, 23.3°C). The humidifier efficiency was investigated when the ambient RH was low (33% RH, 23.6°C) by using an extreme set point of 100% RH. Electrospinning results at different RH were briefly investigated. The scaffolds produced in this project were electrospun between 40 to 60% RH.

2.3.3. Electrospinning Polymer Solution

The electrospinning polymer solution used was made by dissolving 16 wt% Pellethane (thermoplastic polyurethane (TPU)) in a mixture (50:50 by weight) of Dimethylformamide (DMF), and THF, shaken in a Pyrex glass jar at room temperature for 24 hours, and then magnetically stirred until thoroughly mixed.

2.3.4. Electrospinning Parameters

Although not extensively tested, various electrospinning parameters and conditions were investigated by trial and error until an adequate electrospun porous graft scaffold was formed with uniform fibre deposition. The parameters investigated include the mandrel to needle distance (260 to 330 mm), positive and negative high voltage supply (13 to 22 kV, -3 to -5 kV), mandrel rotational speed (750 and 1000 rpm), syringe pump flow rate (2, 5 and 10 ml/hr), and oscillation speed (1, 5 and 10 mm/s).

After initial investigations, the idealised geometries were electrospun at 300 mm, +18 kV, -3 kV, 1000 rpm, 5 ml/hr, 5 mm/s, and the patient-specific P16 geometry at 290 mm, +18 kV, -3 kV, 750 rpm, 5 ml/hr, 5 mm/s.

The electrospinning time was calculated using the surface area of the geometries; samples were electrospun between two to four hours (2 ml/hr, tapered mandrel), a sample which retained the mandrel shape after removal was selected (≈0.3 mm), the surface area was divided by the spinning time (A/t) and used to calculate the spinning time for the other geometries, and corrected for a flow rate of 5 ml/hr. The equations used to calculate the surface area of various shapes are shown in Equations (2-1) to (2-3); surface areas of curved and complex geometry mandrels were obtained from the CAD models in SolidWorks.

Ellipse:

$$A = 2\pi L\sqrt{\frac{(R_1^2 + R_2^2)}{2}} \qquad (2\text{-}1)$$

where: L – length of mandrel, R1 – radius of major axis, R2 – radius of minor axis

Tapered:

$$A = \pi(r + R)\sqrt{(R - r)^2 + L^2} \qquad (2\text{-}2)$$

where: r – smaller radius, R – larger radius, L – length of mandrel

Straight/cylindrical:

$$A = \pi dL \qquad (2\text{-}3)$$

where: d – diameter, L – length of mandrel

2.3.5. Basic Electrospinning Procedure

The porous graft scaffolds were electrospun by first securing the electrospinning mandrel to the chuck (on 5 or 8 mm Ø stainless steel rods), the needle was inserted through the metal plate, the parameters (rotation speed, oscillation speed, mandrel distance and oscillation distance) were configured from the computer interface, and the electrospinning sequence was started. The Pellethane solution filled syringe was secured on the syringe pump, configured (syringe

size, volume of solution and pump speed), and started. The high voltage power supplies were switched on after the stage homing sequence was complete, and adjusted until the polymer solution forms a cone at the tip of the needle with a steady leading stream, see Figure 2-11.

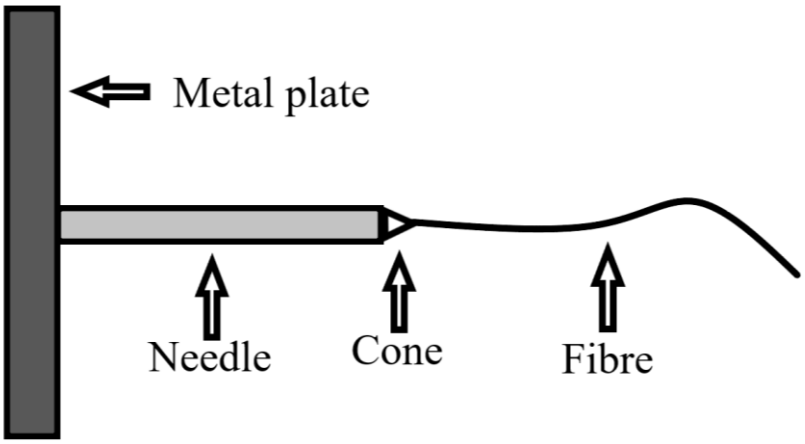

Figure 2-11 Illustration of polymer solution forming a cone at the needle tip

To remove the electrospun graft scaffold from the mandrel, the scaffold was air-dried (10 minutes), the ends were trimmed with a scalpel, and it was then easily rolled off. The graft scaffold was then re-inverted to the original conformation.

2.3.6. Effect of Mandrel Shape

To investigate the limits of electrospinning and fibre deposition due to geometry variations that represent features of patient-specific anatomy, the 15 idealised geometries were 3D printed as conductive PLA electrospinning mandrels (see Figure 2-12), and electrospun on; samples from various positions on each scaffold were tested, as illustrated in Figure 2-13.

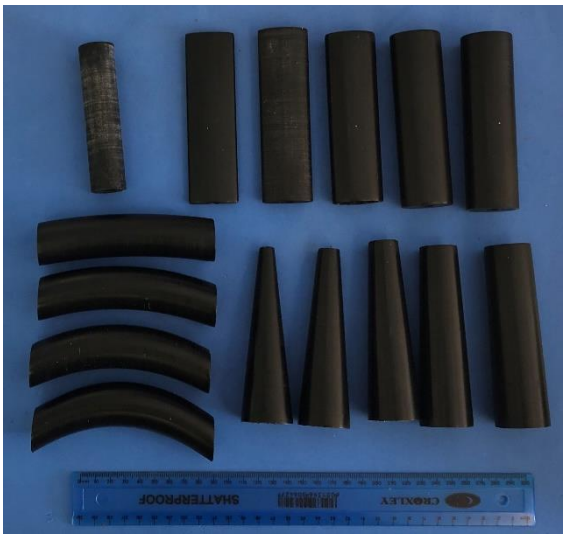

Figure 2-12 3D printed conductive PLA idealised geometry mandrels to model geometric features of patient-specific graft geometry

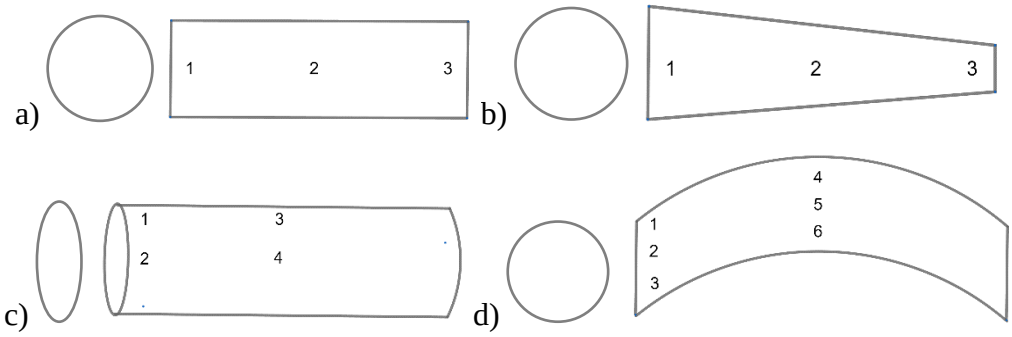

Figure 2-13 Position numberings for, a) straight, b) tapered, c) elliptical, and d) curved, mandrel geometries

Two mandrels with branches (90° and 45°) were also 3D printed and electrospun on (120 to 750 rpm) to investigate the possibility of electrospinning graft scaffolds to include branches or fenestrations, see Figure 2-14.

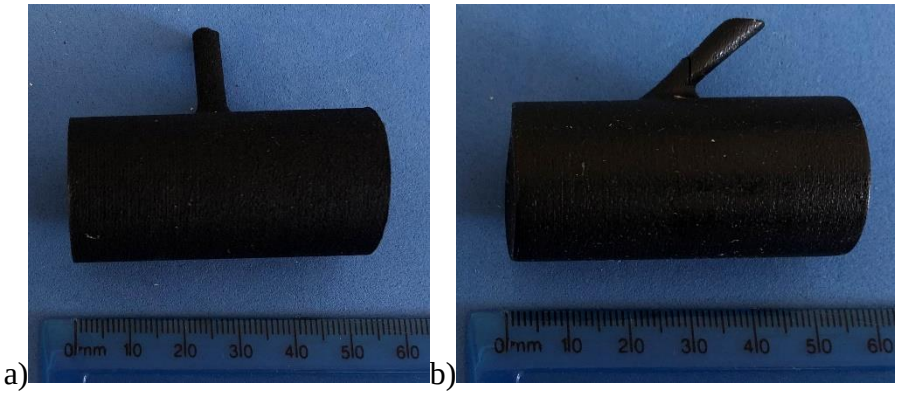

Figure 2-14 Conductive PLA mandrels with a) 90° branch, b) 45° branch

2.3.7. Tensile Testing

Tensile tests were performed on the electrospun graft scaffolds as well as on two commercial woven Dacron graft scaffolds. Dogbone samples (5 x 28 mm) were cut at the desired orientations (longitudinal and circumferential). The samples (10 mm initial gauge length) were preloaded (0.1 N), uniaxial extension was performed on an Instron (Model 5544, 2000 N load-cell) at a crosshead speed of 25 mm/min for electrospun scaffolds, 5 mm/min for commercial woven scaffolds (due to the electrospun scaffolds having a much higher elasticity, a faster testing speed was used), and was extended until a decrease in force of 99% was achieved (indicating break).

2.3.8. Fibre Morphology Evaluation

To evaluate the fibre morphology of the electrospun scaffolds, microscopic images were taken with a SEM, and the images were analysed using image processing software.

2.3.8.1. SEM Imaging

Microscopic images of the electrospun fibres were taken with a Jeol JSM-5200 (for electrospun scaffolds on the 15 idealised geometries) and a FEI Nova NanoSEM230 (field emission gun (FEG) tip, Everhart-Thornley detector (ETD)) (for patient-specific graft scaffolds, commercial graft scaffolds, and a sample electrospun on a non-conductive PLA mandrel) scanning electron microscopes.

Samples of the graft scaffold (inside/outside surfaces, and transverse/longitudinal cross-sections) were cut, arranged on a SEM stub as shown in Figure 2-15, sputter coated (Bio-Rad Polaron Division SEM Coating System, Argon gas, 1.4 kV, 15-20 mA, 5 minutes) and placed under vacuum in the SEM. The focus, contrast and brightness were adjusted accordingly, and images were taken at three different locations on each of the inside and outside surfaces, at the desired magnifications (100-1000X for cross-sections, 1000-2000X for the surfaces).

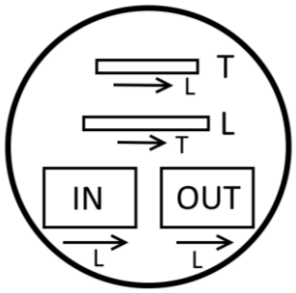

Figure 2-15 Sample arrangement on SEM stub

2.3.8.2. Image Processing

Fiji (Image J) image processing software was used to analyse the SEM images. The images of each sample were placed into separate folders, each folder was bulk analysed for fibre orientation (coherency expressed as orientation index (*OI*)), fibre diameter and pore size, using OrientationJ and DiameterJ plugins, as well as bulk processing macros (See APPENDIX). For the analysis of fibre diameter and pore size, the images were first segmented, and then processed with DiameterJ, the settings used are shown in Figure 2-16.

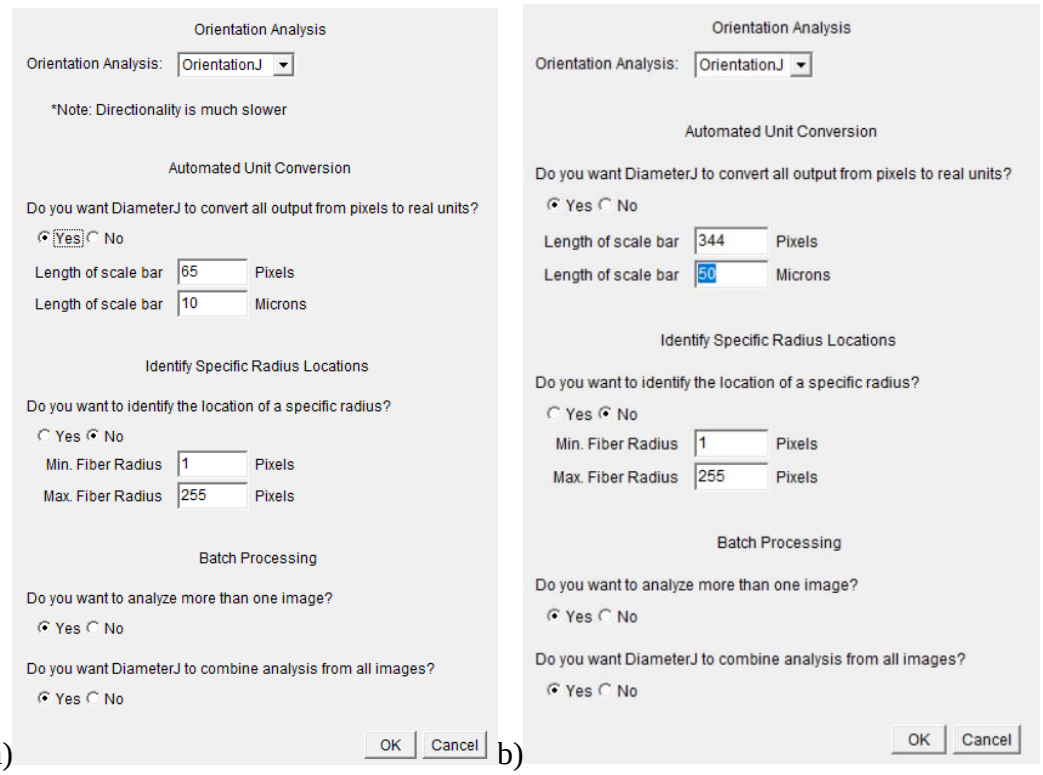

Figure 2-16 DiameterJ settings for, a) Jeol SEM 1000X images, b) Nova SEM 2000X images

2.4. Nitinol Stent Reinforcements

Nitinol stents can be made using laser cut Nitinol tubes (square cross-section) or wound Nitinol wire (round cross-section). Laser cut stents are more precise but at a much higher cost. For proof of concept, hand wound Nitinol wire stents were used.

2.4.1. Nitinol Heat-Set Mandrel

A heat-set mandrel was used to wind the Nitinol wire into patterns, which allowed the wire to retain the pattern during heat-setting. Patient-specific heat-set mandrels can be made using CNC machining, metal casting, or metal 3D printing etc. As an initial proof of concept, a more cost-effective option was used; 1 mm perimeter holes were drilled on a standard 25.4 mm OD (1 inch) aluminium tube, 1 mm slotted spring pins were then inserted as wire wrapping posts, see Figure 2-17. The location of the holes depend on the desired stent pattern.

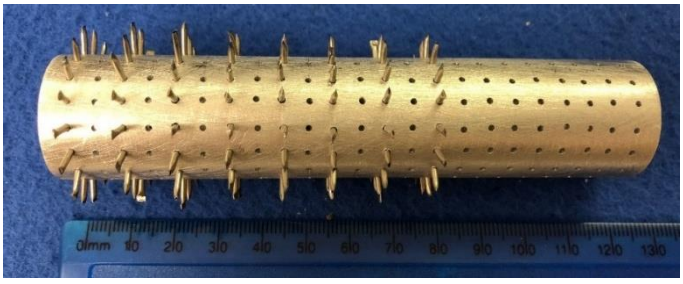

Figure 2-17 Standard 25.4 mm OD heat-set mandrel

2.4.2. Stent Patterns

Using commercial stent pattern designs as guidelines, sinusoidal pattern stent designs were used, see Figure 2-18.

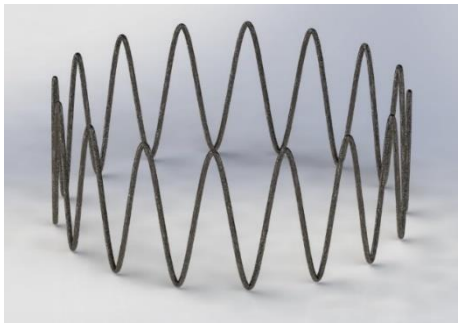

Figure 2-18 Sinusoidal stent pattern

To test the effect of stent pattern variations on the radial force produced, four parameters were individually investigated, which were the number of sinusoidal waves in one stent ring, the wire diameter, the stent height, and the percentage stent pre-deformation. The pre-deformation (PD) was the percentage oversize of the stent when it was heat-set, compared to the diameter of the stent-graft design it was electrospun into. Table 2-2 shows the matrix of the various stent patterns manufactured.

Table 2-2 Matrix of manufactured and tested stent pattern variations

Name	No. waves	Wire t (μm)	Stent height (mm)	Stent pre-deformation (%)
S25-STD	8	380	10	0
S25-D250	8	250	10	0
S25-D500	8	500	10	0
S25-12W	12	380	10	0
S25-16W	16	380	10	0
S25-H05	8	380	5	0
S25-H15	8	380	15	0
S25-PD10	8	380	10	10
S25-PD20	8	380	10	20

S25-STD was the standard/baseline design, with the wire thickness calculated as an equivalent diameter (380 μm) from the stent of a commercial AAA device with a square cross-section, and two additional variations from the baseline were investigated for each parameter. The naming convention starts with the shape and diameter of the heat-set mandrel (S25: straight 25 mm Ø), then combined with a letter and the value representing the parameter modified.

2.4.3. Nitinol Wire Stent Winding

Various stent winding methods were investigated, along with Nitinol wires of different Af temperatures (body temperature 37℃, room temperature 25℃, "super-elastic" <0℃, and "shape-memory" >60℃).

Steel binding wires (<1 mm Ø) were wrapped around the heat-set mandrel between the two rows of wrapping posts to prevent the Nitinol wire from unwrapping, the Nitinol wire was threaded through, and bent tightly around each winding post until the sinusoidal pattern was completed. The ends of the Nitinol wire were then crimped together using a short length (5-10 mm) of hypotube or spring-pin. An example of the wound Nitinol wire on the heat-set mandrel is shown in Figure 2-19.

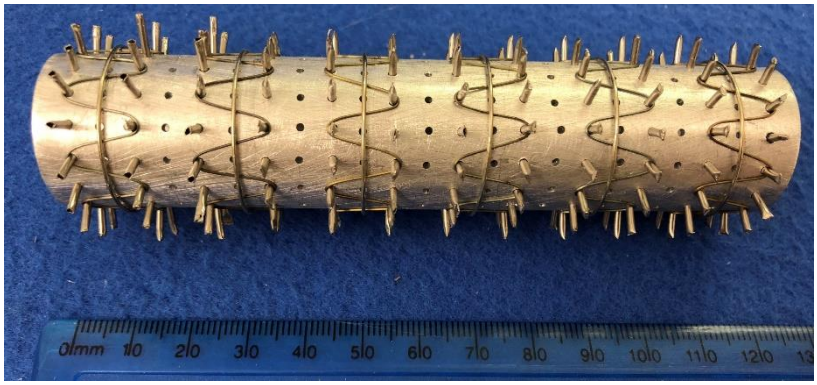

Figure 2-19 Nitinol wire wound on the heat-set mandrel

2.4.4. Nitinol Stent Heat-Setting

Heat-setting of the Nitinol stent was done using a Techne SBL-2D fluidised bath (TC-9D temperature controller), which evenly heated the stent.

The fluidised bath was gradually heated, and the supplied airflow was adjusted accordingly as shown in Table 2-3, until 500℃ was reached, the wound heat-set mandrel was then fully submerged into the fluid bath, heat-set for exactly 5 minutes, taken out, and then quickly quenched in cold water. The steel binding wires were disposed; the stent rings were then stretched, and carefully removed.

Table 2-3 Airflow settings for various temperatures in the fluidised bath

Temperature (℃)	Airflow (SCFM)
50	3.0
100	2.6
200	2.5
300	2.0
400	1.7
500	1.5
600	1.4

2.4.5. Nitinol Transformation Temperature Determination

The transformation temperature of Nitinol wires were determined using a Perkin Elmer DSC4000 differential scanning calorimeter (DSC).

To start the DSC test, the chiller was set to -80°C, the Argon gas supply valve was opened, the DSC was switched on, followed by starting the Pyris software. Before performing tests on the Nitinol samples, the DSC was calibrated using Indium standards (10°C/min). For the tests of Nitinol, wire samples (approximately 30 mg) of various diameters (250, 380, 500 µm) before and after heat-set were weighed (Mettler Toledo XS105 scale (d = 0.01 mg/0.1 mg)), placed in 50 µl DSC pans, and lids were then crimped on. The sample and reference (empty 50 µl pan with crimped lid) pans were placed in the DSC, the weight of the sample was entered on Pyris, and the test was setup to perform a heating and cooling cycle (between -40°C and 100°C at 10°C/min) as shown in Figure 2-20.

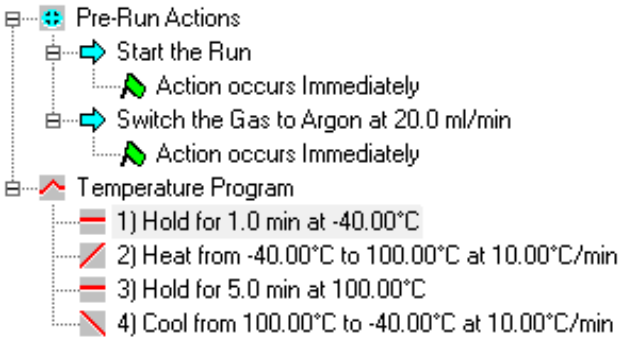

Figure 2-20 Nitinol DSC test setup

Once the test was completed, the "Peak Area" and "Onset" values were calculated on the generated graph. These values were calculated separately for the heating and cooling curves, which gave the As, Ap, and Af temperatures for the former, and Ms, Mp, and Mf temperatures for the latter. An example of the generated graph and corresponding positions for each temperature is shown in Figure 2-21.

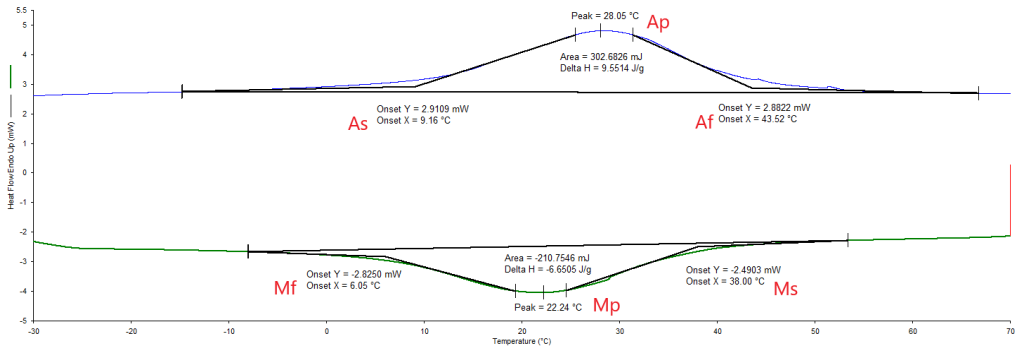

Figure 2-21 Corresponding positions of the various Austenitic and Martensitic temperatures on the DSC curve

2.4.6. Patient-Specific Heat-Set Mandrel Concept

A heat-set mandrel design was made for a patient-specific case, where the designed stent-graft geometry (10% oversize, STL file) was imported into SolidWorks and 1 mm Ø pins were manually placed and extruded 2 mm from the surface of the model, following a sinusoidal pattern with stent heights between 5-15 mm (see Figure 2-22). The concept was to 3D print this mandrel in metal (such as stainless steel, titanium or aluminium), wrap and heat-set the stent on the patient-specific shape, which will conform even better to their anatomy. The concept was not completed but is recommended to be further pursued when resources allow it.

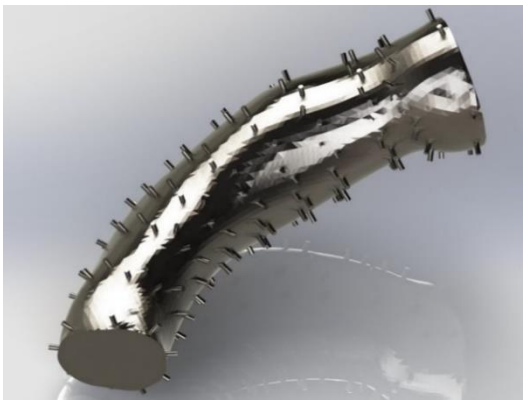

Figure 2-22 Patient-specific heat-set mandrel design in SolidWorks

2.5. Stent Incorporation

Traditionally, the stents are hand stitched onto the graft scaffold, which is a very time consuming process. However, with the use of electrospinning, the stent was attached to the graft much quicker, and the amount of manual labour decreased.

The P16, 10% oversized design was 3D printed, electrospun with the luminal layer, incorporated with stent rings by overspinning the abluminal layer, the ends were trimmed, and the stent-graft was removed from the mandrel with the aid of Ballistol Teflon spray.

The first luminal layer was electrospun using the methods described. The heat-set stent rings were pre-cooled in a freezer (30 minutes), crimped as small as possible in ice water (to reduce the temperature below its Mf temperature), and stretched snugly over the luminal layer on the mandrel (Figure 2-23a). Once all stent rings were in place, arranged accordingly, and allowed to dry (5 minutes), the abluminal layer was overspun, creating the stent-graft (Figure 2-23b).

a)
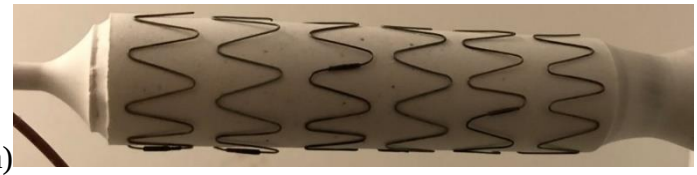

b)
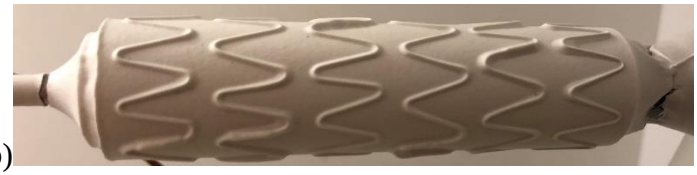

Figure 2-23 a) stent rings placed over luminal layer, b) abluminal layer overspun, incorporating the stent rings

With the stent incorporated into the graft scaffold, the electrospun stent-graft could no longer be rolled off the mandrel; a thin metal rod (<1 mm Ø) was rolled between the scaffold and the mandrel, Ballistol Teflon spray was then sprayed between, and the stent-graft was then gently manoeuvred off the mandrel

2.5.1. Radial Force Testing

The radial force (RF) of the stent/stent-graft was determined using a MSI RX650 radial force tester (see Figure 2-24). The initial (1-2 mm larger than the measured diameter) and final (half of the initial diameter) diameters were set on the computer program, the diameter on the machine was adjusted to the initial diameter, the sample was placed gently inside the radial force tester, and the test was performed at a rate of 0.5 mm/s for three loading and unloading cycles, at a temperature close to body temperature (36-38°C). The data was then analysed in Microsoft Excel, with the intended heat-set diameter as the starting point for calculating the radial force at 10 and 20% diameter reductions to simulate oversizing (OS) effects.

a)
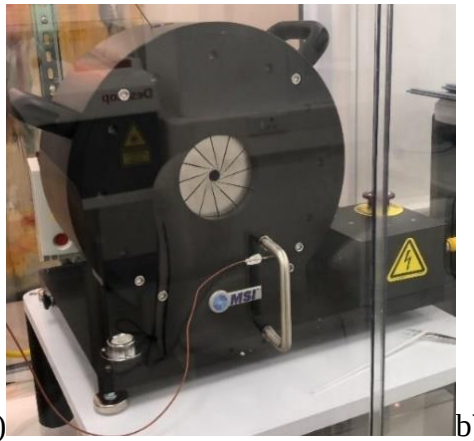

b)
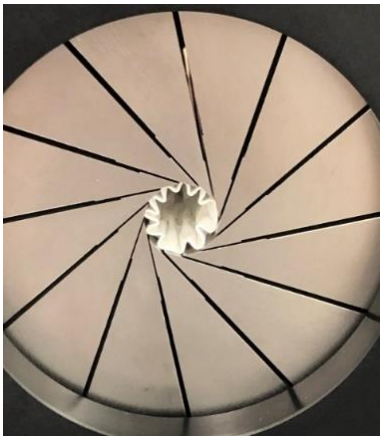

Figure 2-24 a) MSI RX650 radial force tester, b) electrospun stent-graft sample crimped in the radial force tester

Radial force tests were performed on electrospun stent-grafts using the stent patterns shown in Table 2-2, the patient-specific P16 stent-graft, as well as on commercial stent-grafts, the

individual stent rings were then removed from various graft scaffolds and individually tested. Due to the curvature of the P16 stent-graft, side A and B were tested separately (3 stent rings each), their averages were combined, and denoted as PS-P16 SG. The expanded diameter (diameter at 0.2 N RF) of the stent rings were measured by the radial force tester.

The commercial devices investigated were Cook Medical Zenith Flex TFFB-30-96-ZT (stainless steel stent) and Medtronic Endurant II ETBF-32-16-145 (Nitinol stent) stent-grafts.

2.5.2. Delamination Resistance Determination

When the stent was incorporated, irregularities of the stent profile caused visible air pockets between the luminal and abluminal layers. A delamination test was thus performed to test the mean delamination force required to cause the graft layers to delaminate, as well as to investigate if the incorporation of the stent had an effect on the delamination force.

The delamination force between the electrospun scaffold layers were tested by, force-delaminating 5 mm width samples, leaving at least 3 mm of un-delaminated scaffold, each split end was clamped in the Instron and uniaxial extension was performed at 5 mm/min until fully delaminated. Five samples from each of two electrospun grafts were tested; one plain electrospun scaffold and one stent-incorporated scaffold (12 wave, 10 mm stent height, 380 μm Ø wire). An example of the test sample is shown in Figure 2-25.

Figure 2-25 A force-delaminated electrospun graft scaffold sample

2.6. FEA Simulation

Computer simulations were done in collaboration with Technische Universität München using their own in-house simulation software (Hemmler, Lutz, Reeps, Kalender, & Gee, 2018b) on the electrospun and commercial stent-grafts, the radial force results were validated using the experimental radial force test results. The simulation results may act as a guideline for stent design optimisations in the future. Simulation was also performed to compare a cylindrical and curved stent-graft on a simplified, curved aortic anatomy to show differences in the conformity, areas with better seal, and stress distribution on the stent-grafts.

2.6.1. Poisson's Ratio Determination

The Poisson's ratios of the graft materials were required to simulate the behaviour of the stent-grafts more accurately. Dogbone samples (5 x 28 mm) were cut at the desired orientations (longitudinal and circumferential) and a straight line was marked in the middle across the width of the sample. Uniaxial extensions were performed manually on the Instron in 0.5 mm increments, until a 3 mm extension was reached. A photo of the sample was taken at each increment (iPhone 8 cell phone camera, mounted on a test tube stand) at the exact same position and zoom level, examples at 0 and 3 mm extensions are shown in Figure 2-26. The photos were processed in Fiji (Image J); the transverse contraction due to the longitudinal extension was measured and recorded, and used to calculate the Poisson's ratio.

a) 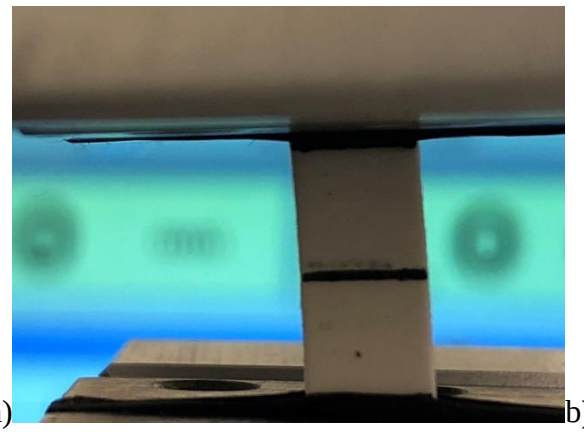 b) 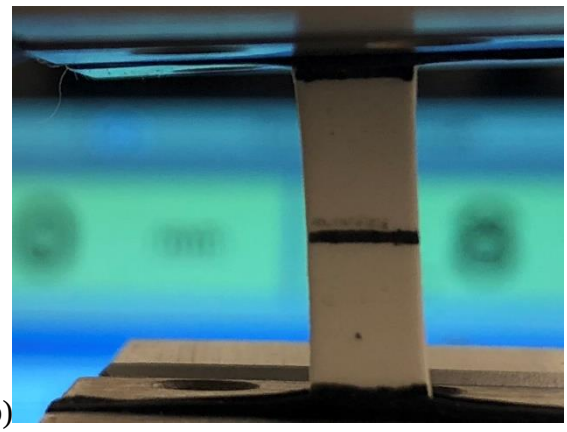

Figure 2-26 Electrospun scaffold Poisson's ratio test, a) 0 mm extension, b) 3 mm extension

Poisson's ratio formula:

$$\nu = -\frac{\varepsilon_2}{\varepsilon_1}$$

ε_1: Longitudinal strain (strain in the direction of load)

ε_2: Transverse strain (strain perpendicular to the direction of load)

2.7. Mock Insertion

Hollow aortic models were used for mock insertion to test fit the patient-specific stent-grafts; they should preferably be transparent enough to show the deployed stent-graft clearly, and flexible enough to mimic the mechanics of the aorta.

Mock insertion was investigated in the P16 hollow aortic model 3D printed using transparent PLA filament, see Figure 2-27. The P16 stent-graft was crimped, and the distal end was clamped between a crocodile clip with a piece of wire attached. A hole was made in the aortic model just below the distal landing zone; the wire was threaded through the proximal end of

the aortic model, pulled through the hole, the stent-graft was guided and pulled to the correct location, the orientation was adjusted from the proximal end, and the stent-graft was expanded by heating.

Figure 2-27 3D printed P16 transparent PLA aortic model

2.8. Statistical Analysis

One way analysis of variance (ANOVA) and post hoc Student's t-tests were performed in Microsoft Excel to determine the statistical significance of the difference between the results; the difference was considered significant when $P<0.05$. All data are shown as mean±standard deviation, unless stated otherwise.

3. Results and Discussion

This section summarises the results and discussion for the development of the patient-specific stent-graft using electrospinning. The subsections include studies of the patient-specific stent-graft geometry design, the electrospinning mandrel materials, the effect of selected electrospinning parameters on the electrospun graft scaffold, the effect of the mandrel shapes on the morphology of the electrospun graft scaffold, the Nitinol transformation temperature of the different diameter wires, the parametric effect of stent pattern designs on the generated radial force, the simulation and experimental result comparison, and the mock insertion results.

3.1. Patient-Specific Models

3.1.1. Stent-Graft Geometry Design

The patient-specific AAA stent-graft design generated in Mimics conserved the native blood vessel geometry very well, as shown in Figure 3-1b; although the TAA stent-graft geometry designed in SolidWorks, shown in Figure 3-1a, was not as precise, the curvature may still improve the conformity compared to standard devices.

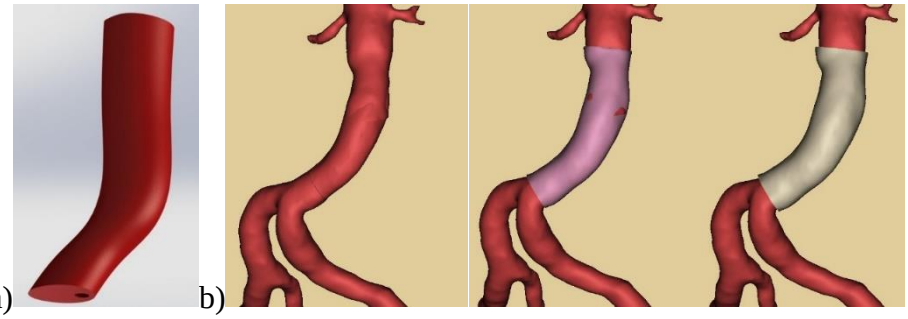

a) b)

Figure 3-1 a) TAA stent-graft geometry design, b) AAA stent-graft geometry designs (0, 10, 20% oversize)

3.2. Electrospinning Mandrel

Both of the TAA and AAA (P16) patient-specific graft geometries investigated were successfully 3D printed, as shown in Figure 3-2.

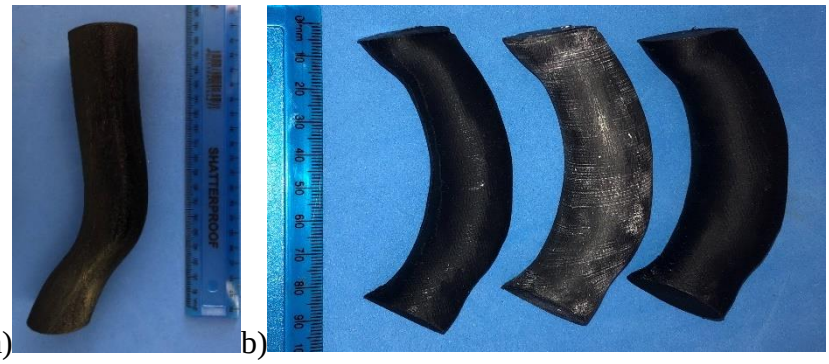

a) b)

Figure 3-2 Patient-specific graft geometry electrospinning mandrels, a) TAA geometry, b) P16 AAA geometry, 0, 10 and 20% oversize designs, 3D printed with conductive PLA

However, this specific TAA geometry (Figure 3-2a) does not suit the TEVAR procedure, and the mandrel was too big for the current electrospinning rig, thus, further investigations were not performed on this specific geometry.

The P16 AAA geometry (Figure 3-2b) was suitable for the EVAR procedure, and the designed electrospinning mandrel geometry could be electrospun on the current electrospinning rig. However, due to the curvature of the mandrel, a through hole was not possible, thus a 5 mm hole (approximately 30 mm deep) was drilled on one side for the attachment of the metal rod.

3.2.1. 3D Printer Modifications

The surface improvements of the 3D printed mandrel after the additional printer upgrades are shown in Figure 3-3b, where the surface became smoother with less defects compared to the 3D print before these upgrades, as shown in Figure 3-3a.

a)  b) 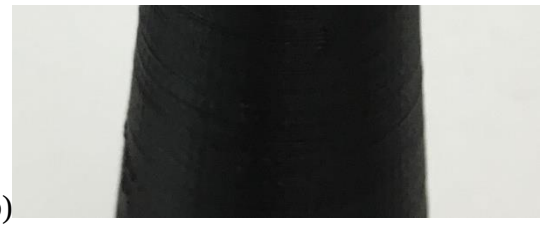

Figure 3-3 Surfaces and print quality of 3D printed mandrels, a) before 3D printer upgrades, b) after 3D printer upgrades

The surface quality of the 3D printed mandrels may have improved due to the part being cooled quickly, as well as the improved rigidity and reduced vibration from the aluminium frame.

3.2.2. Electrospinning Mandrel Material

The electrospun scaffold on the two tapered mandrels was thinner for the non-conductive mandrel compared to the conductive mandrel (0.08±0.01 mm vs 0.18±0.01 mm at the larger end), the former also collapsed after it was removed from the mandrel, whereas the scaffold from the latter held its shape after removal, as shown in Figure 3-4.

a) 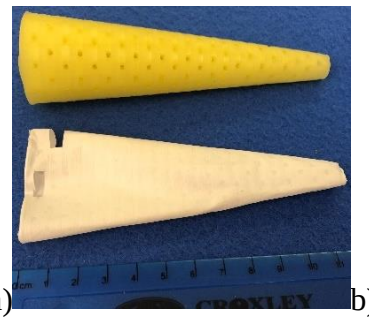 b) 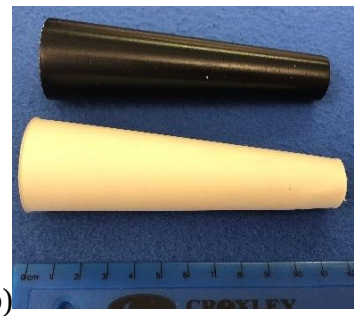

Figure 3-4 Electrospun scaffolds using, a) non-conductive (2 mm perimeter holes), and b) conductive PLA tapered mandrels

The difference in thickness between the electrospun scaffolds shows that the non-conductive PLA electrospinning mandrel had poorer attraction of the electrospun fibres compared to the conductive mandrel, even with the addition of perimeter holes.

The surface of the scaffold on the non-conductive mandrel reflected irregularities such as layer lines and the perimeter holes, whereas it was smooth for the conductive mandrel scaffold, as seen in Figure 3-5; since the inner surface of the scaffold should be as smooth as possible to decrease the friction on the blood flow, these irregularities are not ideal.

a)  b) 

Figure 3-5 Surfaces of electrospun scaffolds from, a) non-conductive (2 mm perimeter holes), and, b) conductive PLA mandrels.

An extreme case with minimal fibre deposition was seen on a non-conductive mandrel with 1 mm perimeter holes, where there were more fibre deposits on the metal rod than on the mandrel, and the fibres on the mandrel seemed to have followed the electric field around it, (Figure 3-6).

Figure 3-6 Minimal electrospun fibres around non-conductive PLA mandrel (1 mm perimeter holes)

The minimal deposition of fibres might also be caused by the mandrel being non-conductive, static electricity build-up (possibly from drilling), or the perimeter holes being too small thus was not able to sufficiently improve fibre attraction.

Since fibre deposition improved on conductive PLA mandrels without the need of perimeter holes, the mandrel surface could thus be improved as described in Section 3.2.3.

3.2.3. Surface Smoothing

The surface finish of the untreated mandrel showed clear layer lines and prominent surface irregularities, whereas on the treated mandrel the surface was smooth with less visible layer lines, as seen in Figure 3-7a and Figure 3-7b respectively. Excessive vapour smoothing caused a tapered mandrel to break into three segments, as seen in Figure 3-7c.

a) 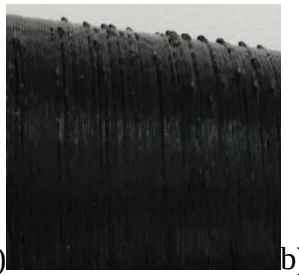 b)  c) 

Figure 3-7 a) untreated surface of 3D print (0.1 mm layer height), b) treated surface of 3D print (sanded & vapour smoothed), c) broken mandrel due to excessive vapour smoothing

Sanding removed most of the layer lines on the 3D printed mandrel, which smoothed the surface; although some of the mandrel surface was removed, (≈1 mm or ≈4% for a 25 mm Ø mandrel), the decrease in diameter was negligible. However, to counteract the loss of diameter, one can also 3D print the mandrel 1 mm larger and sand it to the correct size after printing. THF vapour smoothing created a smooth, glossy layer around the surface of the PLA mandrel, thus further improving the surface finish.

In Figure 3-7c, the excess vapour may have dissolved the bond between the layers, or the heat may have caused the layers to expand and separate, and eventually causing the mandrel to break.

3.3. Electrospun Graft Scaffold

3.3.1. Environmental Control System

In Figure 3-8, the environmental control system was able to increase the RH from 40% to 60% in approximately 5 minutes, decrease from 70% to 45% within 20 minutes, as well as stabilise at ±1-2% around these set points. In Figure 3-9, the system raised the RH from 33 to 56.8% in 30 minutes.

The ability to control the RH within the enclosure was dependent on the ambient RH as seen in Figure 3-8 and Figure 3-9; when the ambient RH was high (54.8%), it took longer to lower the RH (≈15 min , 70 to 45%) than the time it took to raise it (≈8 min , 45 to 70%); similarly, when the ambient RH was low (33%), the system was only able to raise the RH to 56.8% after 30 minutes.

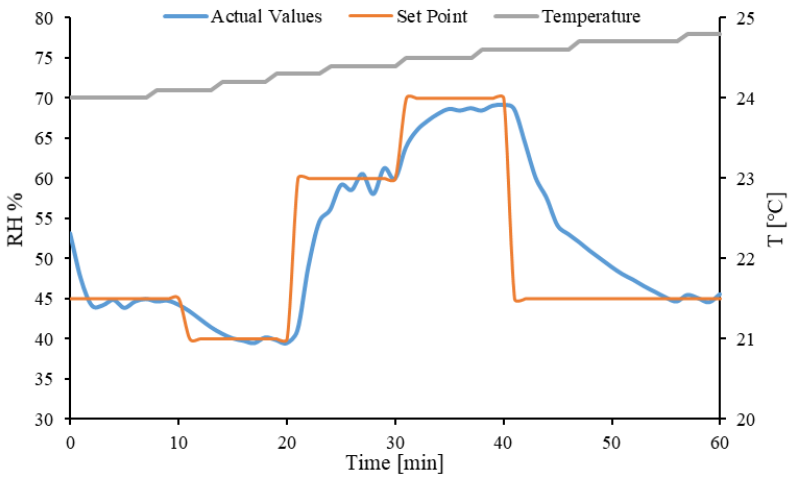

Figure 3-8 Environmental control system efficiency test result, ambient conditions at 54.8% RH, 23.3℃

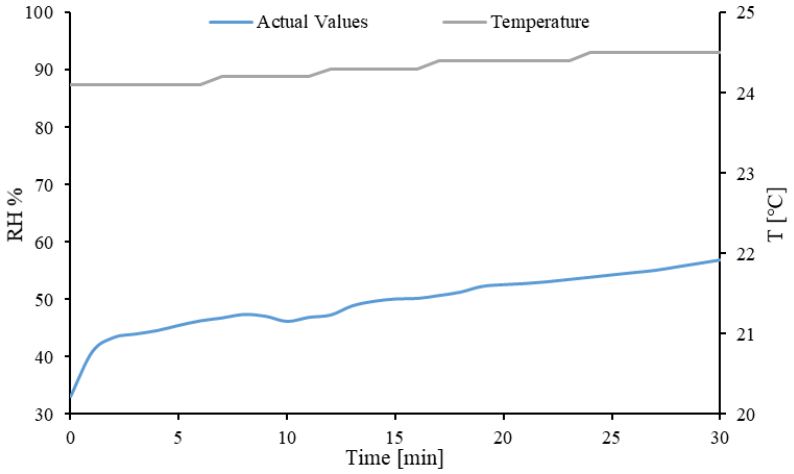

Figure 3-9 Environmental control system efficiency test result, ambient conditions at 33% RH, 23.6℃

3.3.2. Electrospinning Parameters

3.3.2.1. Mandrel to needle distance

The mandrel electrospun at a distance of 260 mm had wet/fused fibre deposition in the centre (Figure 3-10a), whereas at 300 mm there was uniform fibre deposition (Figure 3-10b).

a)

b)

Figure 3-10 Electrospun scaffolds showing, a) wet/fused fibre deposition in the centre (260 mm, +15 kV, -3 kV, 5 ml/hr, 1 mm/s), b) uniform fibre deposition (300 mm, +15 kV, -3 kV, 5 ml/hr, 1 mm/s)

Wet deposition of fibres may be the result of the electrospinning mandrel being too close to the needle, since uniform fibre deposition occurred when the distance was increased.

3.3.2.2. High voltage supply

Fused droplets were formed on the surface when electrospun at +13 kV (Figure 3-11a), whereas at +18 kV there was uniform fibre deposition (Figure 3-11b).

a)  b) 

Figure 3-11 a) fused droplets of polymer solution on electrospun scaffold (+13 kV, -3 kV), b) uniform deposition of fibres on electrospun scaffold (+18 kV, -3 kV)

The fused droplets may be the result of the voltage difference being too low, since uniform fibre deposition occurred when the voltage difference was increased.

The electrospinning parameters showed interconnected effects on the electrospun fibres. For example, when the flow rate of the polymer solution was increased, the mandrel to needle distance, and/or the voltage difference between the needle and collector mandrel may need to be increased as well, otherwise it may result in wet landing of the fibres, and create a fused scaffold similar to those shown in Figure 3-10a.

3.3.3. Graft Scaffold Thickness

Electrospun Pellethane graft scaffolds with full coverage of fibres along the whole 3D printed conductive PLA mandrel were possible with all 15 idealised geometry mandrels, see Figure 3-12. The microscopic fibre distributions will be discussed in Section 3.3.5.

Figure 3-12 Electrospun graft scaffolds on 15 idealised geometry 3D printed conductive PLA mandrels

S25 scaffold at position 2 (0.36±0.015 mm) was significantly thicker compared to positions 1 (0.29±0.01 mm) and 3 (0.3±0.03 mm), which had similar thicknesses, see Figure 3-13a; this might be due to the needle translating past the centre for a longer time than at the ends.

As shown in Figure 3-13b, the thickness for tapered mandrels were generally significantly thicker at positions 1 (mean 29.54% higher) and 2 (mean 43.63% higher) compared to position 3, except for T30 which had similar thicknesses across all three positions (mean 0.27±0.02 mm). T10 had similar thicknesses between positions 1 and 2 (mean 0.32±0.02 mm).

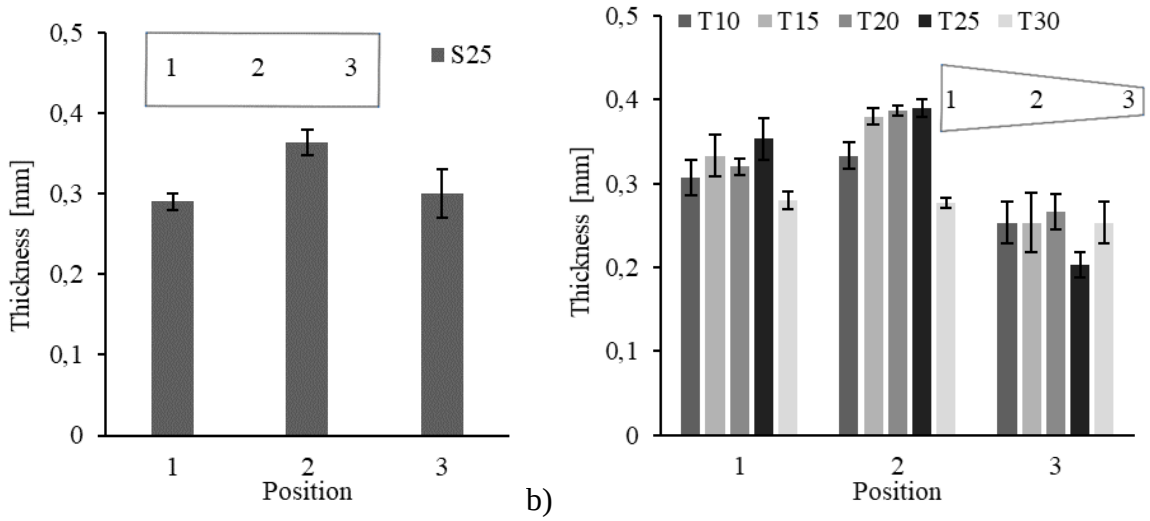

Figure 3-13 Electrospun Pellethane graft thickness variations at different positions on, a) straight mandrel, b) tapered mandrels

On the tapered mandrels, although the scaffold near the smaller end has a smaller surface area which should have a thicker coverage per pass of the needle, it was shown that the scaffold near the larger end was generally thicker than the smaller end. This may be due to the larger end being closer to the needle, thus having a stronger attraction force on the fibres; when the diameter at the smaller end was increased to almost the same diameter as the larger end (T30, 30x35 mm), this effect was negated, where the thickness across all three positions became similar.

The thicker end of the taper may have negated the effect of the centre being thicker due to the needle passing the centre of the mandrel more often, since the centre is now further from the needle compared to the larger end, as shown by the similar thicknesses between positions 1 and 2 in T10. However, this effect still stands for all tapered mandrels when comparing positions 2 and 3, except in T30.

Figure 3-14 showed the scaffold at position 4 was significantly thicker compared to positions 1 to 3 and 6 for all four curved mandrels, except for C05 where positions 4 and 6 were similar;

position 1 was also generally thicker compared to position 3, except for C10 where they were similar, and C20 where it was lower. This may be due to the curvature, where positions 1 and 4 are closer to the needle compared to positions 3 and 6.

C05 had similar thicknesses at positions 4, 5, and 6 (mean 0.45±0.02 mm), and significantly thicker at position 1 (0.38±0.02 mm) compared to positions 2 and 3, which were similar (mean 0.32±0.01 mm). C20 was thickest at position 4 (0.42±0.015 mm), and thinnest at position 1 (0.26±0.031 mm), with a 62.33% difference; this may be due to position 1 being further away from the needle, as well as being on the end.

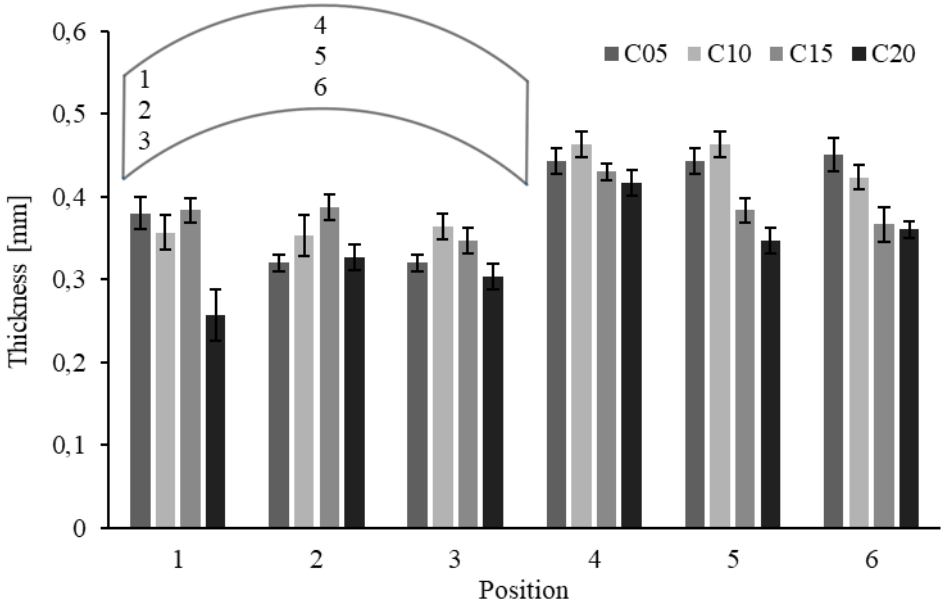

Figure 3-14 Electrospun Pellethane graft thickness variations at different positions on curved mandrels

On the curved mandrels, the scaffolds were generally thickest at position 4, which may be due to it being the peak of the curvature, thus being closer to the needle, as well as being in the centre of the mandrel.

In the elliptical mandrels, a significant trend was seen in the change in thickness at the different positions with the variation of the geometry, as shown in Figure 3-15; the thicknesses decreased at positions 1 and 3, and increased at positions 2 and 4, with the increase in the width of the ellipse. The scaffolds were thicker near positions 1 and 3 compared to positions 2 and 4 at larger length to width ratios (E10 and E15), and the thickness difference decreased as the ratio became smaller, as seen where the thicknesses at positions 1, 3 and 4 (mean 0.42±0.02 mm) became similar for E30. In E10 and E15, position 3 was more than double the thickness of position 4.

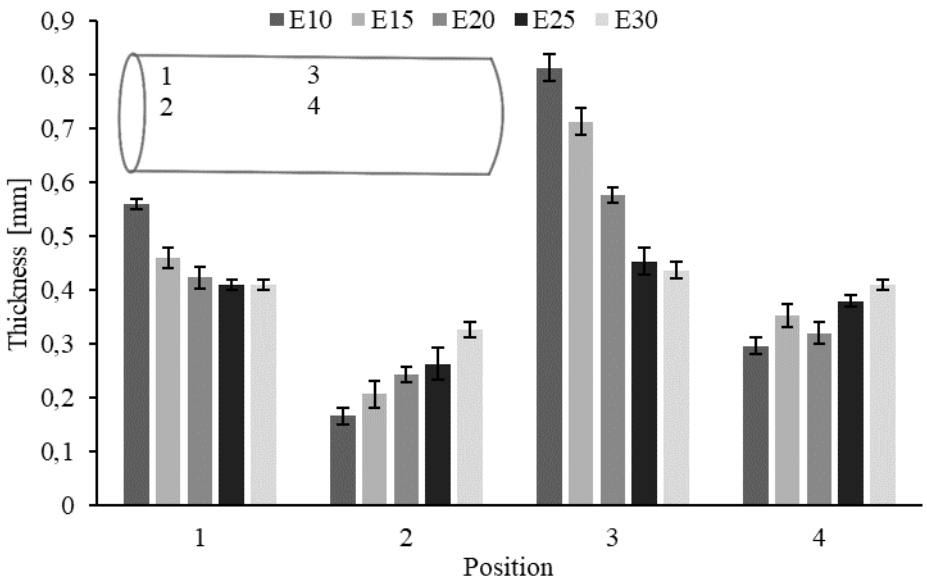

Figure 3-15 Electrospun Pellethane graft thickness variations at different positions on elliptical mandrels

A Pellethane graft scaffold was also successfully electrospun on the P16 graft geometry, with full coverage of fibres along the whole mandrel, as shown in Figure 3-16.

Figure 3-16 Electrospun Pellethane graft scaffold, on patient-specific P16 graft geometry

The thickness at position 4 (0.23±0.02 mm) of the P16 scaffold was significantly higher than positions 1 (0.17±0.03 mm) and 7 (0.13±0.01 mm), see Figure 3-17. On the one end, positions 1 to 3 had similar thicknesses (mean 0.16±0.02 mm), however, on the other end, position 7 (0.13±0.01 mm) was significantly thinner than positions 8 (0.25±0.03 mm) and 9 (0.22±0.01 mm). Positions 1 to 3 having different thickness variation trends compared to positions 7 to 9 may be due to the complex geometry, or due to the mandrel being mounted on one side only, thus having an uneven electrical field. Position 8 being thicker than position 4 may mean it was closer to the needle during the electrospinning process due to the way it was mounted, or maybe it had a stronger electrical field.

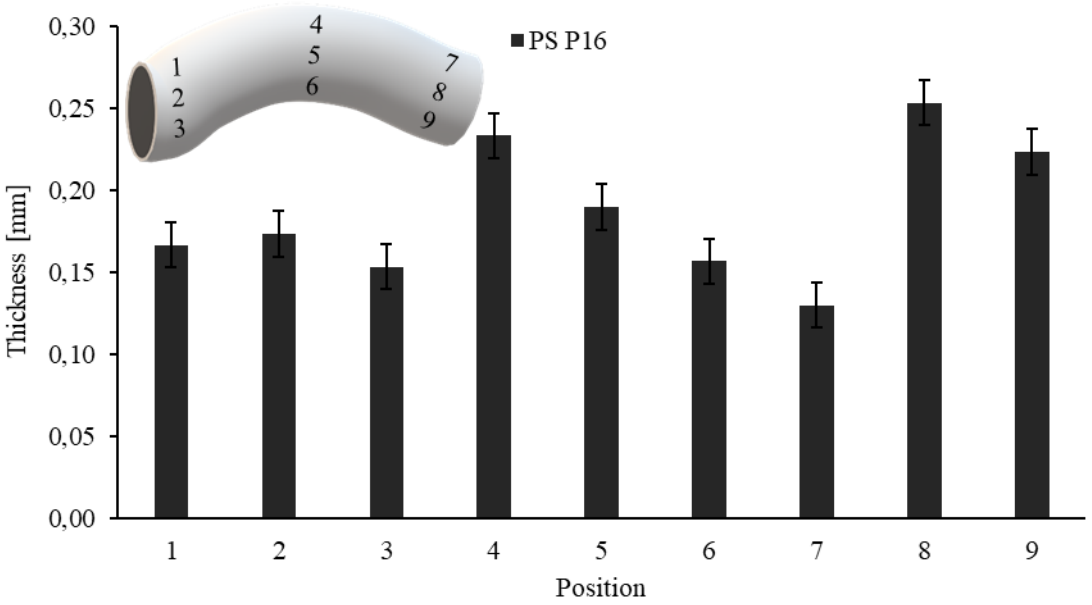

Figure 3-17 Thickness variations on the P16 electrospun Pellethane graft

3.3.3.1. Summary

Macroscopically, the electrospun graft scaffold on all 15 of the idealised geometry mandrels showed uniform fibre deposition, although the scaffolds were generally thicker near the centre of the mandrel compared to the ends of the mandrel.

Tapered mandrel scaffolds were generally thicker on the larger end compared to the smaller end, where the difference becomes smaller as the diameters become similar.

Curved mandrels show no additional trend, but when the curvature becomes too large, the ends near the convex side of the curve may become much thinner than the other positions.

Elliptical mandrel variations have a significant impact on the thickness variation between different positions; a significant trend was shown in the change in thickness due to the change in length to width ratios of the cross-section, where the thickness of the scaffold normalises as the cross-section becomes more circular. In general, the thickness at the peak on the major axis was significantly higher than the peak on the minor axis.

The P16 scaffold showed similar results in the thickness variation compared to curved mandrels, where the peak of the curve was thicker than the ends of the convex side. However, the complex geometry and the way it was mounted may have caused the unexpected result of position 8 at the end being thicker than the peak of the curve.

3.3.4. Tensile Testing

The Young's Modulus and UTS of the electrospun Pellethane graft scaffolds were 45% and 37% higher respectively in the longitudinal direction (2.15±0.47 MPa, 8.20±2.44 MPa) compared to the circumferential direction (1.48±0.43 MPa, 5.99±1.70 MPa), see Figure 3-18. The difference may be due to the alignment of the fibres, which was affected by the rotation speed. There was no significant difference between the maximum strain in the longitudinal (574±77%) or circumferential direction (566±71%). The mean Young's Modulus, UTS, and maximum strain of all the electrospun scaffolds were 1.87±0.56 MPa, 7.29±2.44 MPa, and 570.64±75.45% respectively.

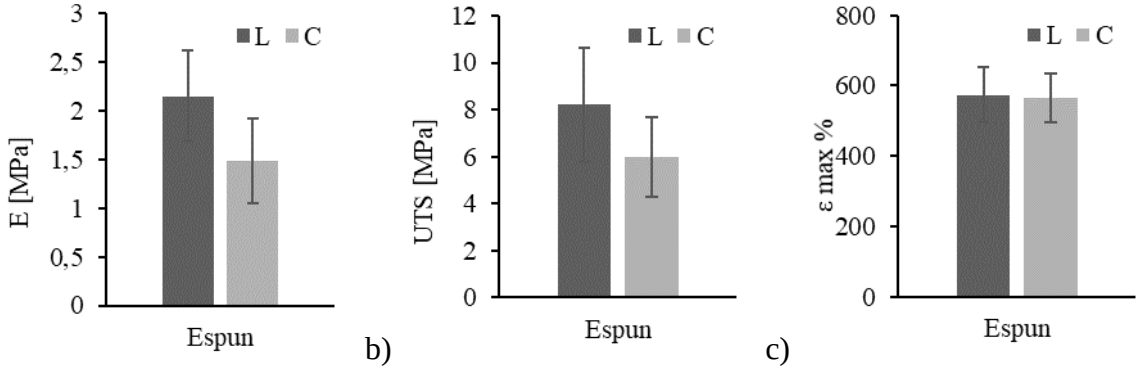

Figure 3-18 Electrospun Pellethane graft scaffold tensile test results showing, a) Young's Modulus, b) ultimate tensile strength, c) maximum strain

The mean UTS of electrospun scaffolds on tapered (8.44±3.71 MPa) mandrels was 52, 18, and 26% higher than the scaffolds on the straight (5.53±0.59 MPa), curved (7.15±1.56 MPa), and elliptical (6.67±1.35 MPa) mandrels respectively, see Figure 3-19. However, there was no statistical difference between the UTS of tapered and straight mandrels, but there was a statistical difference between tapered and elliptical mandrels, even though the mean UTS of elliptical mandrels were closer to that of the tapered mandrels. The scaffolds on curved and elliptical mandrels had similar mean UTS, but when compared with the straight or tapered scaffolds, one showed a statistical difference and the other did not. There was no clear indication as to why the UTS may differ in this way for the different mandrel shapes. Heat pressed Pellethane films had a significantly higher UTS (25.11±4.32 MPa), maximum strain (1213±84 %), and Young's Modulus (8.13±0.82 MPa) compared to the electrospun scaffolds (van den Bergh, 2018), which may be the result of fused vs fibrous scaffold structure.

There was no significant difference in the UTS of the scaffolds between the different positions, or between the different variations within each shape, on neither of the curved, elliptical, or tapered mandrels.

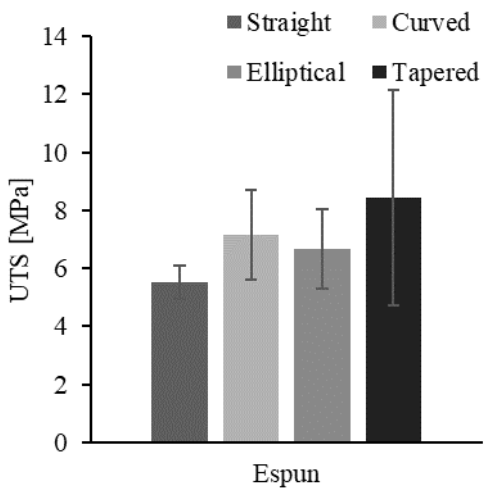

Figure 3-19 Mean ultimate tensile strength of electrospun Pellethane scaffolds on various mandrel geometries

3.3.4.1. Summary

The Young's Modulus and UTS were significantly higher in the longitudinal direction compared to the circumferential direction, but there was no significant difference between the maximum strains experienced in these two directions.

The shape of the mandrel might have no influence on the UTS of the electrospun scaffold, and may be more dependent on the material itself.

3.3.5. Fibre Morphology Evaluation

3.3.5.1. SEM imaging

Although the images taken with the Jeol JSM-5200 SEM were sufficient for analysis, the image quality was visually poor, thus, images for visual presentation purposes were retaken with the newer Nova NanoSEM, and the image quality was much improved, as seen in Figure 3-20a and Figure 3-20b respectively. The surface of the scaffold electrospun on the non-conductive PLA mandrel had prominent surface irregularities due to the holes on the mandrel as shown in Figure 3-20c.

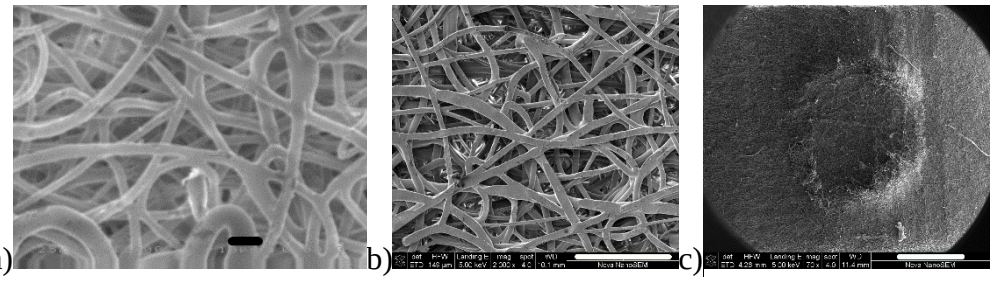

Figure 3-20 Electrospun fibre SEM image examples from, a) Jeol 5200 SEM, 25kV, 1000X magnification, scale bar 10 μm b) Nova NanoSEM230 SEM, 5kV, 2000X, , scale bar 50 μm c) electrospun scaffold on non-conductive PLA mandrel, 5 kV, 70X, , scale bar 1 mm

The SEM images in Figure 3-21 show uniform fibre deposition on the P16 graft geometry on both inside and outside surfaces. The inner surface fibres shown in Figure 3-22a seem to have a flatter profile compared to the outer surface fibres Figure 3-22c, this may be due to the fibres being slightly wet when landing on the flat surface of the electrospinning mandrel. Very fused inner surface fibres are shown in Figure 3-22b, which may be caused by a high RH, or the mandrel being too close to the needle. Figure 3-22d shows straighter fibres compared to the fibres in Figure 3-22c, which may be caused by a difference in rotation speed or electrospinning mandrel diameter; the surface speeds are higher for larger diameter mandrels compared to smaller diameter mandrels at the same rotation speed, which may have caused the fibres to be pulled on tighter during rotation, and caused the fibres to be straighter.

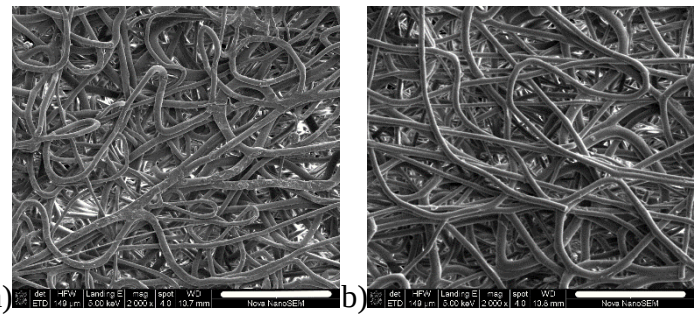

Figure 3-21 SEM images of electrospun fibres on the patient-specific P16 mandrel, a) inside, b) outside surface, 2000X magnification, scale bar 50 μm

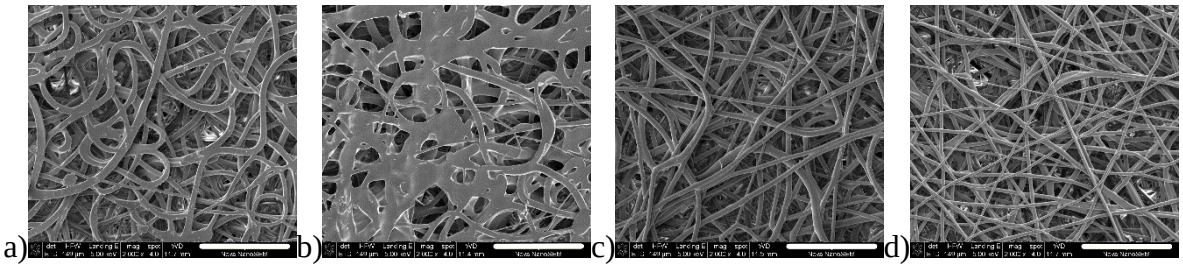

Figure 3-22 Typical SEM images of electrospun Pellethane fibres, a) inside surface, uniform fibres, b) inside surface, fused fibres b) outside surface, wavy fibres, c) outside surface, straight fibres, 2000X magnification, scale bar 50 μm

3.3.5.2. Coherency

Although the mean orientation index (*OI)* was significantly different between the various mandrel shapes, there was no clear trend in the way the *OI* differs between the various shapes, see Figure 3-23a; the mean *OI* was 0.35±0.15 for the electrospun scaffolds on all idealised geometry mandrels. Various scaffolds electrospun on different shapes also showed similar *OI*, except for T10 (0.50±0.14) and T15 (0.48±0.14), which were significantly higher than all the other samples (mean 0.34±0.15). The mean *OI* on the inner (0.36±0.15) and outer (0.34±0.15) surfaces of all the scaffolds also showed no significant difference (see Figure 3-23b).

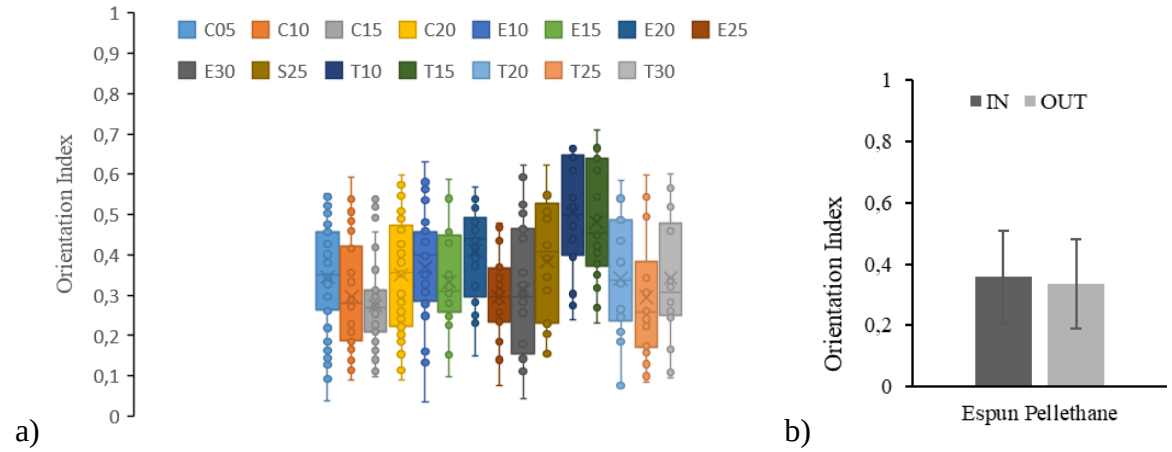

Figure 3-23 Orientation index of the electrospun Pellethane graft scaffolds, a) comparing scaffolds from each of the idealised geometry mandrels, b) comparing the inside and outside surfaces of the scaffolds

S25 position 1 (0.46±0.03) had significantly higher *OI* compared to position 2 (0.27±0.14), see Figure 3-24a, but the same could not be seen between the thickness of the scaffold at the ends and centres of the curved, elliptical or tapered mandrels, see Figure 3-24b to Figure 3-24d. Although there were significant differences between the *OI* at different positions for all mandrel shapes, there was no significant trend, (Figure 3-24b to Figure 3-24d).

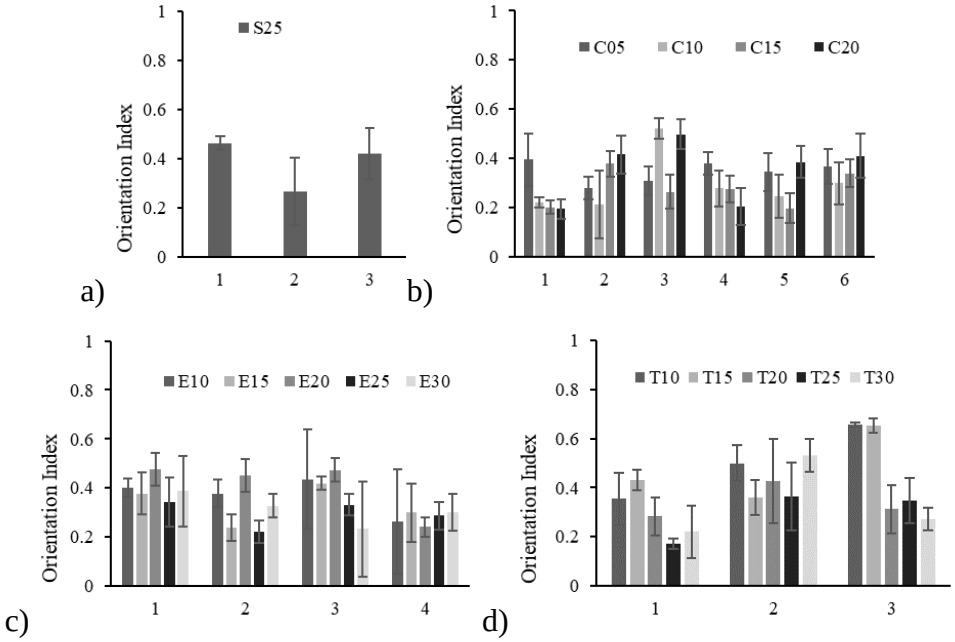

Figure 3-24 Orientation index of the electrospun Pellethane graft scaffolds, comparing different positions from a) straight 25 mm diameter mandrel, b) four variations of curved mandrels, c) five variations of elliptical mandrels, d) five variations of tapered mandrels

The mean *OI* of the scaffolds electrospun on all the idealised geometry mandrels show that the fibres were relatively random, but may still be more oriented in a certain direction ($0<OI<0.5$).

The electrospun P16 scaffold had a mean *OI* of 0.245±0.119 (Figure 3-25), which was significantly lower than the mean *OI* of scaffolds from the idealised geometry mandrels. This may be due to the P16 scaffolds being spun at a lower rotation speed. The variation in *OI* from positions 1 to 6 (Figure 3-23) showed a similar trend compared to C20, and may be due to the similar curvatures of the mandrels.

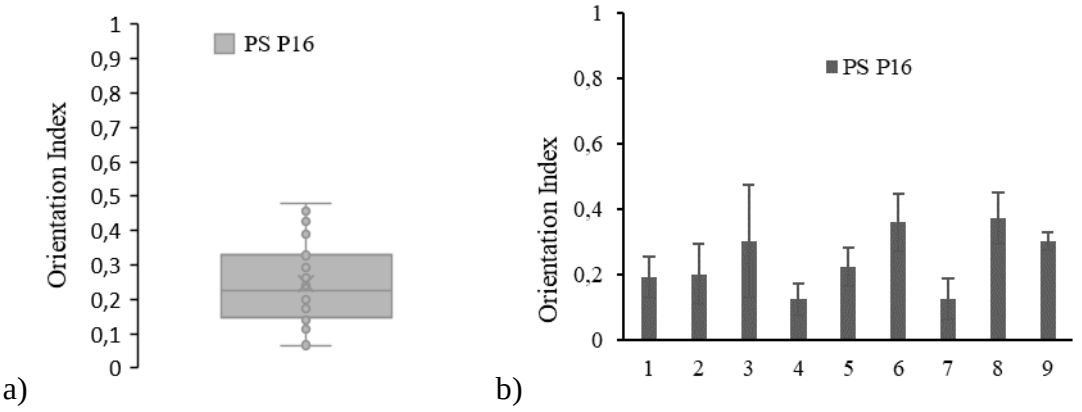

Figure 3-25 Orientation index of the patient-specific P16 electrospun Pellethane graft scaffold, a) distribution of OI, b) at different positions on the scaffold

3.3.5.2.1. Summary

The mandrel shape did not have a prominent effect on the variation in average coherency of the electrospun fibres.

The P16 scaffold electrospun at a lower rotation speed were more randomly oriented compared to the idealised geometry scaffolds electrospun at a higher speed, with a mean *OI* of approximately 0.25 and 0.35 respectively.

Although no significant trend was shown between the variation of the shapes and the different positions, the variation in the *OI* between the different positions of the P16 scaffold showed a similar trend compared to that on the C20 mandrel, which may be due to the similar prominent curved shape of the mandrels.

3.3.5.3. Fibre diameter

There was no significant difference between the mean fibre diameters for the scaffolds on the curved (2.39±0.30 μm), elliptical (2.33±0.43 μm), and tapered (2.32±0.32 μm) mandrels, which were significantly higher than the scaffold on the straight mandrel (1.90±0.14 μm), with a combined average of 2.33±0.36 μm between all idealised geometry scaffolds (Figure 3-26a). There was also no significant difference in fibre diameter for the inside and outside surfaces of the scaffolds (Figure 3-26b).

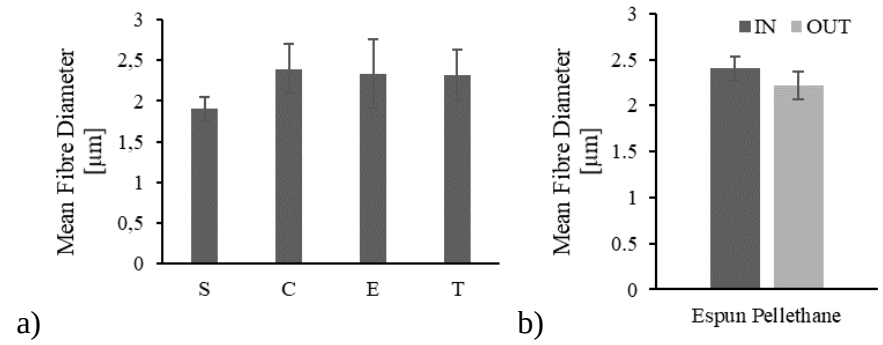

Figure 3-26 Mean fibre diameter of the electrospun Pellethane graft scaffolds, a) comparing scaffolds from each of the idealised geometry mandrels, b) comparing the inside and outside of the scaffolds

Although the mean fibre diameter of the scaffold at position 1 (1.80±0.13 µm) of the straight mandrel was statistically lower than position 3 (2.02±0.09 µm), as shown in Figure 3-27a, since the mandrel is cylindrical and symmetrical, there should not be variations in fibre diameter between these two positions. Thus, the variation had no clear relation to the geometry and may be due to other factors. Fibre diameters were also similar between positions 1 and 2.

The mean fibre diameters were generally similar between the variations of geometry for each of the curved, elliptical, and tapered mandrels, as well as between the different positions, see Figure 3-27; although E30 (2.88±0.24 µm) and T15 position 3 (2.96±0.21 µm) had significantly larger fibre diameters, there were no clear trend for these differences.

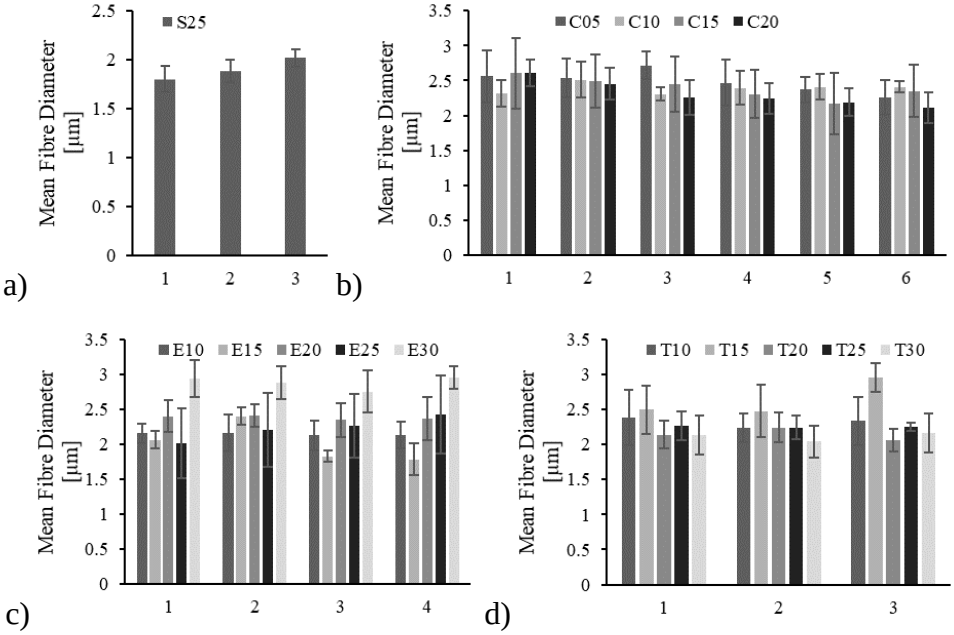

Figure 3-27 Mean fibre diameter of the electrospun Pellethane graft scaffolds, comparing different positions from a) straight 25 mm diameter mandrel, b) four variations of curved mandrels, c) five variations of elliptical mandrels, d) five variations of tapered mandrels

The mean fibre diameter of the P16 scaffold (2.10±0.52 µm) was statistically lower than that of the curved, elliptical and tapered scaffolds, but was similar to the scaffold on the straight

mandrel. There were larger fluctuations in fibre diameter (from 1.5 to 2.5 μm) between the different positions compared to the idealised geometry scaffolds, see Figure 3-28. The reason was uncertain, but it may be due to the complex geometry, different rotation speeds, or due to the mandrel being mounted on one side only, which may have caused higher vibrations or a less uniform electrical field.

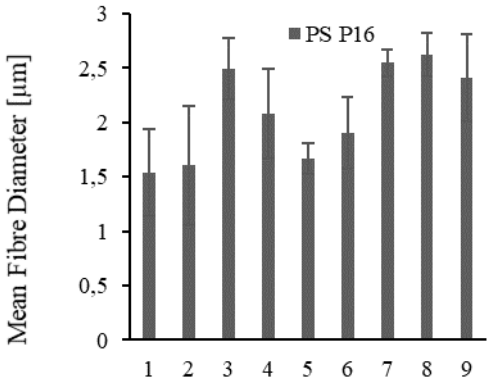

Figure 3-28 Mean fibre diameter at different positions on the patient-specific P16 electrospun Pellethane graft scaffold

3.3.5.3.1. Summary

The shape of the idealised geometry mandrels did not have a prominent effect on the fibre diameters of electrospun scaffolds, with a mean fibre diameter of approximately 2.3 μm.

The P16 scaffold had similar fibre diameters to the scaffold on the straight mandrel, with a mean fibre diameter of approximately 2.1 μm. Larger fluctuations of fibre diameters were seen on the P16 scaffold between various positions, but the reason was uncertain.

3.3.5.4. Pore size

There were no significant differences in mean pore diameters between the different curved mandrels. Although the difference in pore size across different elliptical and tapered mandrels were statistically significant between a few of the shape variations, there was no clear trend, and were approximately between 6 to 8 μm, as seen in Figure 3-29a. This means there might be no relation between the pore size and the mandrel geometry.

There was no significant difference in the mean pore diameter between the inside and outside surfaces of the electrospun Pellethane scaffolds, as shown in Figure 3-29b.

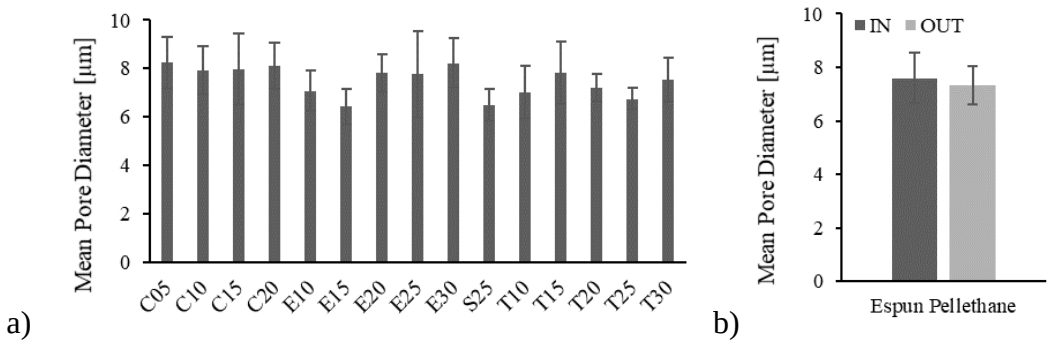

Figure 3-29 a) mean pore diameter of the electrospun Pellethane graft scaffolds, comparing scaffolds from each of the idealised geometry mandrels, b) mean pore diameter of the electrospun scaffolds comparing the inside and outside surfaces

There were no significant difference in pore diameter between the different positions on all idealised mandrel shapes, with a mean of 7.52±1.20 µm, see Figure 3-30.

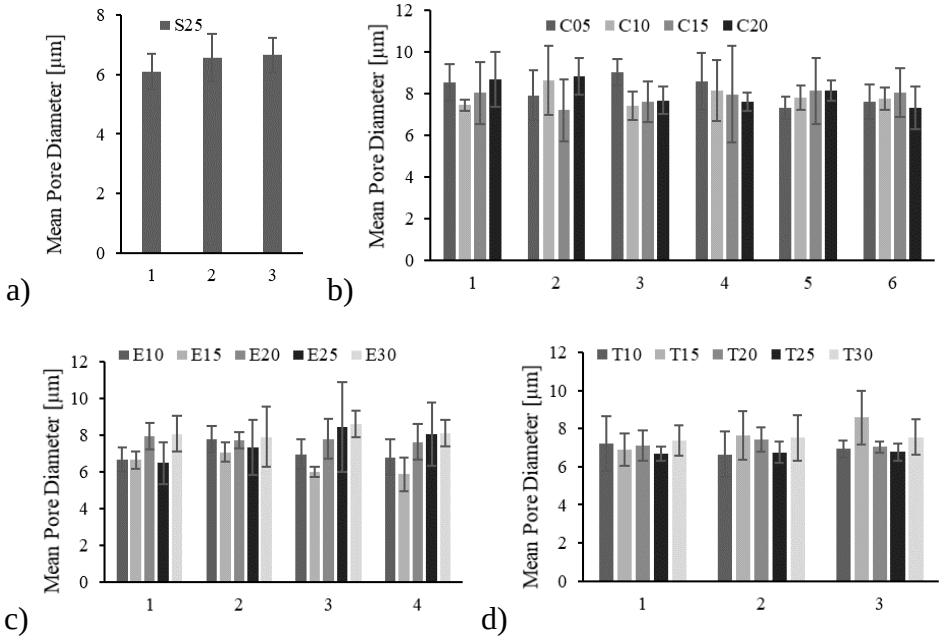

Figure 3-30 Mean pore diameter of the electrospun Pellethane graft scaffolds, comparing different positions from a) straight 25 mm diameter mandrel, b) four variations of curved mandrels, c) five variations of elliptical mandrels, d) five variations of tapered mandrels

Similarly, the mean pore diameter for the P16 scaffold (mean 8.54±1.46 µm) showed no significant difference between the nine different positions, as shown in Figure 3-31, but was statistically larger than the idealised geometry scaffolds.

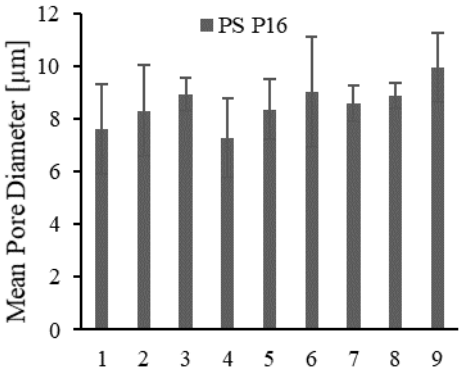

Figure 3-31 Mean pore diameter at different positions on the patient-specific P16 electrospun Pellethane graft scaffold

The mean pore diameter of the Pellethane graft scaffolds electrospun on the idealised geometry mandrels as well as the P16 graft geometry were larger than 5 μm, which was previously shown to allow endothelialisation, although a larger pore diameter near 30 μm was shown to have even better results for rapid tissue ingrowth (Z. Zhang, Wang, Liu, & Kodama, 2004).

3.3.5.4.1. Summary

The shapes of the idealised geometry mandrels did not have a prominent effect on the pore diameters of electrospun scaffolds, with a mean pore diameter of approximately 7.5 μm.

The P16 scaffold had statistically larger pore diameters compared to the idealised geometry scaffolds, with a mean of approximately 8.5 μm.

The mean pore diameters of the electrospun scaffolds on the idealised geometry mandrels as well as the P16 mandrel were all large enough for endothelialisation.

3.3.6. Branched Mandrels

Fibres were unable to deposit near the base of the 90° branch or under the 45° branch, forming "tent"-like structures, as shown in Figure 3-32. This may be due to the rotation speed being too high, the branch obstructing the fibres from the mandrel, or due to the shape of the electrical field around the mandrel; the electrospun fibres also follow a forward and outward helical flight path (Reneker & Yarin, 2008), which may also play a role in the "tenting" effect. When the rotation speed was lowered to 120 rpm, the motor was unable to rotate smoothly at such a low speed; although fibres deposited on the unobstructed side of the branch, there was still no fibre deposition under the 45° branch, as shown in Figure 3-32b. This means that electrospinning of branched scaffolds may only be possible on the current electrospinning equipment with a few modifications.

a) 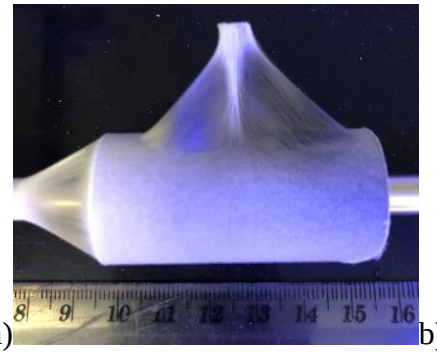 b) 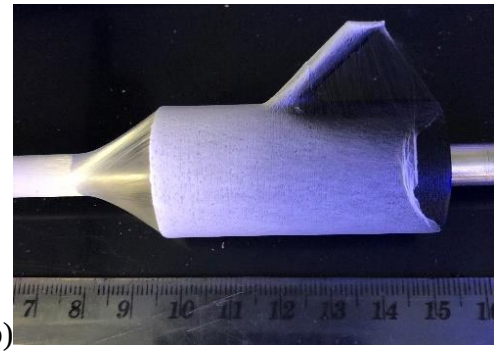

Figure 3-32 Electrospun scaffolds on a) 90° b) 45° branched 3D printed conductive PLA mandrel

3.4. Nitinol Stent Reinforcements

3.4.1. Stent Patterns

Nitinol stent rings of various patterns were successfully heat-set, as shown in Figure 3-33a. The body-temperature Nitinol stent-ring was capable of retaining a smaller diameter at room temperature, as shown in Figure 3-33b, thus it may be possible to be placed snugly over the electrospinning mandrel. Although these stent rings were heat-set on a 25 mm cylindrical mandrel, the expanded diameter in austenite form was slightly larger (≈30 mm) as shown in Figure 3-33b. The same effect was seen on the other stent patterns, as shown in Table 3-1.

The 500 µm wire produced two stents with very different expanded diameters (24.8 and 31.77 mm, herein denoted as 500 µm after-1 and 500 µm after-2, or D500-1 and D500-2, respectively), even though they were heat-set on the same mandrel, at the same time, using wires from the same spool. It was uncertain what may have caused the variations in the expanded diameter and why they were different to the diameters at heat-set.

a) 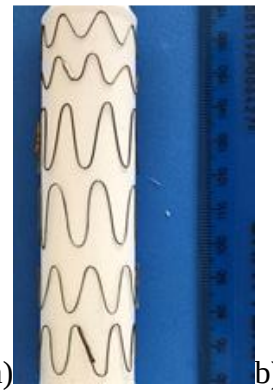 b) 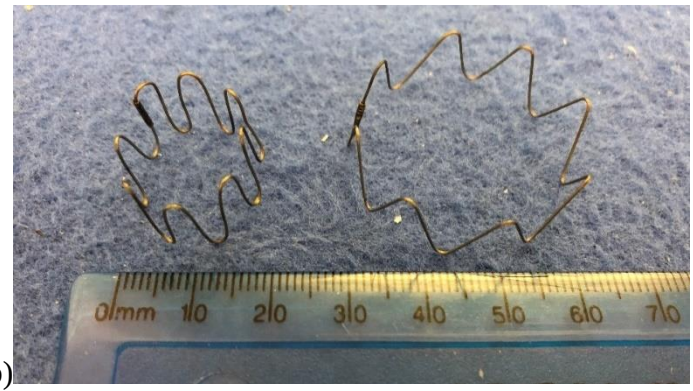

Figure 3-33 a) various Nitinol stent patterns after heat-set, b) crimped and expanded body temperature Nitinol stent ring at room temperature

Table 3-1 Expanded diameters of the various Nitinol stent patterns

	Expanded Diameter (mm)
S25-STD	29,54
S25-H05	29
S25-H15	35,74
S25-PD10	33,93
S25-PD20	35,33
S25-D250	31,95
S25-D500-1	24,8
S25-D500-2	31,77
S25-12W	27,18
S25-16W	28,93

3.4.2. Nitinol Transformation Temperature Determination

Figure 3-34 illustrates the typical DSC curve generated for a Nitinol sample, where the blue and red curves corresponds to the heating and cooling cycles respectively. The curve also shows the locations of the onset temperatures, which corresponds to the various transformation temperatures.

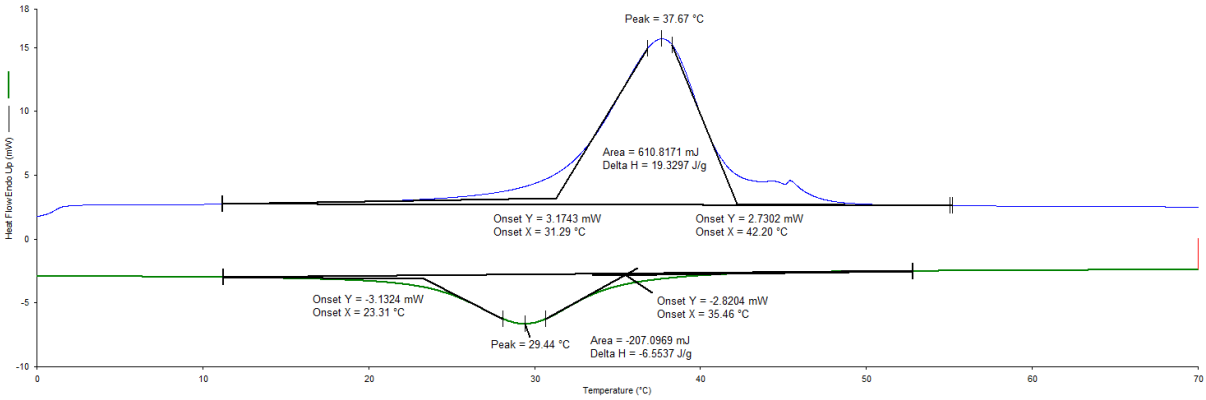

Figure 3-34 Example of the DSC test result for a 380 µm Nitinol wire sample after heat-set, generated on Pyris

Although the Nitinol wires that were procured were labelled as body temperature Nitinol, the DSC test results (Figure 3-36) show that the 380-µm wires had an Af only slightly higher than body temperature (37.0°C) before (42.3±2.4°C) and after (40.4±1.3°C) heat-set. The As was (29.5±1.9°C), which is above room temperature (20-25°C), and below body temperature; this is ideal because the stent ring may retain the crimped shape during electrospinning (martensitic form), and become superelastic when implanted (austenitic form).

The Af of the 250-µm wire was well below body temperature before heat-set (17.7±0.6°C), and increased above body temperature after heat-set (43.2±3.0°C). However, the As (9.6±2.0°C)

was still well below room temperature, which means it will not be able to retain the crimped shape when placed over the electrospun luminal layer at room temperature.

The 500-µm wires had an Af (62.4±4.1°C) much higher than body temperature before heat-set. After heat-set, D500-1 ("500 µm after-1") had a higher As (44.89±1.23°C) and Af (56.9±3.7°C) compared to the As (38.1±1.3°C) and Af (51.3±3.0°C) of D500-2 ("500 µm after-2"). The As and Af were both much higher than body temperature for D500-1, but the As was close to body temperature for D500-2. D500-2 showed two peaks on the DSC curve, whereas D500-1 only had one peak, as seen in Figure 3-35c; the first peak corresponds to the R phase, which may be a factor causing the difference between the expanded diameter after heat-set.

All wires had an Mf above 0°C after heat-set, which means the stent rings can be crimped to, and retain a smaller diameter in ice water.

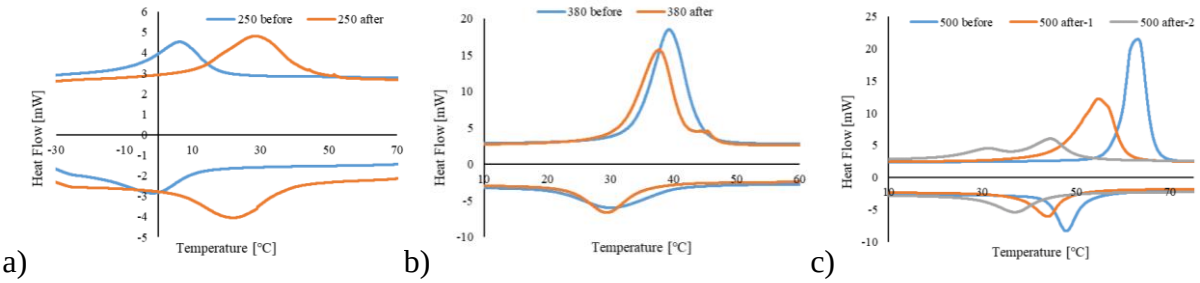

a) b) c)

Figure 3-35 DSC curves of Nitinol wires before and after heat-set, a) 250 µm wire, b) 380 µm wire, c) 500 µm wire

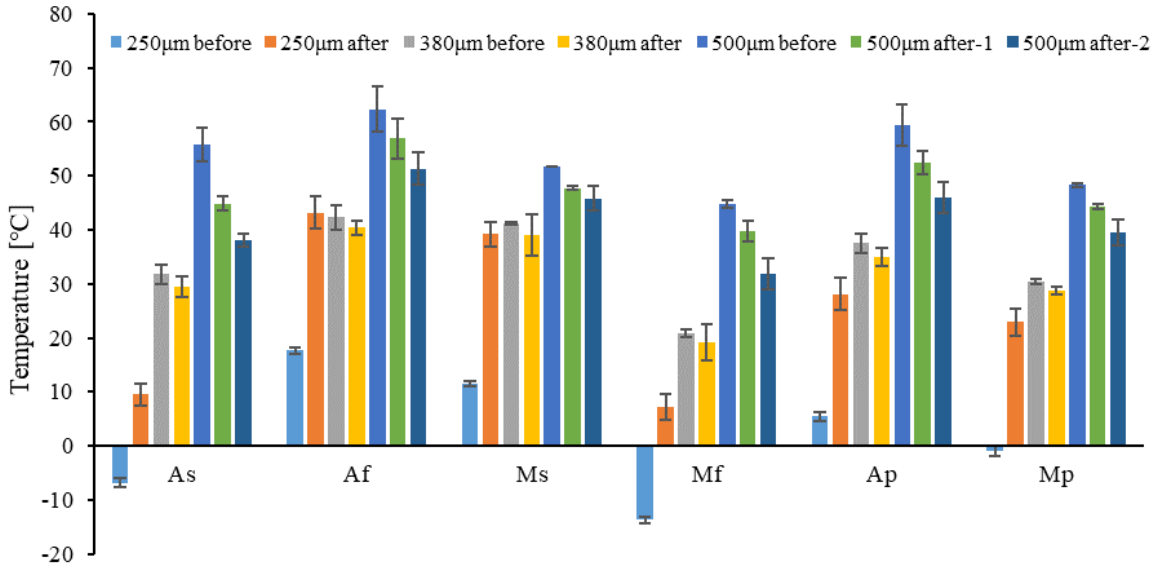

Figure 3-36 Transformation temperatures of Nitinol wires with different diameters, before and after heat-set

3.4.2.1. Summary

The transformation temperatures increased for 380 and 500 µm wires, and decreased for 250 µm wires, after heat-set.

After heat-set, only the 380-µm wire had an As within the ideal range between room and body temperature. The lower than room temperature As of the 250-µm wire means it cannot be overspun into the graft at room temperature. The higher than body temperature As of the 500-µm wires means its radial force at body temperature might not be optimal.

The Mf temperatures above 0°C showed that stent-rings wound with all different diameter wires can be crimped to a smaller diameter in ice water.

3.5. Stent Incorporation

S25-D250 was unable to be overspun into the scaffold as it could not retain the crimped shape at room temperature, as seen in Figure 3-37; this was due to the As being lower than room temperature as discussed in Section 3.4.2, and expands immediately after it was removed from the ice water. S25-12W and S25-16W became less sinusoidal in shape after heat-set, where the angle between the stent legs decreased, especially in S25-16W where the angle became negative, as shown in Figure 3-37; this may be due to the peaks being too close together, or the wave height-to-width ratio being too high.

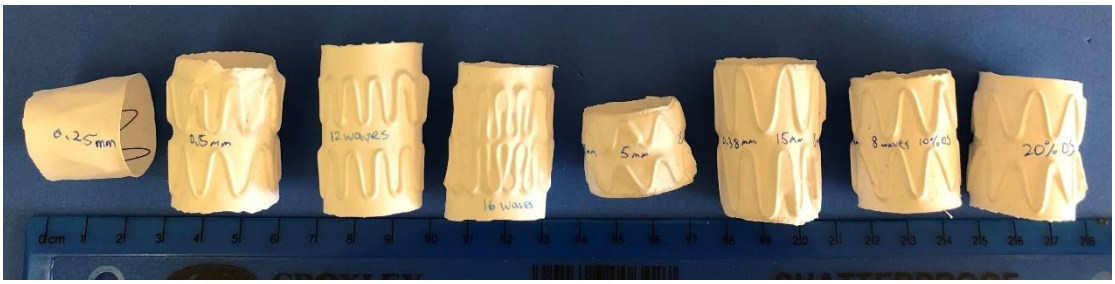

Figure 3-37 Electrospun stent-grafts using S25 mandrel and the various stent-pattern designs. From the left: S25-D250 SG, S25-D500 SG, S25-12W SG, S25-16W SG, S25-H05 SG, S25-H15 SG, S25-PD10, S25-PD20

The incorporation of body temperature Nitinol stent rings was possible on the P16 graft geometry (see Figure 3-38a), although heat-set on a cylindrical mandrel. The stent-graft was easily removed from the electrospinning mandrel with the aid of the Teflon spray, as shown in Figure 3-38b. However, Teflon particle residue may not be desirable; thus, methods of removing these particles and sterilising the stent-grafts should be performed before implant.

Figure 3-38c shows areas of the electrospun P16 stent-graft with close adhesion between the luminal and abluminal layers (blue), and areas with visible air gaps beneath the abluminal layer (red). The stent rings not conforming to the curvature of the P16 graft geometry, a high profile crimp or large irregularities of the stent ring may be the cause of the air gaps.

a) 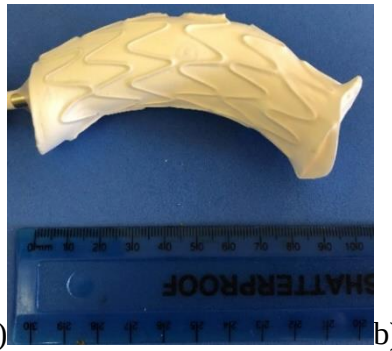 b)  c) 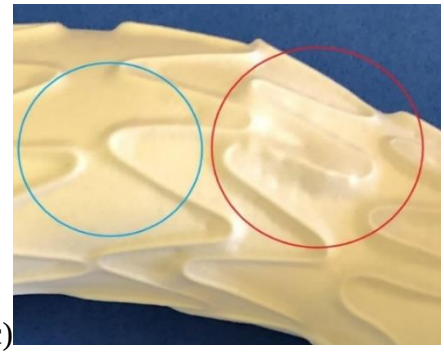

Figure 3-38 a) P16 geometry abluminal layer overspun on the stent rings, b) P16 stent-graft removed from electrospinning mandrel, c) areas of close adhesion (blue), and loose adhesion (red), between the abluminal and luminal layers of the graft scaffold around the stent

The graft layers closely encompassed the Nitinol wire as shown in Figure 3-39a, and only loosely encompassed the wire as shown in Figure 3-39b, leaving a larger air gap in between, similar to the "tent" effect when electrospinning on branched mandrels.

a) 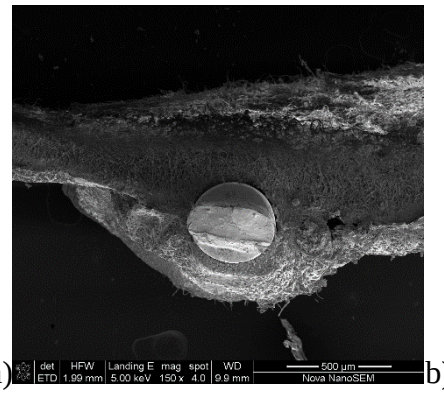 b) 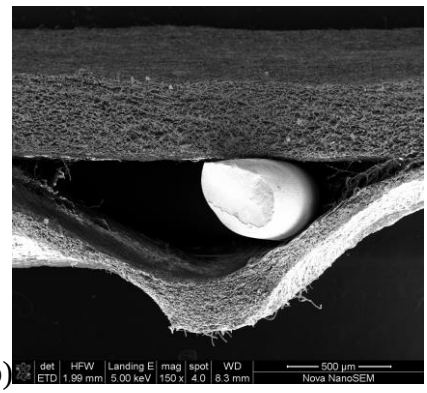

Figure 3-39 SEM images of electrospun Pellethane stent-graft on patient-specific P16 graft geometry, with 380 μm Nitinol wire incorporated, a) close adhesion of luminal and abluminal layers, b) larger gap between layers, 150X magnification, 500 μm scale bar

3.5.1. Radial Force Testing

3.5.1.1. Bare stent

The radial forces at 20% oversize (OS) were significantly higher than the radial forces at 10% OS for all the different stent patterns, as shown in Figure 3-40. The results discussed are of the 10% OS variations (Figure 3-40), unless stated otherwise:

The radial force of S25-STD (2.10±0.12 N, 10 mm stent height) was statistically lower than S25-H05 (7.30±0.11 N) and S25-H15 (2.44±0.05 N), although it was expected to be between S25-H05 and S25-H15.

The radial force of S25-D500-2 (4.98±0.06 N) was significantly higher than S25-D250 (0.80±0.03 N) and S25-STD (380 μm), whereas S25-D500-1 (0.71±0.15 N) was significantly lower than S25-STD, and similar to S25-D250. Although the radial force of both S25-D500

samples were expected to be higher than S25-STD, the low radial force of S25-D500-1 may be related to the DSC result, where the As was much higher than body temperature, but radial force tests were performed near body temperature.

The mean radial force of S25-PD20 (4.30±0.12 N) was slightly higher than S25-PD10 (4.19±0.08 N), but it was not statistically significant. The change in radial force was not linear between S25-STD (0% pre-deformation), S25-PD10, and S25-PD20; the radial force of S25-PD10 was twice as high compared to S25-STD, but S25-PD20 was only 2.57% higher than S25-PD10.

The radial force of S25-12W (1.89±0.09 N) and S25-16W (1.53±0.09 N) were significantly lower than S25-STD (8 waves), although they were expected to be higher.

S25-STD showed a similar radial force compared to Medtronic stents (2.23±0.03 N), but was significantly lower than Cook Medical stents (3.61±0.43 N). S25-H05 showed the highest radial force between all the stents tested (10% OS: 7.30±0.11 N, 20% OS: 7.78±0.07 N).

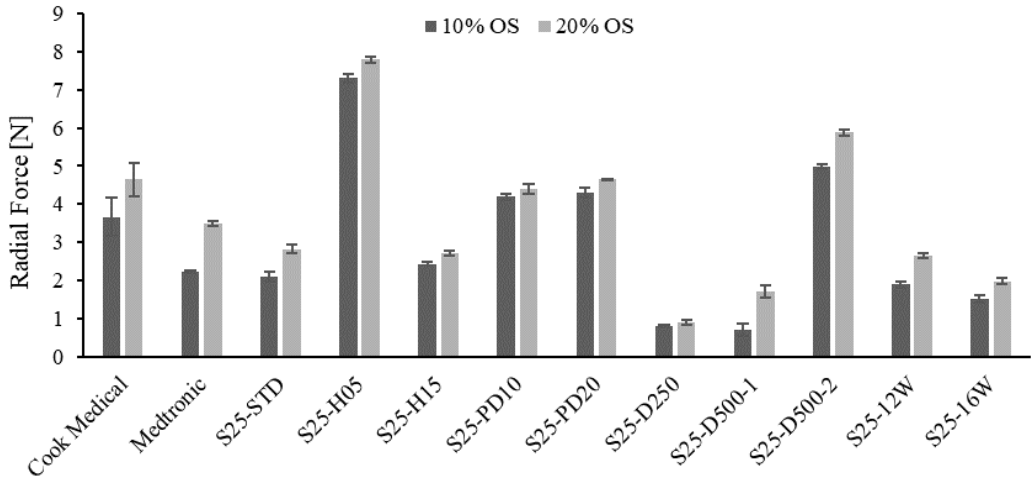

Figure 3-40 Mean radial force of bare stent-rings

3.5.1.2. Stent-graft

The stent-grafts also show significantly higher radial forces at 20% OS compared to 10% OS, as shown in Figure 3-41.

With the stent incorporated, (discussed for 10% OS results shown in Figure 3-41, unless stated otherwise) the radial force of S25-12W SG (4.89±0.45 N) and S25-16W SG (4.57±0.41 N) increased compared to the bare stents, and were significantly higher than S25-STD SG (2.77±0.06 N), as shown in Figure 3-41. However, contrary to expectations, the radial force of S25-16W SG was not significantly higher than S25-12W SG. This may be due to the 16-wave pattern no longer being sinusoidal in shape, as discussed in Section 3.5.

The radial force of S25-D250 SG (1.27±0.09 N) was significantly lower than S25-STD SG, and S25-D500 (5.08±0.15 N) was significantly higher than both. The effect of wire diameter on the radial force of the stent-graft were as expected (RF 250 μm<RF 380 μm<RF 500 μm).

The radial force of S25-PD10 SG (4.32±0.07 N) was significantly lower than S25-STD SG, and S25-PD20 SG (4.50±0.12 N) was significantly higher than both. The effect of stent pre-deformation on the radial force of the stent-graft were as expected (RF 0%<RF 10%<RF 20% PD), unlike in the bare stent case. However, the change was still not linear from S25-STD SG to S25-PD20 SG, and the mean radial force of S25-PD20 SG was only 4.1% higher than S25-PD10 SG.

The radial force of S25-H05 SG (5.81±0.50 N) was significantly higher than S25-H15 SG (4.07±0.19 N), and S25-STD SG was significantly lower than S25-H15 SG; S25-STD SG was expected to fall between S25-H05 SG and S25-H15 SG, but this was not the case. However, S25-PD10 SG and S25-PD20 SG (which had the same parameters as S25-STD SG except for pre-deformation (PD)), had radial forces that fell between S25-H05 SG and S25-H15 SG.

All electrospun stent-grafts had statistically higher radial forces compared to the Medtronic stent-graft (2.77±0.58 N), except for S25-D250 SG (1.27±0.09 N), which was significantly lower. Only S25-STD SG, S25-D250 SG, and PS-P16 SG (3.11±0.23 N) had radial forces that were statistically lower than the Cook Medical stent-graft (3.85±0.36 N), whereas the other stent-grafts were significantly higher. This means that, using commercial stent-graft radial force as a guideline, these electrospun Nitinol stent-grafts with equivalent or higher radial forces may provide adequate fixation force. S25-H05 SG showed the highest radial force between all the stent-grafts tested (10% OS: 5.81±0.50 N, 20% OS: 6.91±0.56 N).

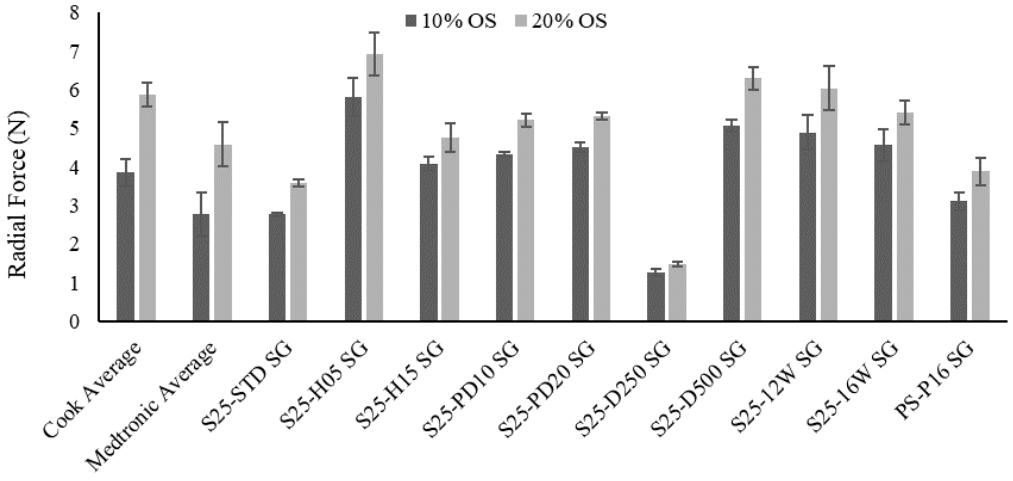

Figure 3-41 Mean radial force of stent-grafts

3.5.1.3. Summary

Various stent patterns produced adequate radial force (equivalent or higher than commercial stent-grafts) when electrospun into stent-grafts. The electrospun patient-specific P16 stent-graft also showed adequate radial force compared to the Medtronic stent-graft.

The radial force of the stent-graft produced was increased by a decrease in stent-height, increase in wire diameter, increase in percentage pre-deformation, and increase in number of waves, with the decrease in stent-height showing the most prominent effect. However, hand-wound Nitinol stents showed counter-intuitive results for a large number of waves.

3.5.2. Delamination Resistance Determination

There was no statistical difference in the mean delamination force between the plain scaffold (0.153±0.045 N) and the scaffold incorporated with a stent (0.211±0.069 N), and that the delamination force between the layers was not significantly affected by the inclusion of the stent. The combined mean delamination force was 0.182±0.062 N.

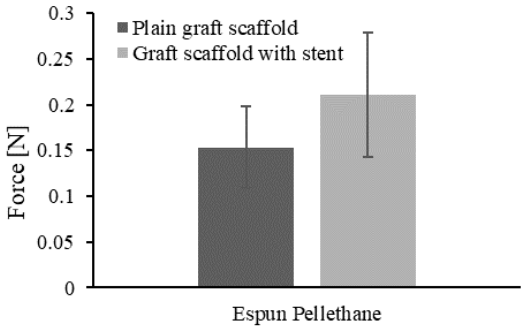

Figure 3-42 Mean delamination force of the electrospun Pellethane scaffolds, 5 mm width samples

3.6. FEA Simulation

3.6.1. Poisson's Ratio Determination

The Poisson's ratio of the electrospun Pellethane scaffold was higher compared to the Cook Medical and Medtronic graft scaffolds, which indicates it experiences larger transverse strain when longitudinally loaded; this may be due to the higher elasticity of the electrospun grafts.

Table 3-2 Poisson's ratio test results for commercial woven, and electrospun graft scaffolds

	Poisson's Ratio		
Sample	10% ε	20% ε	30% ε
Cook C	0.0863	0.1183	0.1542
Cook L	0.0915	0.0608	0.0765
Medtronic C	0.3042	0.2610	0.2163
Medtronic L	0.0477	0.1428	0.1244
ESpun C	0.3593	0.3401	0.3725
ESpun L	0.1970	0.2946	0.3922

3.6.2. Simulation Result

The customised stent-graft showed larger areas with higher contact traction and seal, less areas with no contact with the aorta, lower von Mises stent stress, and more evenly distributed areas with high von Mises vessel stress and overstress, as shown in Figure 3-43. This confirms that customised stent-grafts may result in less leakage, more uniform force distribution on the aorta, and less chance of stent-graft migration.

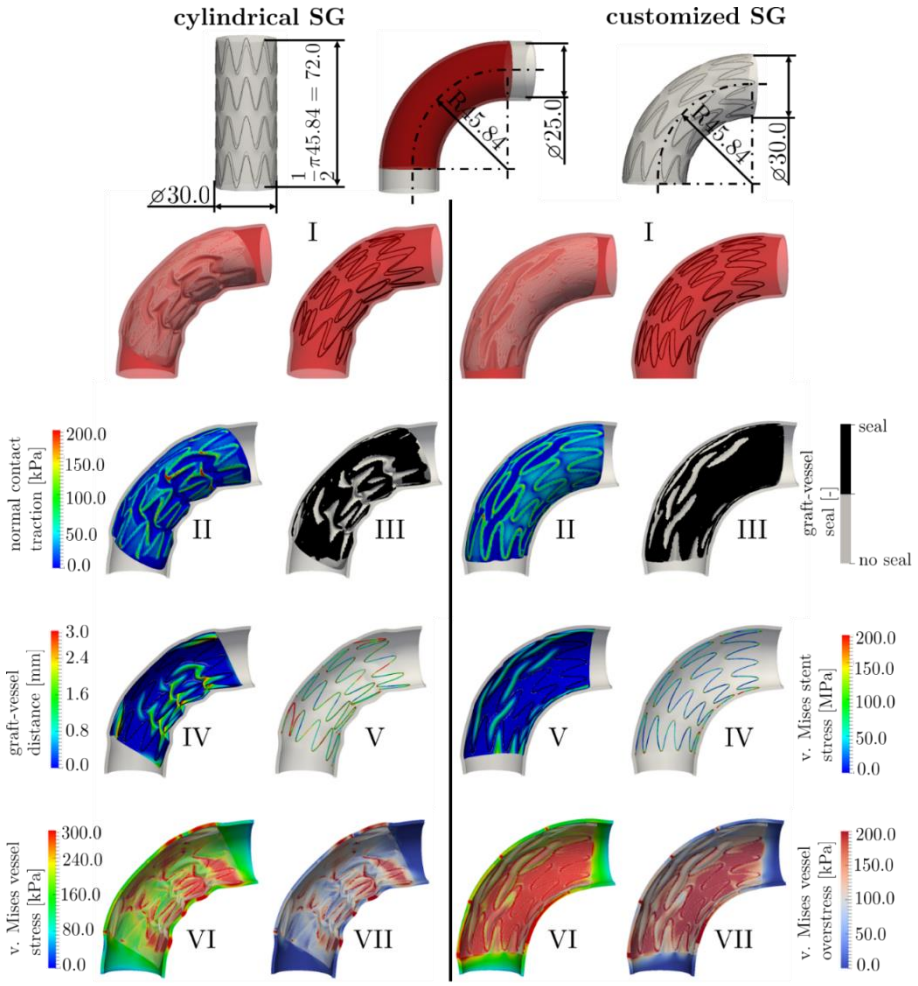

Figure 3-43 Simulation result comparing a standard cylindrical, and a customised stent graft in a simplified curved aortic geometry

The comparison of simulation and experimental results on the radial force generated by a 25 mm diameter electrospun stent-graft in Figure 3-44 show that the hysteresis effect in the simulation was much less prominent compared to the experimental results, and the simulation results were approximately in between the values of the loading and unloading cycles. This may be due to the way boundary conditions and assumptions were setup in order to simplify the simulation. However, the simulation data followed a trend in close relation to the experimental results. Although the predictions may not be exact, it may provide an acceptable prediction.

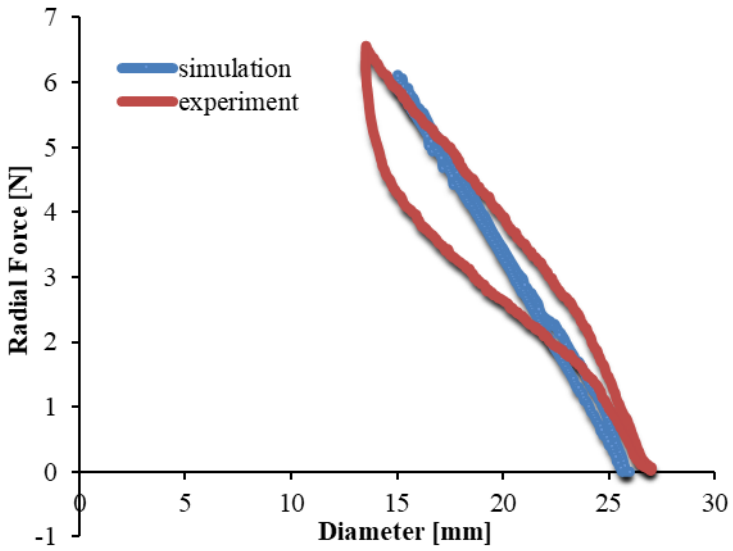

Figure 3-44 Simulation and experimental radial force comparison on a S25 electrospun stent-graft

3.6.2.1. Summary

The simulation results indicate that by using a customised stent-graft geometry that conforms to the aortic geometry, there may be various advantages over using a standard stent-graft.

Simulation results on the S25 electrospun stent-graft showed close approximations of the experimental results.

3.7. Mock Insertion

Although the 3D printed transparent PLA aortic model was not flexible, it can be seen that the P16 stent-graft conformed well to the P16 aortic geometry in Figure 3-45. Although the filament used was indeed transparent, the 3D printed aortic model was only translucent due to the layer lines; in order to see the inserted stent-graft, camera flash or a backlight had to be used when taking pictures.

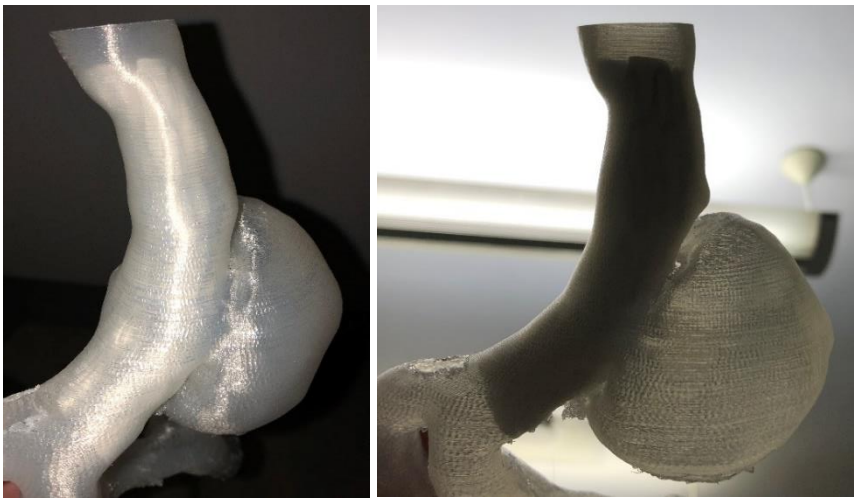

Figure 3-45 Mock insertion of electrospun P16 stent-graft into a 3D printed transparent PLA P16 aortic model

4. Conclusions

Anonymous-patient aortic models 3D reconstructed in Mimics allowed the creation of patient-specific stent-graft geometry designs, with conservation of the native blood vessel geometry, and exclusion of the aneurysm. Patient-specific stent-graft geometries designed in SolidWorks conserved the curvature of the aorta, but were much simplified, and not as precise as those designed in Mimics were.

Idealised and patient-specific stent-graft geometries were successfully 3D printed using Proto-Pasta conductive PLA filament, which showed promising results as electrospinning mandrels, with improved conductivity and surface finish over 3D-printed standard PLA mandrels; the surface was much improved using sanding (100-1200 grit) and THF vapour smoothing.

Humidity-control-system improvements produced electrospun scaffolds with relatively consistent and reproducible morphology and mechanics. Scaffolds with full coverage and uniform fibre deposition were successfully electrospun with a 16 wt% Pellethane solution on idealised and patient-specific conductive PLA mandrels at 290-300 mm mandrel to needle distance, +18 and -3 kV high voltage supply, 750-1000 rpm mandrel rotation speed, 5 ml/hr solution feed rate, 5 mm/s translation speed, and 40-60% RH. Electrospinning of branched electrospun scaffolds had unsuccessful results using the current equipment, with “tent”-ing effects due to the obstruction of the branches.

Electrospun scaffolds were generally thicker near the centre of the mandrel compared to the ends, near the larger end compared to the smaller end of tapered mandrels, near the peak of curved mandrels, and on the peak of the major axis for elliptical mandrels; thickness variation differences decrease as the shape normalises to a cylindrical shape. The mean Young’s Modulus, UTS, and maximum strain of the electrospun scaffolds were 1.87±0.56 MPa, 7.29±2.44 MPa, and 571±75% respectively, where the Young’s Modulus and UTS were significantly higher in the longitudinal direction compared to the circumferencial direction. SEM imaging and analysis on the idealised geometry electrospun scaffolds showed that shape variations did not have a prominent effect on the coherency of fibres, fibre diameter, and pore size, which had a mean of 0.35±0.15, 2.33±0.36 μm, and 7.52±1.20 μm, respectively. This translates to a scaffold with relatively random fibre orientation with previously proven endothelialisable pore size.

Various hand-wound Nitinol wire sinusoidal stent patterns, heat-set on standard one inch (25.4 mm Ø) aluminium tube in fluidised bath, were successfully incorporated into the

idealised and patient-specific grafts by overspinning the abluminal layer, and produced promising radial forces comparible to or higher than commercial Nitinol stent-grafts (2.77±0.58 N). The radial force of the stent-graft increased with an increase in percentage pre-deformation of the stent ring, number of waves, and wire diameter, and a decrease in stent height. The stent height showed the most prominent effect (2x radial force with 5 vs 10 mm stent height at 10% OS), and a large number of waves showed counter-intuitive effects due to the pattern no longer being sinusoidal. DSC test results showed the 250-µm and 500-µm diameter Nitinol wires used did not have As temperatures within the ideal range between room and body temperature as in the case of the 380-µm wire, thus had undesirable effects on the production process and mechanics at working condition. The successfulness and effectiveness of the abluminal layer in closely encompassing the stent onto the luminal layer depend highly on the conformity of the stent on the luminal layer during electrospinning, as well as the stent footprint; the luminal and abluminal layers had a mean delamination force of 0.182±0.062 N.

FEA simulation on a simplified curved aortic geometry showed various advantages of using customised stent-grafts over standard, off-the-shelf devices, such as more surface traction, better seal, and more evenly distributed stresses; this translates to less chance of endoleaks and stent-graft migration, as well as an increased lifespan of the device. The radial force simulation showed close approximations to experimental results, albeit with less hysteresis effect.

Mock insertion of the electrospun patient-specific stent-graft into the 3D-printed transparent-PLA hollow aortic model showed good conformity. However, the model did not have sufficient transparency, and was not flexible enough to mimic the mechanics of the aorta.

Proof of concept was achieved in rapid prototyping patient-specific stent-grafts with the use of digitised CT scan data, 3D printing, electrospinning and Nitinol shape-setting methods.

5. Recommendations

The following improvements, which were not fully implemented in the current work due to lack of resources (or that fell outside the scope of the study), are recommended.

Although the patient-specific graft design on Mimics was precise, manually erasing the aneurysm on each CT scan layer is very time consuming, thus methods of automating the process or producing optimised graft geometry computationally could be developed.

Although casting or 3D printing of the electrospinning mandrel from metal might provide better conductivity, conductive PLA mandrels (as used in this study) may be preferable in terms of cost and manufacturing time.

Although the humidity control system allowed relatively reproducible and consistent scaffolds to be electrospun, temperature control could also be implemented to improve the consistency, as well as allow Nitinol stents with low As temperatures to be overspun, thus reducing the limitations of the current equipment.

Other polymers could be evaluated to achieve optimal properties in terms of biocompatibility, possible drug elusion, scaffold morphology, and mechanics such as burst strength, water entry pressure, water permeability, and kink resistance.

More control over the rotation could be implemented, e.g. by replacing the current motor with a stepper motor will allow for more control, especially at low speeds, if required.

A real-time needle adjustment system could be implemented, so the needle can be angled to deposit under angled branches, as well as to adjust the mandrel to needle distance in real-time so equidistance electrospinning can be achieved irrespective of the mandrel shape; this may be assisted using infrared, ultrasonic, laser distance detectors, or hard-coded according to mandrel geometry. The thickness variation of the scaffolds could also be compensated by using software to adjust spinning time at different locations on the mandrel.

Improved methods of wrapping post placement on the patient-specific heat-set mandrel geometry in CAD software could be developed to accelerate the design process. Patient-specific heat-set mandrels with the inclusion of wrapping posts can be 3D printed using titanium using similar designs as the one shown in Section 2.4.6; this will allow stents rings that conform to the patient-specific anatomy to be developed.

A source for obtaining Nitinol wire with the desired/required transformation temperatures should be found.

Alternatively, stent rings could be laser cut from Nitinol tubes to produce more accurate designs with a smaller stent profile and fewer irregularities, since crimping of the ends will no longer be required. This will also decrease manual labour since stents are no longer required to be hand wound.

Stent ring placement could also be further investigated, taking into account the distance and phase angle between adjacent stent rings, as well as overlapped stent ring designs, to determine designs that work effectively with electrospinning and produce stent-grafts with less kinks in the scaffold. Fatigue testing could also be performed on the electrospun stent-grafts.

Radiopaque markers attachment methods could be investigated.

FEA simulation could be used to determine the optimal stent pattern and graft geometry designs for use with patient-specific anatomies.

The hollow aortic model could be made with a flexible transparent material, which can be casted using transparent silicone or clear urethane rubber in a 3D printed mould, or 3D printed with transparent and flexible silicone-like materials. Mock delivery using a catheter, as well as mock circulation tests could also be done on the stent-grafts.

6. Research Output

6.1. Peer reviewed papers

Submitted

Hemmler, A., Lin A., Thierfelder, N., Franz, T., Gee, M. W., Bezuidenhout, D. (2019)

Customized Stent-Grafts for Endovascular Aneurysm Repair with Challenging Necks: a Numerical Proof of Concept. *Journal of Biomechanical Engineering.*

In preparation (2019)

Lin. A, Thierfelder, N., Hemmler, A., Franz, T., Zilla, P., Bezuidenhout, D.

Patient-Specific Endovascular Aortic Repair (EVAR). *Journal of Biomedical Materials Research Part B.*

References

Aggarwal, S., Qamar, A., Sharma, V., & Sharma, A. (2011). Abdominal aortic aneurysm: A comprehensive review. *Experimental & Clinical Cardiology, 16*(1), 11-15.

Arslan, B., Turba, U. C., Sabri, S., Angle, J. F., & Matsumoto, A. H. (2009). Current Status of Percutaneous Endografting. *Seminars in Interventional Radiology, 26*(1), 67-73. doi:10.1055/s-0029-1208387

Benjamin, E. J., Blaha, M. J., Chiuve, S. E., Cushman, M., Das, S. R., Deo, R., . . . Stroke Statistics, S. (2017). Heart Disease and Stroke Statistics-2017 Update: A Report From the American Heart Association. *Circulation, 135*(10), e146-e603. doi:10.1161/cir.0000000000000485

Chang, R. W., Goodney, P., Tucker, L.-Y., Okuhn, S., Hua, H., Rhoades, A., . . . Hill, B. (2013). Ten-year results of endovascular abdominal aortic aneurysm repair from a large multicenter registry. *Journal of Vascular Surgery, 58*(2), 324-332. doi:10.1016/j.jvs.2013.01.051

Chlupac, J., Filova, E., & Bacakova, L. (2009). Blood vessel replacement: 50 years of development and tissue engineering paradigms in vascular surgery. *Physiol Res, 58 Suppl 2*, S119-139.

CookMedical. (2011). Zenith Flex AAA Endovascular Graft Planning and Sizing. Retrieved from https://www.cookmedical.com/data/resources/AI-BM-FXSZPSPPT-EN-201104.pdf [Accessed on: 09/02/2019]

Dake MD, Miller DC, & Semba CP. (1994). Transluminal placement of endovascular stent-grafts for the treatment of descending thoracic aortic aneurysms. *N Engl J Med 1994;331:1729–34*(1).

Davis, A., Holloway, C., Lewandowski, A. J., Ntusi, N., Nethononda, R. M., Pitcher, A., . . . Rider, O. J. (2013). Diameters of the normal thoracic aorta measured by cardiovascular magnetic resonance imaging; correlation with gender, body surface area and body mass index. *Journal of Cardiovascular Magnetic Resonance, 15*(1), E77. doi:10.1186/1532-429x-15-s1-e77

Desai, N. D., Gottret, J.-P., Szeto, W. Y., McCarthy, F., Moeller, P., Menon, R., . . . Bavaria, J. E. (2015). Impact of timing on major complications after thoracic endovascular aortic repair for acute type B aortic dissection. *The Journal of Thoracic and Cardiovascular Surgery, 149*(2, Supplement), S151-S156. doi:https://doi.org/10.1016/j.jtcvs.2014.10.105

DIYElectronics. (2019). diyelectronics prusa i3 premium kit. Retrieved from https://www.diyelectronics.co.za/store/2128-thickbox_default/diyelectronics-prusa-i3-premium-kit.jpg [Accessed on: 04/02/2019]

Elefteriades, J. A., & Farkas, E. A. (2010). Thoracic Aortic Aneurysm: Clinically Pertinent Controversies and Uncertainties. *Journal of the American College of Cardiology, 55*(9), 841-857. doi:https://doi.org/10.1016/j.jacc.2009.08.084

EngineeringToolBox. (2008). Resistance and Resistivity. Retrieved from https://www.engineeringtoolbox.com/resistance-resisitivity-d_1382.html [Accessed on: 04/02/2019]

England, A., & Mc Williams, R. (2013). Endovascular Aortic Aneurysm Repair (EVAR). *The Ulster Medical Journal, 82*(1), 3-10.

Erbel, R., & Eggebrecht, H. (2006). Aortic dimensions and the risk of dissection. *Heart, 92*(1), 137-142. doi:10.1136/hrt.2004.055111

Findeiss, L. K., & Cody, M. E. (2011). Endovascular Repair of Thoracic Aortic Aneurysms. *Seminars in Interventional Radiology, 28*(1), 107-117. doi:10.1055/s-0031-1273945

FWMetals. (2017). Nitinol [online]. Retrieved from http://www.fwmetals.com/materials/nitinol/ [Extracted on: 03/08/2017]

Gilbert, H. B., & Webster, R. J. (2016). Rapid, Reliable Shape Setting of Superelastic Nitinol for Prototyping Robots. *IEEE robotics and automation letters, 1*(1), 98-105. doi:10.1109/LRA.2015.2507706

Guidoin, R., Maurel, S., Chakfe, N., How, T., Zhang, Z., Therrien, M., . . . Gosselin, C. (1993). Expanded polytetrafluoroethylene arterial prostheses in humans: chemical analysis of 79 explanted specimens. *Biomaterials, 14*(9), 694-704.

Hasan, A., Memic, A., Annabi, N., Hossain, M., Paul, A., Dokmeci, M. R., . . . Khademhosseini, A. (2014). Electrospun scaffolds for tissue engineering of vascular grafts. *Acta Biomaterialia, 10*(1), 11-25. doi:https://doi.org/10.1016/j.actbio.2013.08.022

Hemmler, A., Lutz, B., Reeps, C., Kalender, G., & Gee, M. W. (2018a). A methodology for in silico endovascular repair of abdominal aortic aneurysms. *Biomechanics and Modeling in Mechanobiology*. doi:10.1007/s10237-018-1020-0

Hemmler, A., Lutz, B., Reeps, C., Kalender, G., & Gee, M. W. (2018b). A methodology for in silico endovascular repair of abdominal aortic aneurysms, Biomechanics and Modeling in Mechanobiology. *17*(4), 1139–1164. doi:https://doi.org/10.1007/s10237-018-1020-0

JohnsonMedicalComponents. (2018a). Biocompatibility of Nitinol. Retrieved from http://jmmedical.com/resources/241/Biocompatibility-of-Nitinol.html

JohnsonMedicalComponents. (2018b). Nitinol Shape Setting [Online]. Retrieved from http://jmmedical.com/resources/251/Nitinol-Shape-Setting.html [Extracted on: 27/02/2018]

Kishan A, C.-H. E. (2017). Recent advancements in electrospinning design for tissue engineering applications: A review. doi:10.1002/jbm.a.36124

Krieger, A., HIBINO, N., Johnson, J., Opfermann, J., Cochenour, C., & Breuer, C. K. (2017). WO 2017/035500 A1. PCT: WIPO.

Leotta DF, S. B. (2015). Custom Fenestration Templates for Endovascular Repair of Juxtarenal Aortic Aneurysms. *J Vasc Surg. 2015 June; 61(6): 1637–1641*. doi:doi:10.1016/j.jvs.2015.02.016

Memry. (2017). Introduction to NItinol(Rev 0). Retrieved from https://daks2k3a4ib2z.cloudfront.net/59fcbaf103e295000131288b/5a4bb3895344bc000191bac9_Introduction%20to%20Nitinol_V5.pdf [Accessed on: 2019/02/01]

Moravej, M., & Mantovani, D. (2011). Biodegradable Metals for Cardiovascular Stent Application: Interests and New Opportunities. *International Journal of Molecular Sciences, 12*(7), 4250-4270. doi:10.3390/ijms12074250

Morris, L., Stefanov, F., Hynes, N., Diethrich, E. B., & Sultan, S. (2016). An Experimental Evaluation of Device/Arterial Wall Compliance Mismatch for Four Stent-Graft Devices and a Multi-layer Flow Modulator Device for the Treatment of Abdominal Aortic Aneurysms. *European Journal of Vascular and Endovascular Surgery, 51*(1), 44-55. doi:https://doi.org/10.1016/j.ejvs.2015.07.041

Mozaffarian, D., Benjamin, E. J., Go, A. S., Arnett, D. K., Blaha, M. J., Cushman, M., . . . Turner, M. B. (2015). Heart Disease and Stroke Statistics—2016 Update. *A Report From the American Heart Association*. doi:10.1161/cir.0000000000000350

National Centre for Injury Prevention And Control. (2007). WISQARS Leading Causes of Death Reports, 1999 - 2007. Retrieved from https://webappa.cdc.gov/sasweb/ncipc/leadcaus10.html

National Heart Lung and Blood Institute (Producer). (2019). Aortic Aneurysm. Retrieved from https://www.nhlbi.nih.gov/sites/default/files/inline-images/aneurysm_endo-repair.png [Accessed on: 23/05/2019]

Parodi, J. C., Palmaz, J. C., & Barone, H. D. (1991). Transfemoral Intraluminal Graft Implantation for Abdominal Aortic Aneurysms. *Annals of Vascular Surgery, 5*(6), 491-499. doi:10.1007/BF02015271

Prinssen, M., Verhoeven, E. L. G., Buth, J., Cuypers, P. W. M., van Sambeek, M. R. H. M., Balm, R., . . . Blankensteijn, J. D. (2004). A Randomized Trial Comparing Conventional and Endovascular Repair of Abdominal Aortic Aneurysms. *New England Journal of Medicine, 351*(16), 1607-1618. doi:10.1056/NEJMoa042002

ProtoPasta. (2019). Conductive PLA. Retrieved from https://www.proto-pasta.com/pages/conductive-pla [Accessed on: 04/02/2019]

Rabih A Chaer, M. (2018). Endovascular devices for abdominal aortic repair. Retrieved from https://www.uptodate.com/contents/endovascular-devices-for-abdominal-aortic-repair

Reneker, D. H., & Yarin, A. L. (2008). Electrospinning jets and polymer nanofibers. *Polymer, 49*(10), 2387-2425. doi:https://doi.org/10.1016/j.polymer.2008.02.002

Roll, S., Müller-Nordhorn, J., Keil, T., Scholz, H., Eidt, D., Greiner, W., & Willich, S. N. (2008). Dacron(®)vs. PTFE as bypass materials in peripheral vascular surgery – systematic review and meta-analysis. *BMC Surgery, 8*, 22-22. doi:10.1186/1471-2482-8-22

Ronald M Fairman, M. A. C., MD. (2018). Endovascular devices for thoracic aortic repair. Retrieved from https://www.uptodate.com/contents/endovascular-devices-for-thoracic-aortic-repair

Roth, G. A., Johnson, C., Abajobir, A., Abd-Allah, F., Abera, S. F., Abyu, G., . . . Murray, C. (2017). Global, Regional, and National Burden of Cardiovascular Diseases for 10 Causes, 1990 to

2015. *Journal of the American College of Cardiology, 70*(1), 1-25. doi:https://doi.org/10.1016/j.jacc.2017.04.052

Sampson, U. K. A., Norman, P. E., Fowkes, F. G. R., Aboyans, V., Yanna, S., Harrell, F. E., . . . Murray, C. (2014). Global and Regional Burden of Aortic Dissection and Aneurysms: Mortality Trends in 21 World Regions, 1990 to 2010. *Global Heart, 9*(1), 171-180.e110. doi:https://doi.org/10.1016/j.gheart.2013.12.010

Steuer, J., Lachat, M., Veith, F. J., & Wanhainen, A. (2016). Endovascular grafts for abdominal aortic aneurysm. *European Heart Journal, 37*(2), 145-151. doi:10.1093/eurheartj/ehv593

Technavio. (2016). *Global TEVAR Market 2016-2020*. Retrieved from https://www.researchmoz.us/global-tevar-market-2016-2020-report.html [Accessed on: 25/03/2018]

Timothy, R. (2016). Custom-Made Devices: Current State of the Art. *ENDOVASCULAR TODAY MARCH 2016, 15*(3).

van den Bergh, W. J. W. (2018). *Drug eluting electrospun scaffolds for tissue regeneration.* (MSc (Med) Biomedical Engineering), University of Cape Town,

World Health Organization. (2018). The top 10 causes of death. Retrieved from https://www.who.int/en/news-room/fact-sheets/detail/the-top-10-causes-of-death [Accessed on: 08/02/2019]

Zenkiewicz, M., Richert, J., Rytlewski, P., & Richert, A. (2011). *Selected electrical and thermal properties of polylactide/graphite composites* (Vol. 56).

Zhang, M.-H., Du, X., Guo, W., Liu, X.-P., Jia, X., & Ge, Y.-Y. (2017). Early and midterm outcomes of thoracic endovascular aortic repair (TEVAR) for acute and chronic complicated type B aortic dissection. *Medicine, 96*(28), e7183. doi:10.1097/md.0000000000007183

Zhang, Z., Wang, Z., Liu, S., & Kodama, M. (2004). Pore size, tissue ingrowth, and endothelialization of small-diameter microporous polyurethane vascular prostheses. *Biomaterials, 25*(1), 177-187. doi:https://doi.org/10.1016/S0142-9612(03)00478-2

7. Appendices

7.1. Electrospinning Standard Operating Procedure

Starting procedure

1. Make sure both high voltage power supplies and the electrospinning rig are switched off.
2. Attach the electrospinning mandrel onto the metal rod, attach the sleeve bushing depending on the rod diameter, insert and secure the rod in the chuck, and attach the magnetic mount over the sleeve bushing.
3. Adjust the stationary needle holder to the desired position, and secure using the attached screws.
4. Manually pull the stage towards the outside of the rig while powered down until it reaches the end. Align the inside end of the mandrel with the needle as desired, adjusting either the mandrel or the needle holder as necessary.
5. Switch on the electrospinning rig and the connected computer.
6. On the computer, start the program “ElectroSpinning.exe” on the desktop.
    a. Select the correct COM port for the connected Arduino. Wait 5 seconds after the port is selected, if humidity and temperature readings show up, the correct port has been selected.
    b. Set the electrospinning parameters (make sure oscillation speed has a negative value) and press configure. A message should pop up to confirm successful configuration.

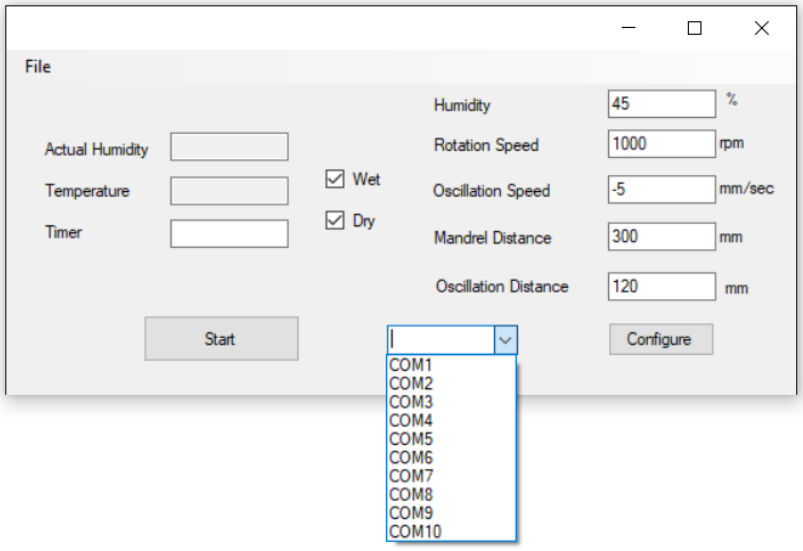

7. Attach the syringe with the polymer solution onto the syringe pump, insert the needle through the access hole on the side of the box and around 10 mm through the hole in the metal plate.
    a. Slightly shift the plate sideways to ensure good contact with the needle, and then tighten the screw.
    b. Make sure there is at least 5 ml more solution in the syringe than the intended amount to be used, as some will be needed to prime the Teflon tube.
8. On the computer, press the start button on the electrospinning program as it takes some time to home the stage, get to the programmed position, and start spinning.
9. While the stage is homing, set the syringe size, volume of solution to be electrospun and the flow rate on the syringe pump, and then press start.
10. Once the Teflon tube is primed and solution starts to flow out through the needle, stop the syringe pump, and wipe the needle tip with tissue.
11. Fill the humidifier reservoir with water, up to the 40 ml mark. Before closing the lid, make sure to push the wick up slightly towards the lid so it makes direct contact with the nebulizer.
12. Once the electrospinning rig has started to spin and translate as desired, close the rig doors.
13. Using the buttons and screen on the humidity controller, set the desired humidity. Once the humidity stabilizes between the set-points, start the syringe pump again.
14. Once the solution starts to flow out at the needle tip again, switch on the high voltage power supply immediately. Adjust the voltages until a cone is formed at the tip of the needle without droplets of solution forming. Check the timer on the syringe pump and let the rig electrospin until completed.

<u>Stopping procedure</u>

1. Once the electrospinning process has been completed, switch off the high voltage power supplies first. Make sure to wait a few seconds for the power to completely switch off before touching any components connected to the rig.
2. Switch off the syringe pump and stop the electrospinning process from the computer.
3. Open the rig doors and let it air out for at least one minute before handling the specimen.
4. Make sure to empty out any unused solution from the syringe after the electrospinning process has been completed. Rinse the syringe and connected piping with the relevant solvent, and then leave it to air dry.
5. Switch off electrospinning rig after experiments are completed.

7.2. P16 Electrospinning Iterations

Four iterations were performed on the P16 graft geometry:

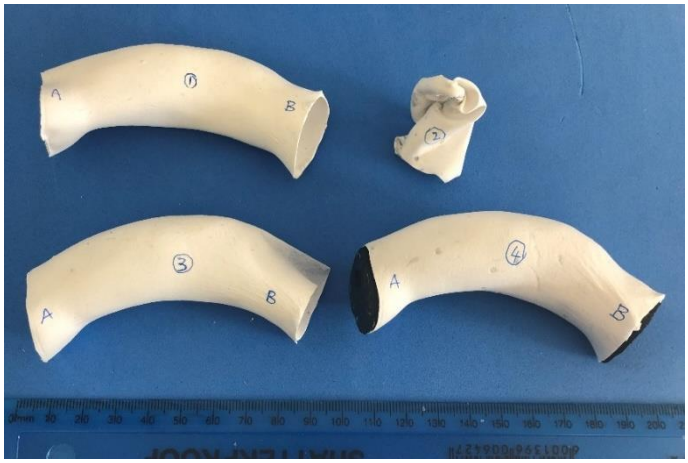

Before the first iteration, the graft was electrospun at the same conditions as those used for the simple geometry mandrels (1000 rpm, 300 mm from needle, +18 kV, -3 kV, 5 ml/hr, 5 mm/s translation speed). It was discovered that due to the P16 mandrel being mounted on one end only, as well as due to the curvature of the geometry, the vibrations generated were very high, thus the rotation speed was decreased to 750 rpm. There were also issues of fibre coverage on the mandrel; side A had less coverage compared to side B in iteration 1, wet deposit in iteration 2 causing the scaffold to fuse together when it was rolled off, minimum deposit near side B in iteration 3, and a spot with minimum deposit near side A in iteration 4. This lead to the fifth and final iteration, (750 rpm, 290 mm from needle, +18 kV, -3 kV, 5 ml/hr, 5 mm/s translation speed, needle adjusted to cover 20 mm past side A during mandrel translation).

7.3. Differential Scanning Calorimeter Operating Procedure

7.3.1. Indium Calibration

The calibration process used was as follows:

1. The two lids on the DSC were removed with tweezers.
2. The Indium and reference (empty) pans were weighed and placed inside the DSC (Indium on the left, reference pan on the right).
    a. Make sure to use clean tweezers when moving the pans, and never touch them with bare hands, as oil from the hands will contaminate the sample, causing inaccurate results.
3. The lids were then placed back on the DSC.

4. The Indium calibration (10°C/min) method file was loaded into Pyris, and the weight of the Indium (with the weight of the reference pan subtracted from the weight of the Indium pan) was entered into the method editor.
5. After checking the program in the method editor, and confirming all the steps and gases used are correct, the test was started.
6. Once the Indium calibration test has been complete, using the "Peak Area" and "Onset" tools from the calculation tab, the delta H and onset X values were applied in the calibration tab.
    a. Peak area: select the area under the peak by left-clicking on the left side of the graph where the curve starts to become near horizontal, then drag the mouse across to the right side of the peak where the curve starts to become horizontal, and then let go. Press calculate, the peak temperature, area and delta H should appear on the graph.
    b. Onset: left-click on the left side of curve where it starts to become flat and drag across to the right, just before the turning point of the peak, where the curve looks relatively linear, and then let go. Drag on the handles that appear, until the two handles form tangents to the curve, one for the horizontal, and the other for the linear part. Press calculate, the onset X and Y values should appear on the graph. Repeat the process for the right side of the graph, starting on the right side of the turning point where the curve becomes linear, and ending where the curve starts to become horizontal.

7.3.2. Nitinol Testing

For the testing of Nitinol, the process used was as follows (make sure clean latex gloves are worn, and clean tweezers are used when handling the pans and samples):

1. An empty 50 µl reference pan with a crimped lid (crimped with a specialized crimping press for these specific pans) was weighed and placed inside the DSC on the right.
2. A 50 µl pan was placed on the scale and tared.
    a. The Nitinol wire was cut into small segments, and wiped clean with isopropyl alcohol.
    b. Approximately 30mg of the wire segments were placed inside the pan, and a lid was crimped on.
3. The Nitinol sample pan was then placed in the DSC on the left side, and the two DSC lids were then replaced.

4. The Nitinol DSC method was loaded into Pyris, or set up to perform the following procedures (using the "Initial State" and "Program" tabs):

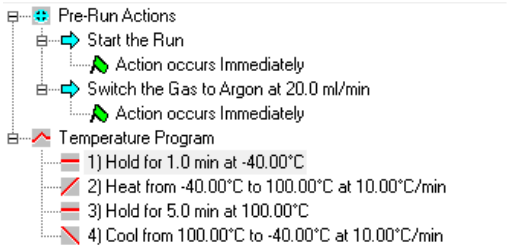

5. The process could be sped up if the temperature was set to -40℃ while setting up the samples and the method.
6. Click on the start button in Pyris and wait for the test to be completed.
7. Left-click and drag on the graph, a selection box will appear, enclose the desired section (the section around the two peaks for heating and cooling) of the graph then double-click in the middle of the selection to zoom in.
8. Click on the "Display" tool and show the "Legend".
9. Click on the "Curves" tool and select "Heat Flow", add a curve for the heating phase, and one for the cooling phase. These should now appear as separate curves on the legend.
10. By clicking on a curve on the legend, "Peak area" and "Onset" calculations as mentioned above could then be performed on each separate curve. These calculations were done for the heating and cooling curves.

7.4. Tensile Testing

The tensile test process used was as follows:

1. The specimen was first prepared and cut into 5 mm x 28 mm strips using a SAT67546 dog-bone cutter.
    a. A 2 mm thick rubber mat on top of a 2 mm thick metal plate was placed under the press.
    b. A paper towel was folded around 4 times and placed on top of the rubber mat.
    c. The specimen was placed on the paper towel, and the dog-bone cutter was placed on the specimen, aligned to the centre of the press and as desired (longitudinal, circumferential or 45° etc.).
    d. Pull down firmly on the handle of the press, cutting from the specimen all the way through the rubber mat.
    e. Release the handle and remove the specimen.

2. A 10 mm division was marked on the specimen along its length with a fine liner, placed as near the centre as possible.
3. Switch on the Instron Tensile Tester from the back of the machine.
4. Switch on the connected computer.
5. Once the display on the Instron has counted down and showed the number "2", the Merlin software was started on the computer.
6. Select and set up the method to be used on Merlin.
    a. Or any method could be selected, modified, and saved as a new file for the desired testing process.
    b. Set up the pre-test speeds. The following was used:
        i. 100 mm/min until 0.1 N load was reached.
    c. Set up the testing speeds and stop conditions. The following was used:
        i. 25 mm/min for electrospun scaffolds.
        ii. 5 mm/min for commercial woven scaffolds.
        iii. Stop test when the load drops by 99% with a 1 N sensitivity.
    d. Set up the starting length, width, and name for the specimen
7. Clamp the specimen onto the Instron.
    a. Raise the top clamp using the up button on the Instron until enough space was made to insert the specimen.
    b. Clamp the specimen on the top clamp, aligning the top division mark with the end of the clamp.
    c. Lower the top clamp using the down button, then fine tune using the scroll wheel, until the bottom division mark aligns with the end of the bottom clamp. Hand tighten both clamps.
    d. Using the scroll wheel, raise the top clamp slightly until the specimen just becomes straight, but without excess tension applied.
8. Zero both the extension and the forces on the Instron. This can be done in Merlin or using the buttons on the Instron.
9. Press start on Merlin and wait for the test to be completed.

Typical stress strain curve for electrospun graft scaffolds:

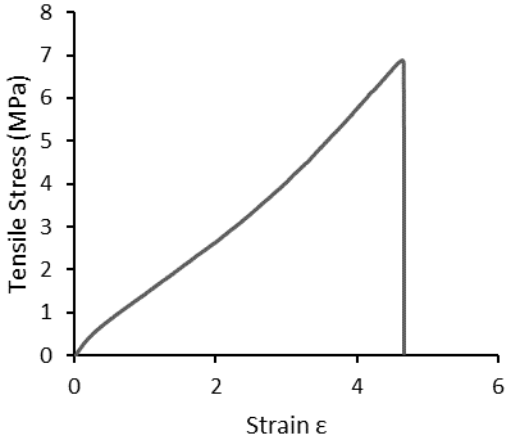

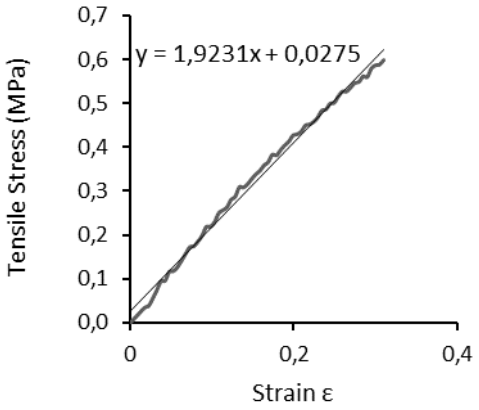

Typical stress strain curve for commercial woven Dacron graft scaffolds:

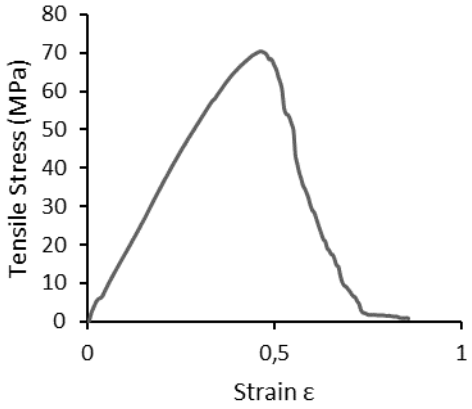

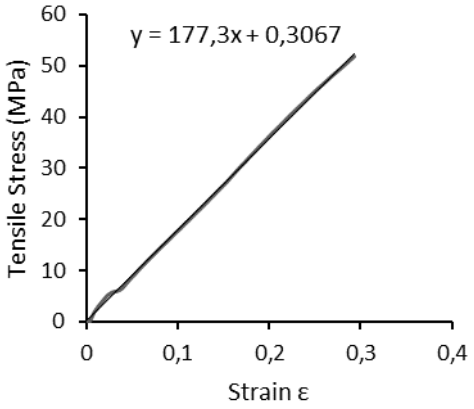

7.5. Radial Force Test

Bare stents

Student's t-test results comparing commercial and in-house Nitinol stent rings radial force:

	Cook	Medtronic	S25-STD	S25-H05	S25-H15	S25-PD10	S25-PD20	S25-D250	S25-D500-1	S25-D500-2	S25-12W	S25-16W
Cook	1	3,75723E-07	7,31362E-15	9,58766E-16	4,62404E-11	3,46454E-05	0,003328857	1,44772E-23	9,0288E-25	9,73678E-14	9,30076E-17	1,0685E-19
Medtronic	3,75723E-07	1	0,059649763	3,41331E-09	6,87523E-06	6,44798E-17	5,46184E-08	3,31931E-19	1,51947E-11	1,97495E-20	4,43735E-06	5,57057E-10
S25-STD	7,31362E-15	0,059649763	1	8,71394E-18	4,18246E-08	5,233E-24	3,04945E-14	8,96328E-20	1,89434E-17	1,28636E-27	0,000151688	1,11565E-11
S25-H05	9,58766E-16	3,41331E-09	8,71394E-18	1	1,9022E-19	5,57183E-17	4,74016E-07	3,23264E-22	3,78445E-18	2,65562E-16	1,42645E-19	7,44591E-20
S25-H15	4,62404E-11	6,87523E-06	4,18246E-08	1,9022E-19	1	3,02651E-25	2,7573E-15	1,82018E-27	2,69306E-20	4,13E-30	5,6269E-14	2,17799E-18
S25-PD10	3,46454E-05	6,44798E-17	5,233E-24	5,57183E-17	3,02651E-25	1	0,057622783	2,41306E-32	1,89311E-27	1,599E-18	6,21418E-27	3,06793E-28
S25-PD20	0,003328857	5,46184E-08	3,04945E-14	4,74016E-07	2,7573E-15	0,057622783	1	9,25784E-20	3,15154E-16	4,94691E-10	3,02443E-16	5,01379E-17
S25-D250	1,44772E-23	3,31931E-19	8,96328E-20	3,23264E-22	1,82018E-27	2,41306E-32	9,25784E-20	1	0,087658466	2,98864E-36	4,26856E-21	2,80724E-17
S25-D500-1	9,0288E-25	1,51947E-11	1,89434E-17	3,78445E-18	2,69306E-20	1,89311E-27	3,15154E-16	0,087658466	1	8,05039E-30	5,11349E-17	1,36215E-13
S25-D500-2	9,73678E-14	1,97495E-20	1,28636E-27	2,65562E-16	4,13E-30	1,599E-18	4,94691E-10	2,98864E-36	8,05039E-30	1	1,15745E-30	1,31956E-31
S25-12W	9,30076E-17	4,43735E-06	0,000151688	1,42645E-19	5,6269E-14	6,21418E-27	3,02443E-16	4,26856E-21	5,11349E-17	1,15745E-30	1	1,10673E-09
S25-16W	1,0685E-19	5,57057E-10	1,11565E-11	7,44591E-20	2,17799E-18	3,06793E-28	5,01379E-17	2,80724E-17	1,36215E-13	1,31956E-31	1,10673E-09	1

Radial force of commercial stent rings at various positions on the device:

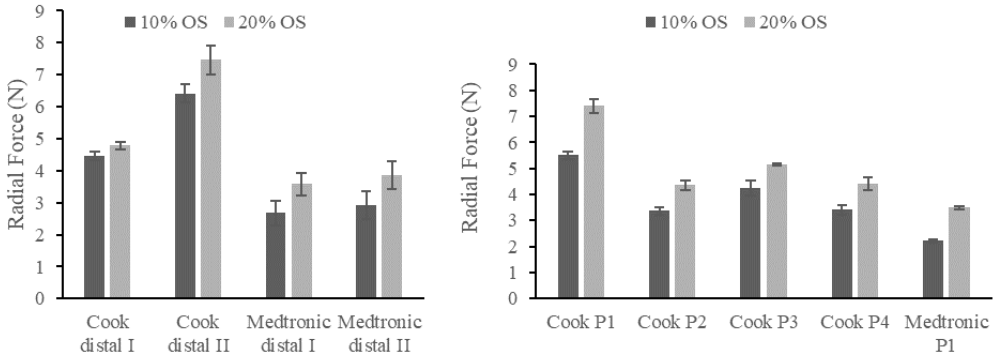

Stent Graft

Student's t-test results comparing commercial and in-house Nitinol stent-graft radial force:

	Cook Average	Medtronic Average	S25-STD SG	S25-H05 SG	S25-H15 SG	S25-PD10 SG	S25-PD20 SG	S25-D250 SG	S25-D500 SG	S25-12W SG	S25-16W SG	PS-P16 SG
Cook Average	1	2,1471E-05	6,87391E-10	2,32762E-10	0,073860775	0,000220101	6,44376E-06	2,65518E-17	9,09362E-10	2,97317E-06	0,000175697	1,37312E-08
Medtronic Average	2,1471E-05	1	0,997380523	8,86267E-12	2,87182E-07	8,25098E-09	1,64792E-09	1,78476E-08	4,68381E-11	2,68445E-09	2,48604E-08	0,016674194
S25-STD SG	6,87391E-10	0,997380523	1	5,8857E-16	5,81879E-17	2,36857E-25	4,61917E-23	6,40472E-24	3,25476E-23	1,21332E-13	5,3821E-13	1,01903E-05
S25-H05 SG	2,32762E-10	8,86267E-12	5,8857E-16	1	1,49056E-10	9,89939E-10	1,28465E-08	1,42959E-19	0,000148022	0,000120846	1,24736E-06	2,80355E-21
S25-H15 SG	0,073860775	2,87182E-07	5,81879E-17	1,49056E-10	1	0,000286283	1,1162E-06	1,38132E-23	3,31561E-12	8,00527E-06	0,001052243	3,49117E-14
S25-PD10 SG	0,000220101	8,25098E-09	2,36857E-25	9,89939E-10	0,000286283	1	0,000291753	6,98351E-30	6,039E-13	0,000290909	0,056202802	1,42132E-18
S25-PD20 SG	6,44376E-06	1,64792E-09	4,61917E-23	1,28465E-08	1,1162E-06	0,000291753	1	6,09396E-28	1,3971E-09	0,008128101	0,590679532	7,84615E-20
S25-D250 SG	2,65518E-17	1,78476E-08	6,40472E-24	1,42959E-19	1,38132E-23	6,98351E-30	6,09396E-28	1	5,58779E-27	2,1995E-18	2,36652E-18	4,45435E-24
S25-D500 SG	9,09362E-10	4,68381E-11	3,25476E-23	0,000148022	3,31561E-12	6,039E-13	1,3971E-09	5,58779E-27	1	0,219915279	0,000920067	3,91167E-23
S25-12W SG	2,97317E-06	2,68445E-09	1,21332E-13	0,000120846	8,00527E-06	0,000290909	0,008128101	2,1995E-18	0,219915279	1	0,078523371	8,92288E-17
S25-16W SG	0,000175697	2,48604E-08	5,3821E-13	1,24736E-06	0,001052243	0,056202802	0,590679532	2,36652E-18	0,000920067	0,078523371	1	5,14495E-15
PS-P16 SG	1,37312E-08	0,016674194	1,01903E-05	2,80355E-21	3,49117E-14	1,42132E-18	7,84615E-20	4,45435E-24	3,91167E-23	8,92288E-17	5,14495E-15	1

Radial force of distal components of commercial stent-grafts:

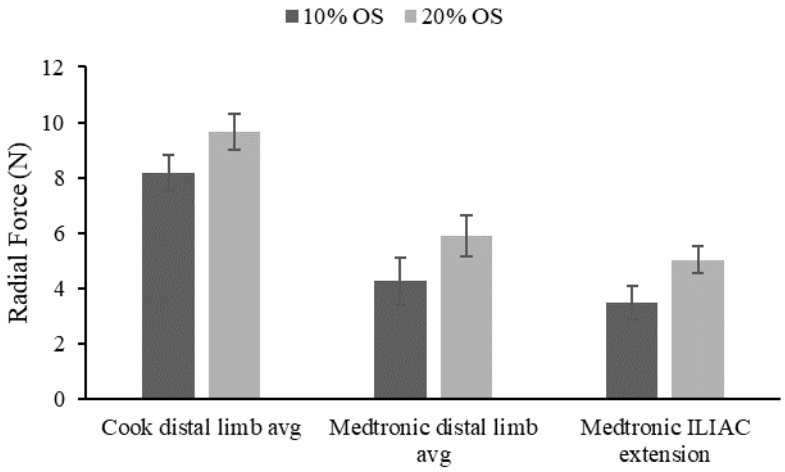

7.6. Poisson's Ratio Test

The Poisson's ratios test was performed on the Instron tensile tester (see tensile test section for basic set up and start up instructions) was as follows:

1. The graft scaffolds were cut into circumferential and longitudinal segments using the dog-bone cutter as mentioned in the Instron tensile test section above.

2. Similar to the tensile test, a 10 mm division was marked along the length of the segment, and a straight line was drawn in the centre perpendicular to the length of the segment.
3. The Instron and Merlin were started as mentioned above.
4. The specimen was then clamped on the Instron by the two outer lines marking the 10 mm division, and straightened using the scroll wheel on the Instron (make sure not to overstretch it).
5. A cell phone (iPhone 8) camera was used to take the pictures of this experiment.
    a. The phone was mounted horizontally between the clamps of a test tube holder.
    b. The clamps were secured tightly and made sure that when a photo was taken, the phone and the holder does not shake, or move out of place.
    c. The holder was positioned such that the camera aligns with the specimen between the Instron clamps.
    d. The camera was then zoomed in fully to ensure consistency of the photos.
6. The extension and force were zeroed on the Merlin software.
7. A photo was taken for the starting point of the experiment.
8. Using the scroll wheel on the Instron, the specimen was manually stretched in 0.5 mm increments, and a photo was taken at each increment, until a 3 mm extension was reached.
9. The photos were then processed using Fiji (Image J).
    a. Since all these images were taken at almost the exact same distance (assuming minor vibrations when touching the phone to capture the photo to be negligible) the scale for all the photos in a set (all photos from one sample) was set using the first image.
        i. Using the known initial width of 5 mm for the specimen, a line was drawn on Image J across the width of the specimen (along the line drawn in the centre), and used to set the scale (under the “Analyze” tab) of the image.
    b. Click on the top of the window of the image in Image J and press “m” on the keyboard to measure the length of the line. A new “Results” window should pop up showing the length of the line to be “5”.
    c. Open each consecutive image in the set in Image J, each time drawing a line over the centre line and press “m” to measure the new lateral length as the specimen is stretched longitudinally.
    d. The results window should now be populated with all the above measurements.
    e. The results were saved as a .csv file and processed in Excel to calculate the Poisson’s ratio. The process was repeated for each set of photos.

7.7. Delamination

The process used was as follows:

1. The graft without a stent in between was split lengthwise using two pairs of tweezers.
    a. The layers were split in half by pulling on a corner in opposite directions until the layers peel away from each other.
2. The graft with a stent in was easier to split, as soon as it was cut and the stent was removed, the air gap between the layers allowed the graft to be split easily.
3. Keep pulling until 5 – 10 mm of the graft has been split, giving at least 10 mm length of material to be clamped. Make sure to leave at least 3 mm of un-delaminated material.
4. The Instron and Merlin were started as mentioned above.
5. Clamp each of the split end in the Instron, one on each clamp. Stretch using the buttons and scroll wheel on the Instron until almost straight.
6. Zero the extension and force. Measure the distance between the two clamps and enter it into Merlin as the initial distance.
7. Set the test speed to 5 mm/min, set up the name of the experiments etc. and start the test. The tension measured shows the force required to pull the two layers apart.

Typical delamination test stress-strain curve:

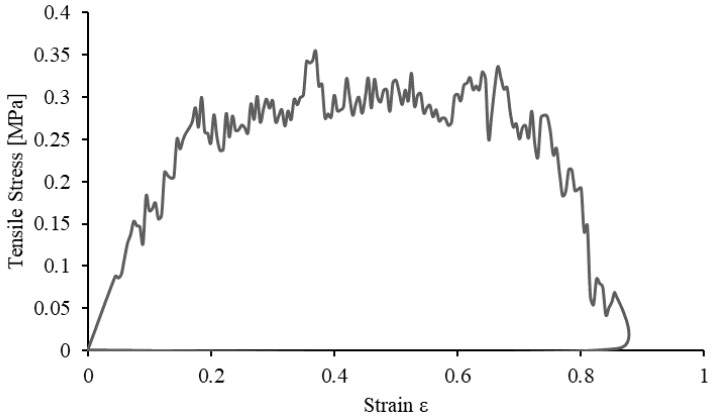

7.8. Fibre Morphology

7.8.1. Image Processing

7.8.1.1. Coherency

OrientationJ Macro

```
run("Set Scale...", "distance=344 known=50 pixel=1 unit=um global");// Current scale at x2000
makeRectangle(0, 0, 1024, 880);
run("Crop");
run("Despeckle");
run("Enhance Contrast", "saturated=0.3 normalize equalize");
run("Median...", "radius=2");
makeRectangle(0, 0, 1024, 880);
run("OrientationJ Measure", "measure");
```

Student's t-test results comparing the OI of the electrospun scaffolds from various electrospinning mandrel geometries:

	C05	C10	C15	C20	E10	E15	E20	E25	E30	S25	T10	T15	T20	T25	T30
C05	1.00000	0.14392	0.01991	0.85386	0.51372	0.74473	0.06029	0.13808	0.39656	0.34972	0.00023	0.00138	0.92327	0.23612	0.95002
C10	0.14392	1.00000	0.48995	0.10878	0.06062	0.30365	0.00196	0.98090	0.70426	0.04352	0.00001	0.00004	0.29706	0.98141	0.28387
C15	0.01991	0.48995	1.00000	0.01418	0.00651	0.06264	0.00003	0.48343	0.31161	0.00428	0.00000	0.00000	0.07796	0.59103	0.07313
C20	0.85386	0.10878	0.01418	1.00000	0.63307	0.62842	0.09816	0.10836	0.32872	0.44396	0.00055	0.00288	0.81327	0.19721	0.83898
E10	0.51372	0.06062	0.00651	0.63307	1.00000	0.37053	0.29625	0.05194	0.20745	0.76255	0.00545	0.01950	0.54948	0.12583	0.57037
E15	0.74473	0.30365	0.06264	0.62842	0.37053	1.00000	0.03396	0.25975	0.60554	0.25088	0.00020	0.00109	0.86490	0.38531	0.84064
E20	0.06029	0.00196	0.00003	0.09816	0.29625	0.03396	1.00000	0.00084	0.02103	0.52874	0.02572	0.08805	0.10685	0.00966	0.11539
E25	0.13808	0.98090	0.48343	0.10836	0.05194	0.25975	0.00084	1.00000	0.68831	0.03239	0.00000	0.00002	0.26302	0.99646	0.25128
E30	0.39656	0.70426	0.31161	0.32872	0.20745	0.60554	0.02103	0.68831	1.00000	0.15600	0.00031	0.00128	0.56063	0.74836	0.54366
S25	0.34972	0.04352	0.00428	0.44396	0.76255	0.25088	0.52874	0.03239	0.15600	1.00000	0.02100	0.05888	0.41146	0.09651	0.42848
T10	0.00023	0.00001	0.00000	0.00055	0.00545	0.00020	0.02572	0.00000	0.00031	0.02100	1.00000	0.65054	0.00249	0.00020	0.00278
T15	0.00138	0.00004	0.00000	0.00288	0.01950	0.00109	0.08805	0.00002	0.00128	0.05888	0.65054	1.00000	0.00846	0.00080	0.00933
T20	0.92327	0.29706	0.07796	0.81327	0.54948	0.86490	0.10685	0.26302	0.56063	0.41146	0.00249	0.00846	1.00000	0.38597	0.97885
T25	0.23612	0.98141	0.59103	0.19721	0.12583	0.38531	0.00966	0.99646	0.74836	0.09651	0.00020	0.00080	0.38597	1.00000	0.37374
T30	0.95002	0.28387	0.07313	0.83898	0.57037	0.84064	0.11539	0.25128	0.54366	0.42848	0.00278	0.00933	0.97885	0.37374	1.00000

7.8.1.2. Fibre Diameter

Typical images generated during the process of fibre diameter evaluation using DiameterJ plugin:

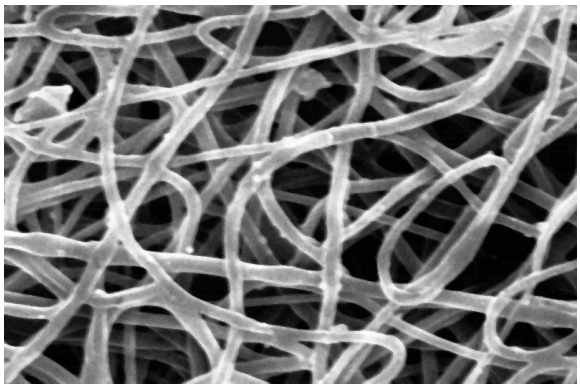

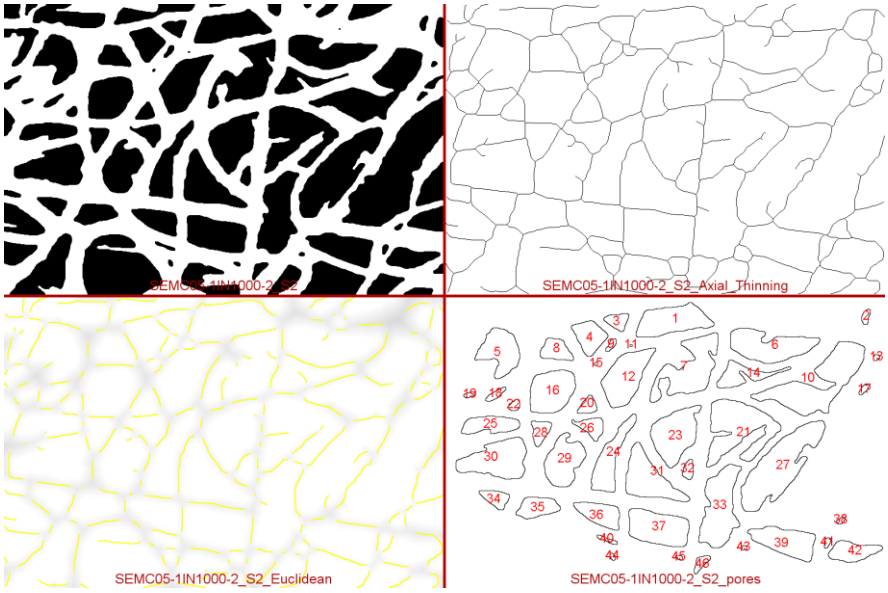

Student's t-test results comparing fibre diameter variations at different positions on the P16 graft geometry electrospun scaffold:

P16	1	2	3	4	5	6	7	8	9
1	1	0.804802	0.000758	0.043343	0.472525	0.115342	0.000152	0.000146	0.003542
2	0.804802	1	0.005584	0.121801	0.801835	0.283766	0.002143	0.001649	0.015502
3	0.000758	0.005584	1	0.07236	7.7E-05	0.007775	0.662212	0.365018	0.707868
4	0.043343	0.121801	0.07236	1	0.042846	0.43009	0.024377	0.01604	0.186832
5	0.472525	0.801835	7.7E-05	0.042846	1	0.139275	4.25E-07	2.59E-06	0.001537
6	0.115342	0.283766	0.007775	0.43009	0.139275	1	0.001186	0.001047	0.036693
7	0.000152	0.002143	0.662212	0.024377	4.25E-07	0.001186	1	0.436192	0.453582
8	0.000146	0.001649	0.365018	0.01604	2.59E-06	0.001047	0.436192	1	0.276056
9	0.003542	0.015502	0.707868	0.186832	0.001537	0.036693	0.453582	0.276056	1